UNIVERSIDADE FEDERAL DE SANTA CATARINA
CENTRO TECNOLÓGICO
PROGRAMA DE PÓS-GRADUAÇÃO EM ENGENHARIA ELÉTRICA

Mateus de Freitas Bueno

THREE-PHASE DAB CONVERTER WITH RECONFIGURABLE TRANSFORMER CONNECTION STRATEGY

Florianópolis
Setembro de 2023

Mateus de Freitas Bueno

THREE-PHASE DAB CONVERTER WITH RECONFIGURABLE TRANSFORMER CONNECTION STRATEGY

Dissertação submetida ao Programa de Pós-Graduação em Engenharia Elétrica da Universidade Federal de Santa Catarina para a obtenção do título de Mestre em Engenharia Elétrica
Orientador: Prof. André Luís Kirsten, Dr.
Coorientador: Eduardo Valmir de Souza, Dr.

Florianópolis
Setembro de 2023

Catalogação na fonte pela Biblioteca Universitária da Universidade Federal de Santa Catarina.
Arquivo compilado às 11:16h do dia 13 de dezembro de 2023.

Mateus de Freitas Bueno
THREE-PHASE DAB CONVERTER WITH RECONFIGURABLE TRANSFORMER CONNECTION STRATEGY/
Mateus de Freitas Bueno. - Florianópolis, Setembro de 2023-
104 p. : il. (algumas color.) ; 30 cm.

Orientador: Prof. André Luís Kirsten, Dr.
- Universidade Federal de Santa Catarina - UFSC
Departamento de Engenharia Elétrica e Eletrônica - EEL
Programa de Pós-Graduação em Engenharia Elétrica - PGEEL, Setembro de 2023.

1. Comutação Suave. 2. Conversor CC-CC Isolado. 3. *Dual-Active Bridge*. 4.
Magneticos de alta frequência. 5. Otimização de conversores.

Mateus de Freitas Bueno

THREE-PHASE DAB CONVERTER WITH RECONFIGURABLE TRANSFORMER CONNECTION STRATEGY

O presente trabalho em nível de mestrado foi avaliado e aprovado por banca examinadora composta pelos seguintes membros:

Prof. Gierri Waltrich, Dr.
Universidade Federal de Santa Catarina

Prof. Lucas Mondardo Cunico, Dr.
Instituto Federal de Santa Catarina

Prof. Carlos Alberto Teixeira, Ph.D.
Royal Melbourne Institute of Technology

Certificamos que esta é a **versão original e final** do trabalho de conclusão que foi julgado adequado para obtenção do título de Mestre em Engenharia Elétrica.

Documento assinado digitalmente
Telles Brunelli Lazzarin
Data: 20/12/2023 11:04:42-0300
CPF: ***.400.719-**
Verifique as assinaturas em https://v.ufsc.br

Prof. Telles Brunelli Lazzarin, Dr.
Coordenador do Programa

Documento assinado digitalmente
Andre Luis Kirsten
Data: 15/12/2023 11:04:39-0300
CPF: ***.272.690-**
Verifique as assinaturas em https://v.ufsc.br

Prof. André Luís Kirsten, Dr.
Orientador

Florianópolis
Setembro de 2023.

Dedico este trabalho à minha família, os verdadeiros responsáveis por todas as minhas conquistas.

Acknowledgements

Em primeiro lugar, quero agradecer profundamente aos meus pais, Silvane de Freitas Bueno, Luiz Joaquim Bueno e ao meu irmão Vitor de Freitas Bueno, por sua confiança inabalável, apoio constante e motivação ao longo de todas as etapas da minha vida. Sua fé em mim é o principal motivo pelo qual alcancei esta etapa importante.

À minha namorada, Laura Bona Moll, que esteve sempre ao meu lado durante a minha jornada acadêmica, inclusive fazendo frequentemente a viagem de Joinville a Florianópolis para passar os finais de semana comigo, meu sincero agradecimento.

Ao Professor André Luís Kirsten, meu orientador, quero expressar minha gratidão pela orientação, dedicação e confiança em meu trabalho.

Ao Eduardo Valmir de Souza, meu coorientador, agradeço pelas conversas e sugestões valiosas que contribuíram para o aprimoramento do meu trabalho.

Aos grandes amigos que conheci no INEP, incluindo Artur Magnus, Brendon Kulak, Caio Hudson, Christopher da Fonseca, Cleiton Dal'Agnol, Douglas Sotoriva, Edhuardo Grabovski, Esio Eloi, Ícaro Albuquerque, Ion Leandro, Leonardo Bender, Leonardo Bellincanta, Mateus Nava, Mateus Orige, Nicholas Furtado, Paulo Ícaro Teixeira, Rossano Sotoriva, Suélen Bampi, Tailan Orlando, Thiago Rech, Valdecir Junior de Paris, Welenton Maito e William Rafhael, meu profundo agradecimento. Suas conversas estimulantes e os momentos de descontração compartilhados dentro e fora do INEP foram inestimáveis.

Aos professores do INEP, André Luís Kirsten, Denizar Cruz Martins, Gierri Waltrich, Marcelo Lobo Heldwein, Roberto Francisco Coelho, Samir Ahmad Mussa e Telles Brunelli Lazzarin, agradeço pelos ensinamentos, convivência e disponibilidade nos momentos de dúvida.

Ao secretário Diogo Duarte e ao técnico Antônio Pacheco, meu agradecimento por criarem as condições para a realização deste trabalho.

Por fim, aos membros da banca, Prof. Carlos Alberto Teixeira, Prof. Gierri Waltrich e Prof. Lucas Mondardo Cúnico, agradeço pelas valiosas sugestões e comentários que enriqueceram este trabalho.

Resumo

A pesquisa começa com uma revisão da literatura e contextualização do conversor *Three-phase Dual Active Bridge* (DAB3), explorando várias técnicas de modulação. A modulação *phase-shift* (PS) é utilizada neste trabalho. São analisadas seis possíveis conexões do transformador entre as duas pontes trifásicas, a partir das quais são derivadas as principais equações para estimar perdas e ganho estático. Esse procedimento é aplicado a todas as seis conexões de transformadores e para toda a faixa de ângulos. Além disso, é realizada uma análise do processo de comutação, categorizando a operação do conversor em regiões de *Zero Voltage Switching* (ZVS), *incomplete Zero Voltage Switching* (iZVS) e *Hard Switching* (HS). A principal contribuição deste trabalho é a Estratégia Transformador com Conexão Reconfigurável (RTCS) para aumentar a eficiência do conversor por meio da utilização de duas conexões distintas de transformador, cada uma com uma região diferente de ZVS. Essa estratégia se mostra especialmente eficaz quando o conversor é exposto a cargas com variações significativas de tensão. Os arranjos iDY e YY são escolhidos para o protótipo, cada uma selecionada para operar em diferentes níveis de tensão. O protótipo projetado é testado em diferentes pontos de operação. Por fim, a eficiência do protótipo é comparada com a eficiência teórica, e a validade das equações de perdas é confirmada. Para otimizar ainda mais o projeto do DAB3, um algoritmo de otimização é desenvolvido utilizando as equações teóricas validadas. Esse algoritmo determina a configuração mais adequada para o transformador entre as opções estudadas. Além disso, o algoritmo é expandido para projetar o DAB3 com perdas reduzidas ao utilizar a RTCS. Ao comparar a eficiência, custo e/ou volume com e sem RTCS, os benefícios potenciais são avaliados.

Palavras-chave: Comutação Suave, Conversor CC-CC Isolado, *Dual Active Bridge*, Magneticos de alta frequência, Otimização de conversores.

Resumo Expandido

Introdução

Pesquisadores e engenheiros têm desenvolvido diversas tecnologias e sistemas para gerar e distribuir energia de forma mais eficiente, a fim de atender à demanda crescente por eletricidade [1]. A versatilidade dos Conversores CC-CC Isolado Bidirecional (IBDCs) tem levado à sua ampla adoção em inúmeras aplicações. O aumento do uso de recursos de energia renovável resultou no surgimento de microrredes, geração distribuída e sistemas de armazenamento de energia como soluções inovadoras para lidar com preocupações de confiabilidade e estabilidade.

Os Conversores CC-CC Isolados Bidirecionais (IBDCs) possuem classificações em tipos de estágios únicos e de dois estágios. Os de um estágio possuem menos estágios de conversão e, portanto, menos componentes. No entanto, operá-los em amplas faixas de tensões pode ser ineficiente. Topologias de múltiplos estágios, como os conversores de dois estágios, adicionam conversores de potência para ajustar níveis de tensão e corrente, melhorando a eficiência dos componentes. Conversores AC/DC e DC/AC são essenciais para fornecer energia AC ao transformador de alta frequência (HF), com diferentes configurações de circuito. Redes ressonantes de HF armazenam energia nessa parte AC e moldam as formas de corrente para reduzir perdas. O transformador de HF é fundamental para isolamento elétrico e amplificação de tensão e corrente. Combinados, esses componentes permitem que o IBDC converta energia eficientemente, mantendo o isolamento.

Conversores bidirecionais flyback e push-pull são comuns como IBDCs básicos. A topologia flyback é eficiente em baixas potências, mas é desafiadora pela complexidade do transformador. Já o push-pull é usado em potências maiores, com problemas de tensões indesejadas. O Dual Active Bridge (DAB) lida bem com maiores potências, tanto a versão monofásica (DAB1) quanto a versão trifásica (DAB3). Estudos comparativos mostram que o DAB3 é mais eficiente em densidades de potência mais altas. Conversores ressonantes, embora complexos, reduzem perdas de comutação. O DAB3 é escolhido neste trabalho por sua alta densidade de potência e menor estresse de corrente nos semicondutores.

Objetivos

O objetivo geral deste trabalho é analisar o conversor DAB3 e suas potenciais aplicações em sistemas de eletrônica de potência com grande variação de tensão na carga. O foco principal é explorar a eficiência do conversor em diferentes condições. Os objetivos específicos deste trabalho são os seguintes:

- Analisar a eficiência e as características de desempenho do DAB3 sob diferentes conexões do transformador com modulação PS. Desenvolver um modelo de perdas para o conversor. Comparar a eficiência teórica com resultados experimentais.
- Investigar o conceito de utilizar relés para alterar a conexão do transformador

trifásico, expandindo assim as regiões de ZVS.

- Desenvolver um algoritmo de otimização que utilize as equações teóricas validadas para encontrar o melhor projeto para um dado conjunto de componentes. O algoritmo deve ter a liberdade de selecionar entre as configurações de transformador estudadas.

Metodologia

A pesquisa baseia-se na análise do DAB3 com modulação PS. Equações analíticas de estresse e ganho estático para seis opções de conexões trífasicas são obtidas. A análise também aborda a tensão de descarga nos capacitores parasitas dos interruptores durante o tempo morto. Essas equações são validadas por meio de simulações e aplicadas às seis configurações estudadas. Propõe-se a Estratégia de Reconfiguração da Conexão do Transformador (RTCS) como uma forma de melhorar a eficiência do conversor em diferentes pontos de operação.

Resultados e Discussão

Duas configurações, iDY e YY, foram selecionadas para analisar os ganhos de eficiência da RTCS. A iDY é mais eficiente em tensões mais altas, enquanto a YY é mais eficiente em tensões intermediárias. Essa maior eficiência, dependendo do ponto de operação, foi confirmada pelo protótipo construído. A eficiência teórica e prática se aproximam, demonstrando que a alteração da conexão do transformador aumenta a eficiência. Com as equações validadas, um algoritmo foi desenvolvido para encontrar o projeto ótimo dado um conjunto de componentes. Ao comparar o projeto ótimo teórico com e sem a RTCS, observa-se que, na maioria dos casos, ocorre uma redução das perdas entre 15 % e 28 %, resultando em um aumento da eficiência do sistema. Além disso, é possível utilizar componentes magnéticos menores para uma mesma especificação de projeto.

Considerações Finais

Com o intuito de aumentar o desempenho do conversor, sugere-se os seguintes tópicos para trabalhos futuros:

- Desenvolvimento de equações de estresse e ganho estático considerando capacitores parasitas, tempo morto e diodo de corpo;
- Análise do conversor com técnicas de modulação mais complexas;
- Integração do modelo de perdas com o modelo térmico para uma análise abrangente do desempenho do conversor;
- Comparação entre o DAB3 e versões ressonantes para avaliar as vantagens e limitações de cada projeto;
- Desenvolvimento de técnicas de balanceamento para as correntes trifásicas visando aprimorar a eficiência do conversor.

Palavras-chave: Comutação Suave, Conversor CC-CC Isolado, *Dual Active Bridge*, Magnéticos de alta frequência, Otimização de conversores.

Abstract

The research commences with a literature review and contextualization of the Three-Phase Dual Active Bridge (DAB3) converter, exploring various modulation techniques. Phase shift modulation (PS) is used in this work. Six possible thee-phase transformer connections between the two three-phase bridges are analyzed, from which the main converter equations are derived to estimate losses and static gain. This procedure is applied to all transformer connections and full range of angles. Additionally, a switching process analysis is conducted, categorizing the converter operation into zero voltage switching (ZVS), incomplete zero voltage switching (iZVS), and hard switching (HS) regions. This work contributes by introducing the Reconfigurable Transformer Connection Strategy (RTCS) to enhance converter efficiency by utilizing two distinct transformer connections, each one with different ZVS regions. This strategy proves especially effective when the converter is exposed to loads with substantial voltage variations. The iDY and YY connections are chosen for the prototype, each one selected to operate at different voltage levels. The prototype was built and tested at different operations points. The prototype efficiency is compared with the theoretical efficiency, and the loss equations validity is confirmed. To further optimize the DAB3 design, an optimization algorithm is developed using the validated theoretical equations. This algorithm finds out the most suitable transformer connection among the studied options. Additionally, the algorithm is expanded to design the DAB3 with reduced losses when utilizing the RTCS. Potential benefits are evaluated by comparing the efficiency, cost, and/or volume with and without the RTCS.

Key-words: Soft-switching, Isolated DC-DC converter, Dual Active Bridge, High-frequency magnetic, Converter optimization.

List of Figures

List of Tables

List of abbreviations and acronyms

3ϕ network	Three-phase network
AWG	American Wire Gauge
BDC	Bidirectional DC-DC Converter
DAH	Dual Half Bridge Converter
DAB1	Single-phase Dual Active Bridge Converter
DAB3	Three-phase Dual Active Bridge Converter
ESS	Energy Storage Systems
EV	Electric Vehicle
EVSE	Electric vehicle supply equipment
HF	High Frequency
HS	Hard-Switching
IBDC	Isolated Bidirectional DC-DC Converters
iGSE	Improved Generalized Steinmetz Equation
iZVS	Incomplete Zero Voltage Switching
PCB	Printed Circuit Board
PS	Phase-shift modulation
PSO	Particle Swarm Optimization
RMS	Root mean square
RTCS	Reconfigurable Transformer Connection Strategy
SS	Soft-Switching
ZCS	Zero Current Switching
ZVS	Zero Voltage Switching

List of symbols

D_1	Primary power switch duty-cycle
D_2	Secondary power switch duty-cycle
D_ϕ	Power switch duty cycle due to phase shift
E_{off}	Turn-off Energy
E_{on}	Turn-on Energy
I_i	Average input current
I_o	Average output current
L_1	Secondary coils inductance from coupled inductor
L_2	Primary coils inductance from coupled inductor
L_{dab}	Auxiliar DAB inductor
L_m	Magnetizing inductance
L_{tr1}	Primary leakage inductance
L_{tr2}	Secondary leakage inductance
M	Mutual inductance from coupled inductor
N_L	Number of turns in the inductor
N_p	Number of turns in the primary winding
N_s	Number of turns in the secondary winding
R_{tr1}	Primary winding resistance
R_{tr2}	Secondary winding resistance
ΔV_i	Input voltage ripple
ΔV_o	Output voltage ripple
f_s	Switching Frequency
i_{C_i}	Input capacitor current

i_{Co}	Output capacitor current
i_{in}	Input current
i_{ld-x}	Current inductor L_{dab} at phase x
i_{out}	Output current
i_{tr-x}	Transformer primary current at phase x
i_{tr-X}	Transformer secondary current at phase X
i_x	Half-bridge current at phase x
l_g	Inductor air gap length
n	Transformation Ratio
n	Transformer voltage gain
s_{xi}	Switching function
s_x	Switching function at phase x
t_{dt}	Dead time
V_{div}	Ideal voltage to reconfigure the 3ϕ network
V_{hist}	Hysteresis voltage to reconfigure the 3ϕ network
V_i	Input voltage
V_o	Output voltage
ϕ	Phase shift angle
λ	Weight vector
$\mathbf{x}$	States for differential equations

Contents

Chapter

1 Introduction

Researchers and engineers have been developing various technologies and systems to generate and distribute power more efficiently to meet the ever-increasing demand for electricity [1]. One such prominent technology is the Isolated Bidirectional DC-DC Converter (IBDC).

1.1 IBDC APPLICATIONS

The versatility of IBDCs has driven their widespread adoption in numerous applications. Some notable ones are highlighted in this section.

1.1.1 Microgrids

The growing use of renewable energy resources led to the rise of microgrids, distributed generation, and energy storage systems as innovative solutions to address reliability and stability concerns [2]. Figure 1.1 showcases examples of microgrid applications with IBDC.

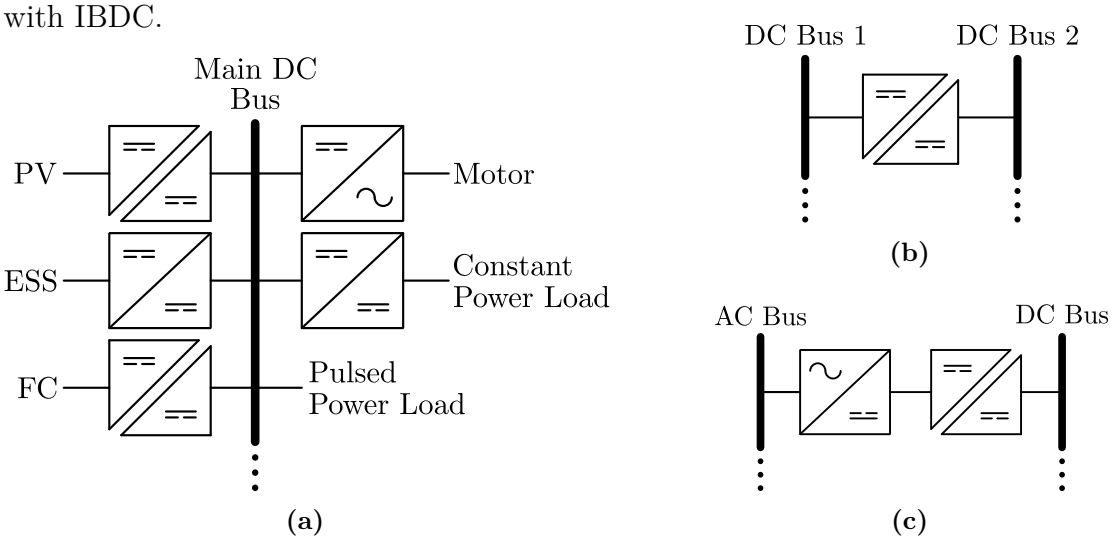

Figure 1.1 – (a) Typical DC microgrid with various sources and loads [3] (b) Interconnected DC microgrids [4] (c) Distribution system with an isolated bidirectional ac–dc converter [5]

Figure 1.1 (a) shows a typical DC microgrid configuration. In the context of DC microgrids, conventional DC/DC converters such as buck, boost, and buck/boost converters are commonly utilized. However, certain applications demand high voltage gain that exceeds the capabilities of these classical converters. Isolated converters are commonly used in this situation because of their high voltage step-up/down capability. Furthermore, for sensitive storage units and critical loads, galvanic isolation becomes essential, necessitating the implementation of an IBDC [3].

Figure 1.1 (b) presents another application where an efficient and reliable power management system is achieved through a direct interconnection between adjacent DC buses using an IBDC. This system architecture enables efficient power transfer between adjacent DC microgrids by reducing the number of power conversion stages. Additionally, it offers redundancy for each microgrid in the event of a system fault, thereby reducing the limitations of a single microgrid [4].

In Figure 1.1 (c), the diagram depicts a system configuration with an isolated bidirectional AC/DC converter. This setup shows the integration of an AC bus with a DC bus, which is particularly important when incorporating renewable energy sources. The isolated bidirectional AC/DC converter plays a central role in this system, enabling bidirectional power flow and regulating the DC-bus voltage. This ensures efficient utilization of renewable energy and effective management of power distribution to and from the AC grid [5].

1.1.2 EV chargers

Electric vehicles (EVs) have emerged as a promising and eco-friendly alternative to internal combustion engine vehicles. As the popularity of EVs continues to grow, there is a pressing need for a robust and efficient EV charging infrastructure. EV chargers can be classified into three levels. Level 1 chargers have a power capacity ranging from 1.44 kW to 1.92 kW and are primarily used for residential charging purposes. Level 2 chargers offer higher power, ranging from 3.1 kW to 19.2 kW, and are commonly used for both residential and commercial charging. Level 3 chargers, also known as fast chargers, operate with a power capacity ranging from 50 kW to 350 kW. Level 3 are typically installed at public places, resembling gas stations, and provide rapid charging capabilities. The Level 1 and Level 2 chargers are AC chargers, while Level 3 chargers are DC chargers [6].

While Level 1 and 2 chargers are on-board chargers inside the EV, Level 3 chargers are typically installed outside the vehicle to reduce weight and volume. They are off-board chargers that directly connect to the EV battery [7]. This connection facilitates faster and more efficient charging, contributing to the widespread adoption of electric vehicles and enabling longer journeys with shorter charging stops [8]. Figure 1.2 illustrates an EV charging system that incorporates both off-board and on-board chargers, with the connection to the EV facilitated by electric vehicle supply equipment (EVSE) [6].

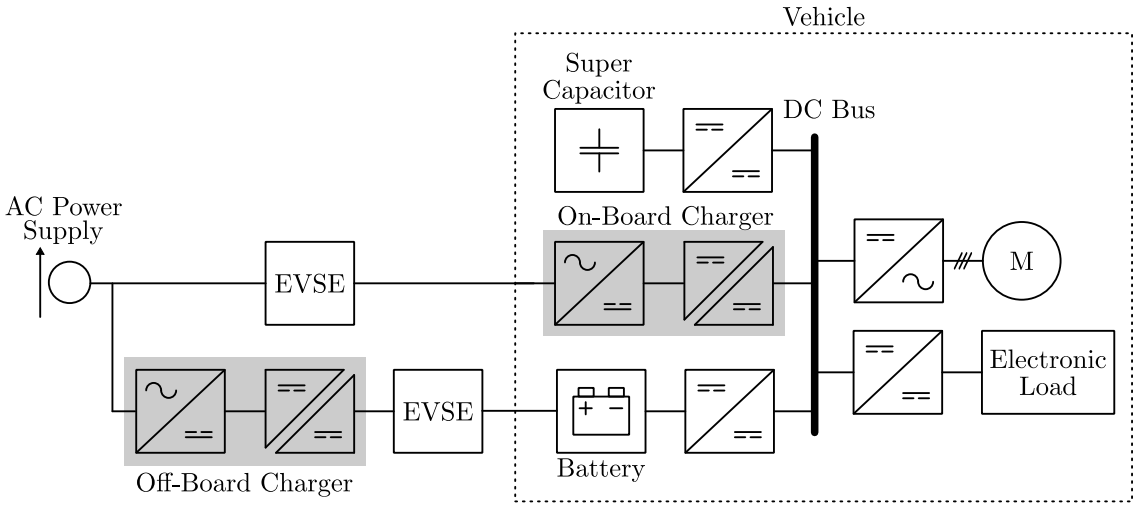

Figure 1.2 – EV charging system including off-board and on-board charger [6]

DC ultra-fast charging has emerged as a promising solution to reduce the range anxiety of electric vehicle (EV) drivers and compete with the quick refueling of internal combustion engine vehicles. This technology aims to fully charge EV batteries within just 10 minutes, using power ratings of 400 kW or higher [9]. However, implementing such high-power charging presents challenges and research needs in various areas. These include developing advanced EV batteries capable of handling rapid charging, designing robust and efficient charging cables, optimizing charging infrastructure to handle the significant power flow, ensuring overall reliability and safety during the charging process. Addressing these challenges is crucial to unlock the full potential of DC ultra-fast charging, making it a practical and widely adopted option for EVs [6].

These chargers are designed to be future-proof, with the capability to deliver more than 350 kW of power to the battery pack, even though current EVs do not yet require such high charging power, as shown in Table 1.1. Additionally, these chargers are designed to be compatible with future 800 V vehicles while still maintaining compatibility with existing 400 V systems. Manufacturers have achieved this compatibility by modularizing their designs, allowing for different configurations of current and voltage for the same power output. This modularity enables efficient high-power charging for both 400 V and 800 V vehicles, even at partial loads, taking advantage of economy-of-scale effects [10].

Table 1.1 – The charging specifications of some commercially available EVs [10].

Model	Battery Voltage	Rated Energy (Usable)	Onboard Charging Power (Time)	Maximum Charging Power (Time)
eCitaro (bus)	400 V	182 kWh	N/A	300 kW (29 min)
7900 Electric (bus)	600 V	150 kWh	11 kW(10.9 h)	300 kW (24 min)
Model S, long range	400 V	100 kWh	11.5 kW(10.25 h)	250 kW (38 min)
E-tron 55 Quattro	396 V	95 kWh	11 kW(9.25 h)	150 kW (26 min)
EQC 400 4Matic	405 V	85 kWh	7.4 kW(10.5 h)	150 kW (31 min)
Taycan 4S	800 V	79.2 kWh	11 kW(9 h); 9.6 kW(9.5 h)	270 kW (21 min)
Model 3, long range	360 V	75 kWh	11.5 kW(7.75 h)	250 kW (22 min)
Polestar 2	450 V	75 kWh	11 kW(7.75 h)	150 kW (31 min)
Bolt	350 V	62.2 kWh	7.4 kW(8.3 h)	50 kW (66 min)
Leaf e+	360 V	62 kWh	6.6 kW(11.5 h)	100 kW (35 min)
Zoe ZE50	400 V	54.7 kWh	22 kW(3 h)	50 kW (56 min)
Ioniq	320 V	40.4 kWh	7.2 kW(6.25 h)	100 kW (20.6 min)
Leaf	360 V	40 kWh	6.6 kW(6.5 h)	50 kW (40 min)

Furthermore, bidirectional off-board charging capability has been considered by EV manufacturers, although concerns regarding cost, volume, and battery degradation have been raised. While some current off-board charging can support bidirectional power flow, this feature is yet to be fully utilized due to the absence of complementary smart power system architecture from utility companies. Nevertheless, it is expected that bidirectional chargers will become more prevalent in future off-board charging designs, as they offer enhanced smart grid functionalities. Unidirectional chargers, though cost-effective and simpler to design, lack the capabilities provided by bidirectional counterparts [11].

1.2 IBDC TOPOLOGIES

IBDCs can be classified into two main types: single-stage and two-stage converters. Single-stage converters have a minimal number of conversion stages, resulting in a relatively lower number of components. However, operating them over wide input and output voltage ranges can lead to less efficient utilization of transformers and switches. On the other hand, multi-stage topologies, such as two-stage converters, include an additional power converter to adjust voltage and current levels, which enhances transformer and switch utilization [12]. The components of a single-stage IBDC is presented in Figure 1.3.

Figure 1.3 – Different components required for a single-stage IBDC [12]

The AC/DC and DC/AC converters play a crucial role in providing AC power to the high-frequency (HF) transformer. Different circuit configurations, such as full bridge,

half bridge, and push-pull circuits, can be used in these converters [13]. Resonant HF networks are used to store energy within the HF AC part and shape the switch current waveforms to reduce switching losses. While not strictly mandatory for the converter basic functionality, these HF networks are commonly included due to the presence of parasitic elements in the HF transformer, like stray inductances and parasitic capacitances [12].

The HF transformer is a vital component that ensures electrical isolation and allows for large voltage and current gain ratios. It offers advantages over low-frequency transformers, as higher frequencies enable smaller transformer and filter components [14]. Overall, the combination of these components enables the IBDC to efficiently convert and transfer power bidirectionally while maintaining isolation between the input and output sides [12].

Bidirectional flyback and push-pull converters are commonly used as basic IBDC. Bidirectional flyback topologies, presented in Figure 1.4 (a), find widespread application in low-power scenarios where galvanic isolation is necessary due to their simplicity, low component count and fast dynamic response. However, these converters face challenges related to the transformer, as it needs to provide both isolation and energy storage, leading to higher voltage and current stresses on the switches. Consequently, this results in substantial switching losses and reduced conversion efficiency. This converter has power limitations and does not offer high power density. This is because it does not use a transformer but instead employs coupled inductors, which have low utilization of the magnetic element and do not achieve good efficiency [15].

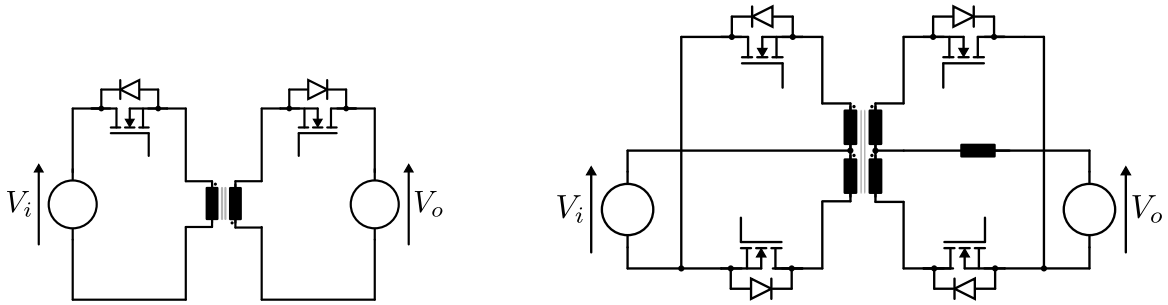

(a) **(b)**

Figure 1.4 – (a) Flyback converter [15] (b) Push-pull converter [13]

The push-pull converter, as shown in Figure 1.4 (b), is used for higher power levels compared to the flyback converter. Push-pull converters with high-frequency transformers can also experience issues with leakage inductance, leading to significant voltage spikes. Additionally, the presence of a transformer center tap adds complexity to the design, lowering the converter overall reliability. Considering these factors, basic voltage-fed isolated converters are better suited for low-power applications [13].

The Dual Active Bridge (DAB) converter is a topology capable of handling higher power levels. The DAB concept was introduced in 1989, comprising two transformer versions: single-phase (DAB1) and three-phase (DAB3), illustrated in Figure 1.5 [16].

These converters employ two back-to-back bridges connected by a transformer and a series inductance, facilitating power exchange between voltage sources [16, 17].

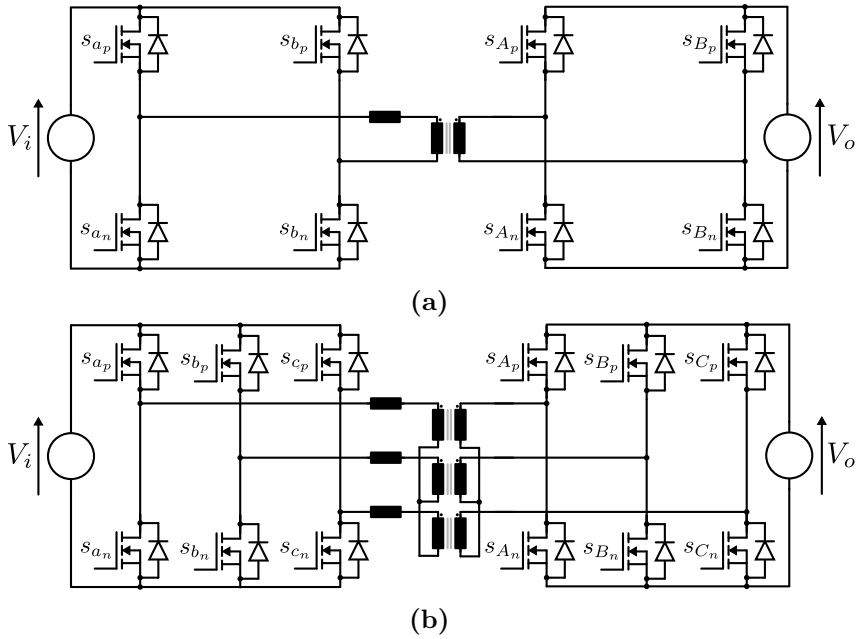

Figure 1.5 – (a) DAB1 converter (b) DAB3 converter [16]

Several studies have compared DAB1 and DAB3 [18, 19, 20]. Under phase shift modulation, DAB3 exhibits higher switching and conduction losses compared to DAB1, up to 30% and 18%, respectively. DAB1 ZVS boundaries provide wider soft-switching (SS) regions, allowing its working points to stay within the SS region for a broader range of normalized transferred power than DAB3. Certain operating conditions can reduce peak current stress by up to 30% for DAB1, while DAB3 has a higher RMS current, around 9%, despite having lower harmonic content. Due to reduced voltage and current ripple, DAB3 requires smaller capacitors, resulting in smaller volumes and weights. The optimal DAB approach for an application depends on balancing higher efficiency and lower volume [18].

On one hand, studies such as [21] have demonstrated that the three-phase transformer can achieve higher power density, especially under certain design constraints related to flux density and current. This attribute makes it particularly appealing for applications where limited space and high power density are crucial requirements. Additionally, the reduction in current stress on the semiconductors enables higher power processing using the same semiconductor technology, without the need for parallel switches [22].

The Dual Half Bridge (DHB) converter known for its high power density, is commonly utilized in medium power applications. In this converter, illustrated in Figure 1.6, the bus voltage is divided into two capacitors, resulting in double the current requirement for the same power compared to a full-bridge converter. Additionally, the DHB converter only offers the possibility of modulation with two levels. Despite these limitations, its high power density makes it well-suited for various medium-power applications [13].

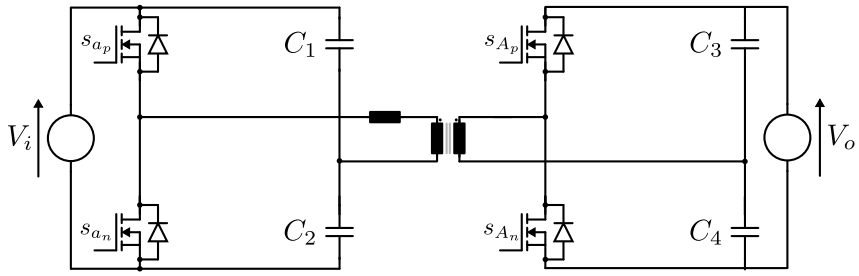

Figure 1.6 – DHB converter [13]

Resonant DC-DC converters, also known as DC-DC converters with resonant HF networks, offer advanced features using semiconductor switches effectively. By modifying the waveforms of the switch currents, they achieve low switching losses. However, these converters have some downsides, such as increased complexity and the requirement for additional power components. Nevertheless, their ability to significantly reduce switching losses makes them a promising choice for specific applications [12].

Taking these characteristics into account, the DAB3 configuration is chosen as the preferred option in this work. Since it has higher power capability and lower ripple current on both input and output side, which leads to lower capacitor volume and thus higher power density.

1.3 OBJECTIVES

The general objective of this work is to analyze the three-phase Dual Active Bridge Converter (DAB3) and its potential applications in power electronics systems with wide voltage variation at load. The main focus is to explore the converter efficiency under different conditions. The specific objectives of this work are:

- Analyze the efficiency and performance characteristics of the DAB3 under different transformer connection with PS modulation. Develop a converter loss model. Compare the theoretical efficiency with experimental results.
- Investigate the concept of using relays to change the transformer connection in the DAB3 converter, thereby expanding the ZVS regions.
- Develop an optimization algorithm that utilizes the validated theoretical equations to find the best design for a given set of components. The algorithm should have the freedom to select among the studied transformer connection configurations.

1.4 WORK STRUCTURE

This work consists of five chapters and three appendices.

- **Chapter 1**: This chapter provides a contextual overview of the topic and discusses the applications of IBDCs.
- **Chapter 2**: The methodology to derive analytical equations with PS modulation is described, and an analysis of converter switching during dead-time is conducted.
- **Chapter 3**: Introduces a strategy to enhance converter efficiency when the load voltage varies significantly. This approach involves switching between two 3ϕ networks to take advantage of their different ZVS regions. The chosen pair of 3ϕ networks, iDY and YY, are used in the prototype. Efficiency analysis at different operations points confirms that each transformer is optimized for a specific voltage level.
- **Chapter 4**: Extends the proven equations from previous chapters to a theoretical optimal design. The goal is to quantify the gains in volume, efficiency, and/or cost by introducing the option to switch between two transformers. Optimal designs for both options are presented, along with the optimization routines.
- **Chapter 5**: Discusses the conclusions and final considerations of the dissertation, along with proposals for future research.
- **Appendix A**: Present most of DAB3 basic equations.
- **Appendix B**: Outlines the 4 kW prototype design methodology.
- **Appendix C**: Presents all loss models used for both design and efficiency analyses.

Chapter

2 Three-Phase Dual Active Bridge Converter Review

This chapter provides a review of the Three-Phase Dual Active Bridge Converter (DAB3). The main modulation techniques are presented. Next, the arrangements of inductors plus three-phase transformer studied in this work are introduced. One of these arrangements is selected to present the methodology for obtaining the analytical equations of interest in this work. Simulations are conducted to compare the results with the theoretical equations. Finally, an analysis of the switching process is conducted to determine if the converter operates in ZVS region.

2.1 MODULATION STRATEGIES

The DAB3 can be operated using various modulation strategies. The switching functions are presented to explain some of these modulations. The switching function determines the status of each power switch in the DAB3 converter. It is defined as

$$s_{xi} = \begin{cases} 1 & \text{Switch } s_{xi} \text{ enabled} \\ 0 & \text{Switch } s_{xi} \text{ disabled} \end{cases}. \tag{2.1}$$

In this context, i represents the transistor leg (a, b, c, A, B or C), and x indicates the positive or negative power switch (p or n) between that transistor leg, as illustrated in Figure 1.5 (b). Assuming no dead time, the switching functions s_{ip} and s_{in} have a linear dependence, given by $s_{in} = 1 - s_{ip}$. As a result, it is sufficient to consider only the positive switching function, denoted as $s_i = s_{ip}$, to represent the switching function of the converter.

Additionally, the duty-cycles for the primary-side and secondary-side bridges are represented by D_1 and D_2, respectively. The variable D_3 is determined by the rising edges of the driving pulses between the primary-side and secondary-side bridges. Finally, D_ϕ is determined by the center of the driving pulses between the two bridges.

The phase-shift (PS) modulation is the conventional modulation scheme used for DAB3. The three-phase legs of each bridge are operated with a phase shift of 120°, and the switches have a duty-cycle of 50% ($D_1 = D_2 = 0.5$), similar to PS modulation for

the DAB1. A phase shift ϕ is added between the input and output sides, which generates different current shapes for $\phi < \pi/3$ and $\phi > \pi/3$, where $D_\phi = \phi/2\pi$ [23]. For instance, Figure 2.1 (a) and (b) respectively illustrate an example for $\phi < \pi/3$ and for $\phi > \pi/3$.

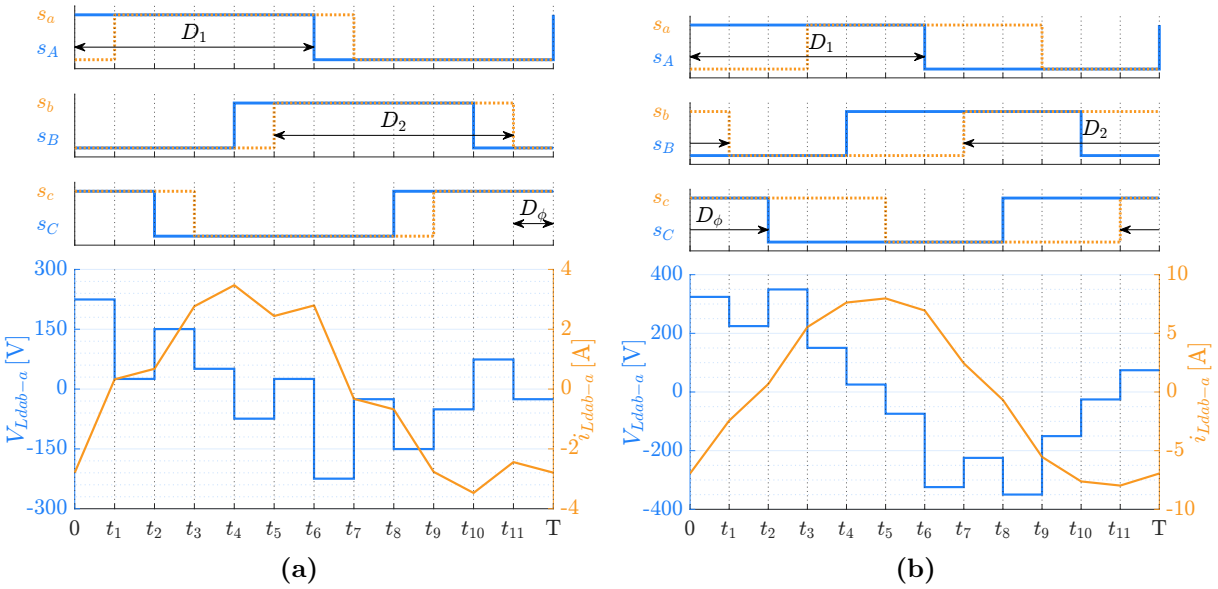

Figure 2.1 – PS modulation with (a) $\phi = 30°$ (b) $\phi = 90°$

PS modulation has advantages that include its ease of implementation and inherent ZVS capability, without requiring any auxiliary element. However, the power conversion efficiency and ZVS range of this modulation scheme decreases when the voltage conversion ratio deviates from unity [23].

The asymmetrical duty-cycle control method, presented in [24], enables SS of the DAB3 converter under partial load conditions while reducing the rms current in the filter. The pulse width of the zero-voltage state is adjusted by controlling the duty-cycle of the top devices in the input and output bridges to achieve ZCS. The duty-cycles D_1 and D_2 can be varied between 0 and 1/3. In the DAB3 converter, different modulation schemes, such as triangular and trapezoidal current modes, are utilized to achieve ZCS. The modulation scheme, known as the Triangular Current Mode Buck Operation (TRI Buck), is used to step down the input voltage in light load conditions ($d < 1$), as shown in Figure 2.2 (a). The modulation scheme, called the Triangular Current Mode Boost Operation (TRI Boost), is used to step up the input voltage in low load conditions ($d > 1$), as shown in Figure 2.2 (b). Lastly, the Trapezoidal Current Mode (TRAP) is employed to transfer more power compared to the TRI Buck and TRI Boost modulation, as depicted in Figure 2.2 (c). The TRAP mode introduces a larger load angle to generate trapezoidal mode phase current.

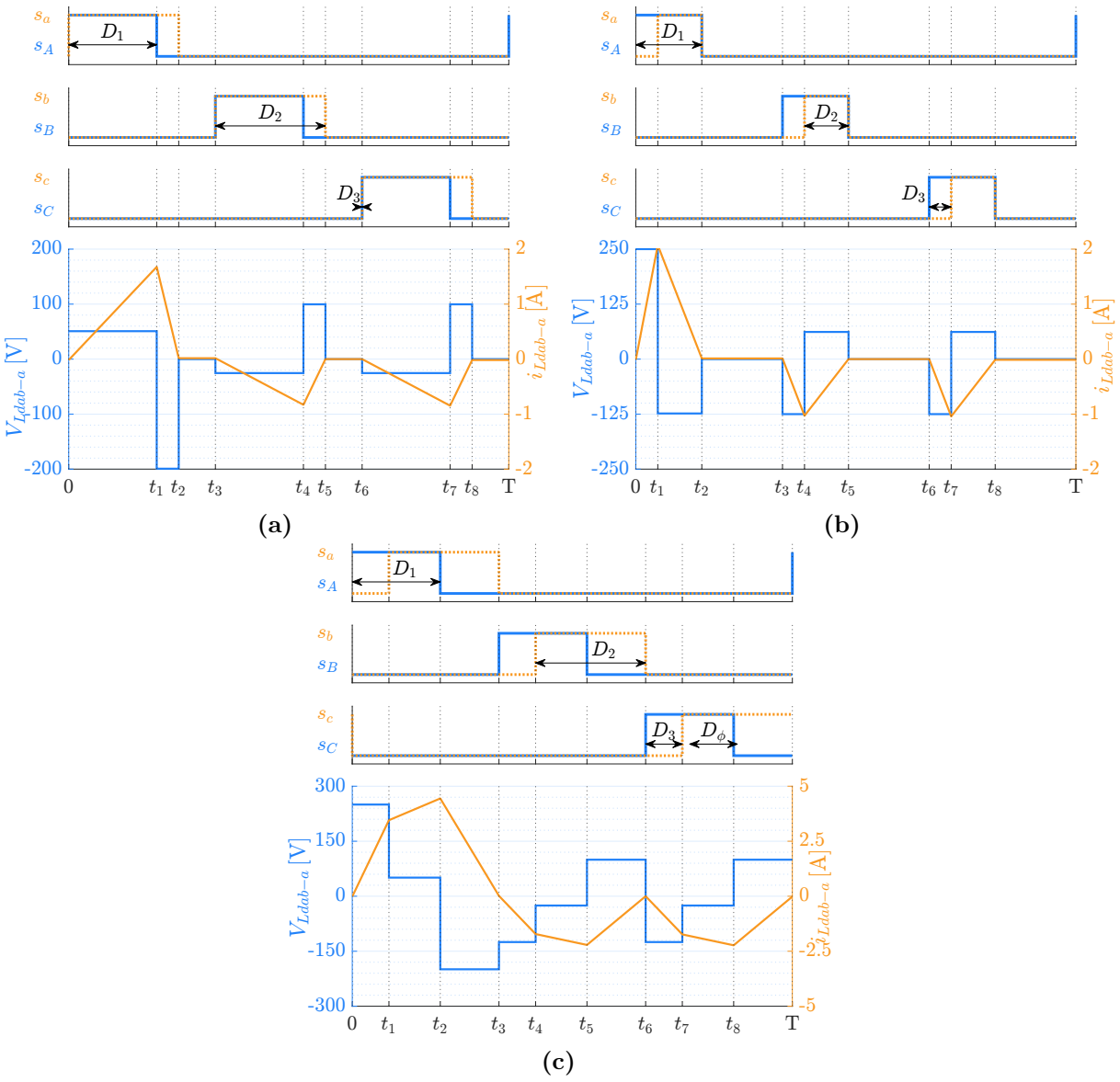

Figure 2.2 – (a) TRI buck modulation (b) TRI boost modulation (c) TRAP modulation

Some modulation strategies for the DAB3 aim to solve the problem of poor partial load efficiency. For example, in [25], this approach involves operating two phases in parallel under low and medium loads, thereby functioning as a DAB1 with high efficiency using the triangular and trapezoidal current modes. PS control is still applied at high loads, but the converter loses the benefit of small ripple output current due to non-interleaved operation. However, this approach requires highly synchronized gate triggering circuits and periodic changes in paralleled phases, increasing control complexity [25]. Figure 2.3 presents this modulation, in which the phase B and C are put in parallel, the first one uses PS modulation and the second one uses TRAP modulation.

In [26], an optimized hybrid modulation scheme designed to minimize total power losses in a DAB3 converter under varying load and voltage conditions is presented. By integrating traditional PS modulation with the strategic application of zero-vector (ZV) voltage in the switching sequence, this modulation strategy achieves SS transitions, reduces

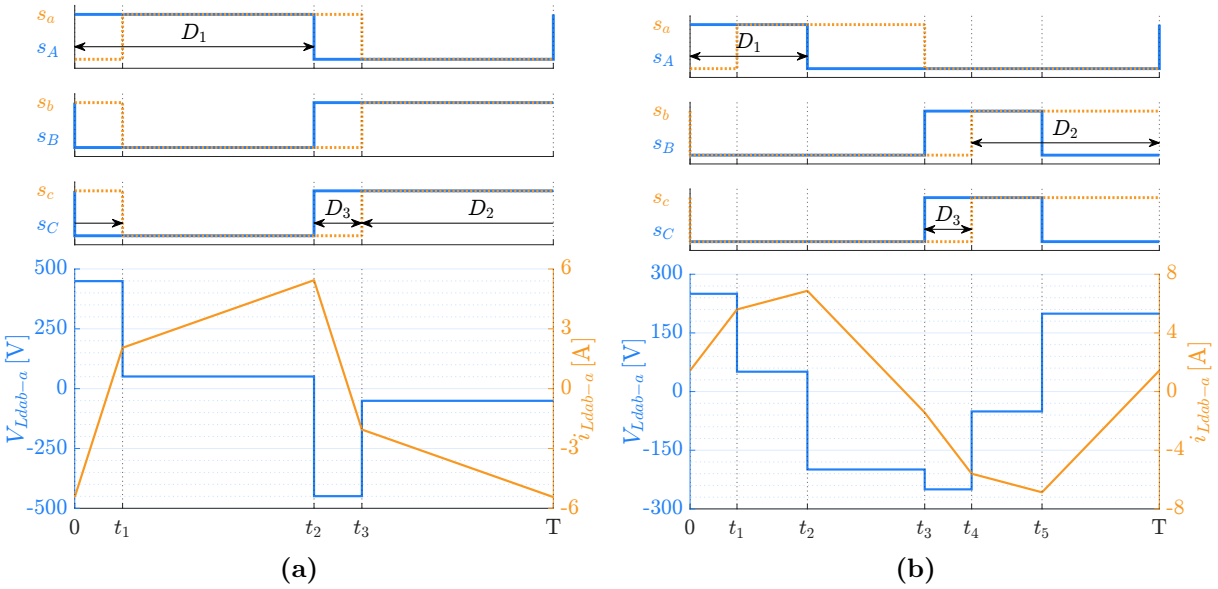

Figure 2.3 – DAB3 operating as a DAB1 using (a) PS modulation and (b) TRAP modulation

rms current, and lowers switching losses.

In [27], the variables D_1, D_2, and D_3 are varied, resulting in a total of 7 operating modes. These modes are analyzed, and a lookup table is generated to determine the optimal operating point for the converter. This approach allows for achieving maximum efficiency among possible combinations. Similarly, in [28], the same method is applied, although the approach to determining the points of maximum efficiency differs.

Another option is Burst-Mode, which facilitates intermittent power transfer during light-load operation. This strategy enhances the light-load power converters efficiency by minimizing switching losses. Transistors cyclically turn ON and OFF at fixed frequencies to generate a burst of pulses that can be transferred to the output [29].

2.2 THREE-PHASE NETWORK

There are several options for the three-phase system connecting the two three-phase inverters. In [30], a comparison is presented between three transformer winding configurations: YY, YD, and DD. Each configuration was analyzed to understand the stress on converter components, such as switches, transformers and filter capacitors. The YY and DD configurations demonstrated similar performance, with the DD configuration exhibiting approximately $\sqrt{3}$ times lower winding current when compared to YY. Conversely, the YD configuration displayed a broader ZVS region at lower power levels and a constant turn-off current for low powers. This characteristic ensures ZVS even with zero phase-shift, making the YD configuration advantageous in certain operating conditions [30].

Another transformer arrangement is presented in [31], the YDe transformer. This type of transformer winding is able to provide a lagging angle between the primary and secondary transformer voltages. With the introduction of this configuration, the DAB3

efficiency under light-load conditions is significantly improved while maintaining a simple control approach. The analysis is done with the PS modulation, demonstrating the superior efficiency of YDe configuration when compared to traditional YY and YD configurations.

Before analyzing the configurations used in this work, the transformer model employed is presented. Figure 2.4 (a) illustrates the T model, a simplified transformer equivalent circuit; in this study, the model is further simplified by neglecting the resistances. This assumption relies on the small values of R_{tr1} and R_{tr2} compared to other parameters, along with the largeness of R_m. Consequently, this yields the model presented in Figure 2.4 (b).

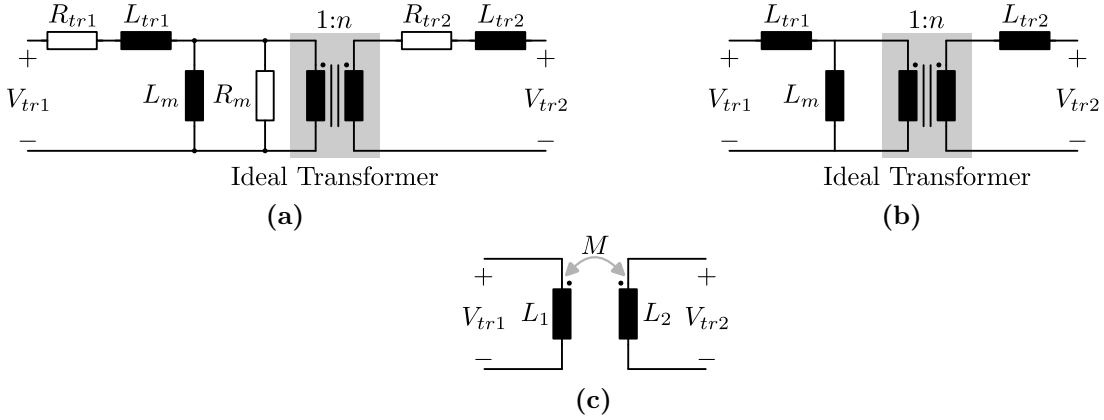

Figure 2.4 – Transformer equivalent circuit (a) T-type [32] (b) Simplification I (c) Simplification II

Figure 2.4 (b) and (c) actually show two approaches to describe the same circuit. The model in Figure 2.4 (b) considers the leakage and mutual inductances together with an ideal transformer, while Figure 2.4 (c) models the transformer based on a coupled inductor. The relationships

$$\begin{cases} L_1 = L_{tr1} + L_m \\ L_2 = L_{tr2} + L_m n^2 \\ M = L_m n \end{cases} \quad \begin{cases} L_{tr1} = L_1 - M/n \\ L_{tr2} = L_2 - Mn \\ L_m = M/n \\ n = \sqrt{L_2/L_1} \end{cases} \tag{2.2}$$

are used to transition from one model to another. In this work, the models depicted in Figure 2.4 (b) and (c) are employed.

This study investigates various transformer plus auxiliary inductor (L_{dab}) combinations, referred as 3ϕ networks in this work. It is considered the delta (D) and wye (Y) for the secondary side. On the primary side, an additional degree of freedom is present due to the auxiliary inductor. Three options are considered: Y, D with the auxiliary inductor inside the coil (iD), and D with the auxiliary inductor outside the coil (oD). These arrangements, presented in Figure 2.5, are denoted as YY, YD, oDY, oDD, iDY,

and iDD in this study.

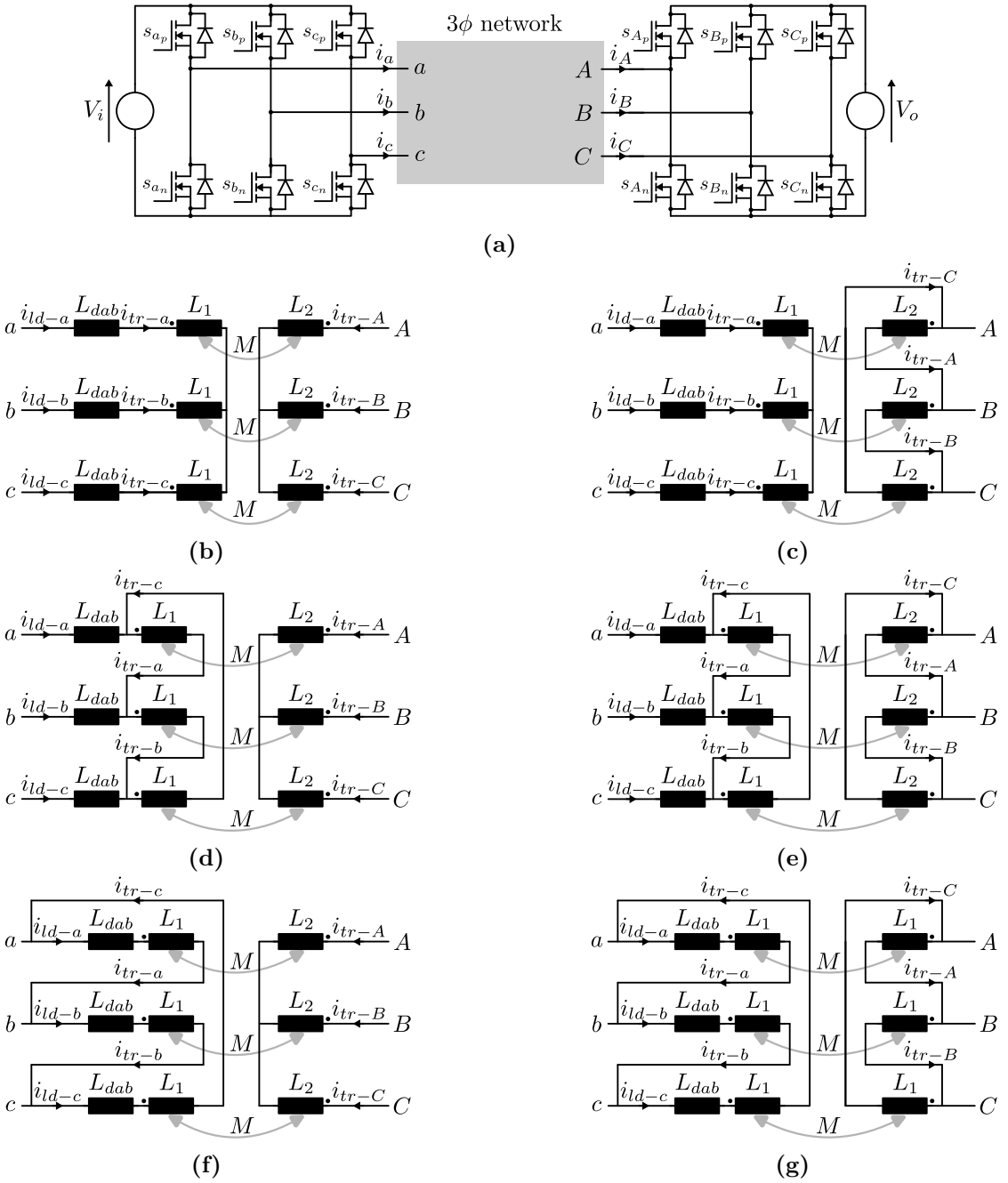

Figure 2.5 – (a) DAB3 with a generic 3ϕ network. Options of 3ϕ network: (b) YY, (c) YD, (d) oDY, (e) oDD, (f) iDY and (g) iDD

2.3 DAB3 ANALYTICAL ANALYSIS

The subsequent section delineates the methodology employed for computing stresses in the converter utilizing PS modulation. The procedure for one of the transformer arrangements is expounded, which was subsequently applied to all other transformers. Utilizing converter stress equations, graphs are generated to demonstrate the behavior of relevant quantities in the converter. In this section, the analytical equations for the oDY

transformer are derived. However, it is important to note that this procedure is equally applicable to all transformers, with only basic equations being adjusted accordingly.

From Figure 2.5, it is possible to verify the nomenclatures used, which are:

- i_x: The currents flowing out of the primary transistor leg , where x can be a, b, or c;
- i_X: The currents that enter the secondary transistor leg, where X can be A, B, or C;
- i_{tr-x}: The transformer primary currents, where x can be a, b, or c;
- i_{tr-X}: The transformer secondary currents, where X can be A, B, or C;
- i_{ld-x}: The currents in the inductor L_{dab}, where x can be a, b, or c.

It is used the switching function presented in Equation 2.1. This switching function is independent of the 3ϕ network, for a single inverter being described as

$$\left[\begin{array}{c} \mathbf{s}_{inv} \\ \hdashline \mathbf{ang}_{inv} \end{array}\right] = \left[\begin{array}{cccccc} 1 & 1 & 1 & 0 & 0 & 0 \\ 0 & 0 & 1 & 1 & 1 & 0 \\ 1 & 0 & 0 & 0 & 1 & 1 \\ \hdashline 0 & \frac{\pi}{3} & \frac{2\pi}{3} & \pi & \frac{4\pi}{3} & \frac{5\pi}{3} \end{array}\right]. \tag{2.3}$$

Since the DAB3 uses two three-phase inverters, and assuming that the secondary lags the primary, the switching function, along with the angle for each switching, can be described as

$$\left[\begin{array}{c} \mathbf{s}_{abc} \\ \hdashline \mathbf{s}_{ABC} \\ \hdashline \mathbf{ang} \end{array}\right] = \left[\begin{array}{c} \mathbf{s}_a \\ \mathbf{s}_b \\ \mathbf{s}_c \\ \hdashline \mathbf{s}_A \\ \mathbf{s}_B \\ \mathbf{s}_C \\ \hdashline \mathbf{ang} \end{array}\right] = \left[\begin{array}{cccccccccccc} 1 & 1 & 1 & 1 & 1 & 1 & 0 & 0 & 0 & 0 & 0 & 0 \\ 0 & 0 & 0 & 0 & 1 & 1 & 1 & 1 & 1 & 1 & 0 & 0 \\ 1 & 1 & 0 & 0 & 0 & 0 & 0 & 0 & 1 & 1 & 1 & 1 \\ \hdashline 0 & 1 & 1 & 1 & 1 & 1 & 1 & 0 & 0 & 0 & 0 & 0 \\ 0 & 0 & 0 & 0 & 0 & 1 & 1 & 1 & 1 & 1 & 1 & 0 \\ 1 & 1 & 1 & 0 & 0 & 0 & 0 & 0 & 0 & 1 & 1 & 1 \\ \hdashline 0 & \phi & \frac{\pi}{3} & \phi+\frac{\pi}{3} & \frac{2\pi}{3} & \phi+\frac{2\pi}{3} & \pi & \phi+\pi & \frac{4\pi}{3} & \phi+\frac{4\pi}{3} & \frac{5\pi}{3} & \phi+\frac{5\pi}{3} \end{array}\right]. \tag{2.4}$$

This switching function depends on the angle applied between the two inverters, and Equation 2.4 presents the case where the angle is between $0° < \phi < 60°$.

With the switching function, it is possible to define the input vector

$$\mathbf{u} = \left[\begin{array}{c} \mathbf{s}_{abc} \\ \hdashline \mathbf{s}_{ABC} \end{array}\right] \left[\begin{array}{c} V_i \\ \hdashline V_o \end{array}\right]. \tag{2.5}$$

Another simplification is considered for the transformers. It is assumed that the coupling occurs only within the same phase, and the coupling between different phases is null and the equivalent circuit is composed by three single-phase transformers connected. Considering this, it is possible to describe the voltages of each coil as a function of the currents as

$$\begin{bmatrix} V_{L_{1a}} \\ V_{L_{1b}} \\ V_{L_{1c}} \\ V_{L_{2a}} \\ V_{L_{2b}} \\ V_{L_{2c}} \end{bmatrix} = \begin{bmatrix} L_1 & 0 & 0 & M & 0 & 0 \\ 0 & L_1 & 0 & 0 & M & 0 \\ 0 & 0 & L_1 & 0 & 0 & M \\ M & 0 & 0 & L_2 & 0 & 0 \\ 0 & M & 0 & 0 & L_2 & 0 \\ 0 & 0 & M & 0 & 0 & L_2 \end{bmatrix} \frac{\mathrm{d}}{\mathrm{d}t} \begin{bmatrix} i_{tr-a} \\ i_{tr-b} \\ i_{tr-c} \\ i_{tr-A} \\ i_{tr-B} \\ i_{tr-C} \end{bmatrix}. \tag{2.6}$$

Given the presented equations, it is possible to isolate the derivatives of the states and obtain the following matrix of derivatives

$$\frac{\mathrm{d}}{\mathrm{d}t} \begin{bmatrix} i_{tr-a} \\ i_{tr-b} \\ i_{tr-c} \\ i_{tr-A} \\ i_{tr-B} \\ i_{tr-C} \end{bmatrix} = \begin{bmatrix} \frac{V_i(3L_2\mathbf{s}_a - 3L_2\mathbf{s}_b - 2Md\mathbf{s}_A + Md\mathbf{s}_B + Md\mathbf{s}_C)}{-3M^2+3L_1L_2+9L_2L_{dab}} \\ \frac{V_i(3L_2\mathbf{s}_b - 3L_2\mathbf{s}_c + Md\mathbf{s}_A - 2Md\mathbf{s}_B + Md\mathbf{s}_C)}{-3M^2+3L_1L_2+9L_2L_{dab}} \\ \frac{V_i(3L_2\mathbf{s}_c - 3L_2\mathbf{s}_a + Md\mathbf{s}_A + Md\mathbf{s}_B - 2Md\mathbf{s}_C)}{3(-M^2+L_1L_2+3L_2L_{dab})} \\ -\frac{V_i(3M\mathbf{s}_a - 3M\mathbf{s}_b - 2L_1d\mathbf{s}_A + L_1d\mathbf{s}_B + L_1d\mathbf{s}_C - 6L_{dab}d\mathbf{s}_A + 3L_{dab}d\mathbf{s}_B + 3L_{dab}d\mathbf{s}_C)}{3(-M^2+L_1L_2+3L_2L_{dab})} \\ -\frac{V_i(3M\mathbf{s}_b - 3M\mathbf{s}_c + L_1d\mathbf{s}_A - 2L_1d\mathbf{s}_B + L_1d\mathbf{s}_C + 3L_{dab}d\mathbf{s}_A - 6L_{dab}d\mathbf{s}_B + 3L_{dab}d\mathbf{s}_C)}{3(-M^2+L_1L_2+3L_2L_{dab})} \\ -\frac{V_i(3M\mathbf{s}_c - 3M\mathbf{s}_a + L_1d\mathbf{s}_A + L_1d\mathbf{s}_B - 2L_1d\mathbf{s}_C + 3L_{dab}d\mathbf{s}_A + 3L_{dab}d\mathbf{s}_B - 6L_{dab}d\mathbf{s}_C)}{3(-M^2+L_1L_2+3L_2L_{dab})} \end{bmatrix}. \tag{2.7}$$

Here, the derived states are expressed as functions of both other states and the switching functions, where each switching function is represented as a vector of 12 positions, presented in Equation 2.4.

With all the differential equations, it is possible to calculate all the static equations using

$$x(t) = e^{\mathbf{A}t}\mathrm{x}(0) + \int_0^t e^{\mathbf{A}(t-\tau)}\mathbf{B}\mathbf{u}(\tau)d\tau. \tag{2.8}$$

Where $\mathbf{A}$ is the transition matrix that represents the dependence of each state derivative with other state. Since there is no dependence, this matrix is equal to zero. $\mathbf{B}$ is the transition matrix that represents the dependence of each state derivative with the switching functions. Since $\mathbf{A} = 0$, Equation 2.8 can be written as

$$x(t) = \mathrm{x}(0) + \int_0^t \mathbf{B}\mathbf{u}(\tau)d\tau. \tag{2.9}$$

The states to be solved are

$$\mathbf{x} = \begin{bmatrix} i_{tr-a} & i_{tr-b} & i_{tr-A} & i_{tr-B} \end{bmatrix}^T, \tag{2.10}$$

all other states are linearly dependent on these states. Upon solving, it is obtained the state current in each position for each current, $\mathbf{x}$ is 4×12. After solving the equations to obtain the steady-state values, it is assumed that the average value of the state variables is zero. One way to achieve this is assuming that the initial current is equal to the negative current in the middle of period, by considering that

$$\mathbf{x}_{(:,1)} = -\mathbf{x}_{(:,7)}. \tag{2.11}$$

Due to the equations size, most of them are presented in Appendix A. In the following analysis, graphs are used to present the converter behavior. The parameters shown in Table 2.1 are considered for the graphs.

Table 2.1 – Parameters for simulation

Parameters	Value	Parameters	Value
V_i	400 V	ϕ	15 °
V_o	300 V	L_{dab}	60 μH
P_o	780 W	L_{tr1}	2 μH
f_s	100 kHz	L_{tr2}	2 μH
n	1	L_m	0.5 mH

With steady-state states, the following integrals are applied

$$i_{rms} = \sqrt{\frac{1}{T}\int_0^t i(t)^2 \mathrm{d}t} \qquad\qquad i_o = \frac{1}{T}\int_0^t i(t)\mathrm{d}t. \tag{2.12}$$

to obtain the RMS current and the average current, respectively.

2.3.1 States current

Figure 2.6 (a) presents the current and voltage in the transformer primary, while Figure 2.6 (b) displays the current and voltage in the transformer secondary. From the state current, all other currents in the converter can be described. For example, the current in the inductor for this 3ϕ network can be represented as

$$[i_{ld-a} \quad i_{ld-b} \quad i_{ld-c}]^T = [i_{tr-a} \quad i_{tr-b} \quad i_{tr-c}]^T - [i_{tr-c} \quad i_{tr-a} \quad i_{tr-b}]^T, \tag{2.13}$$

which results in the current and voltage profiles presented in Figure 2.6 (c).

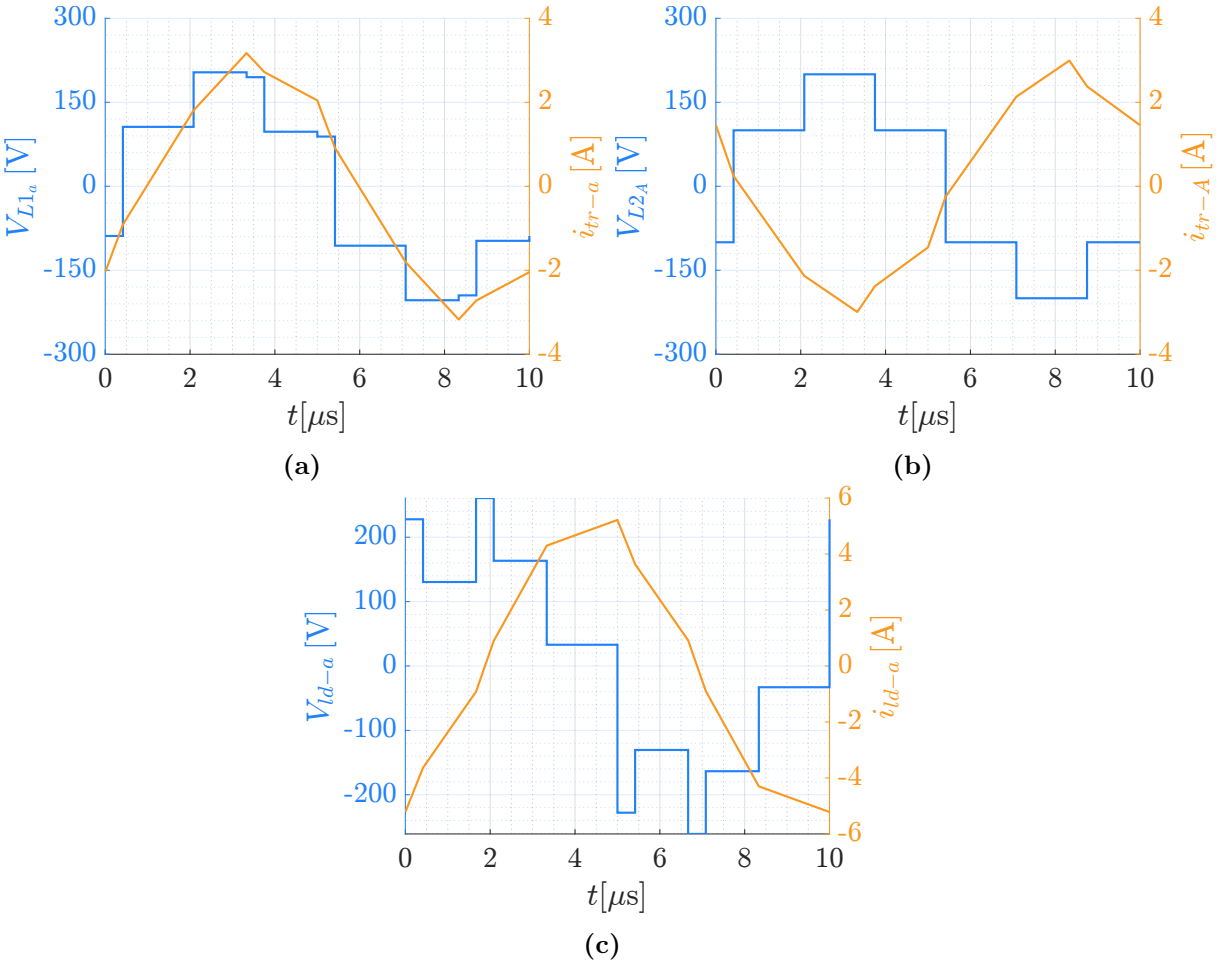

Figure 2.6 – (a) Voltage and current applied to the primary of the transformer (b) Voltage and current applied to the secondary of the transformer (c) Voltage and current applied to the inductor

2.3.2 Output current and output power

The output current of the converter is formed by the current supplied to each half bridge. For the transformer oDY, the relationship between the current on each secondary half bridge and the secondary transformer current is given by

$$[i_A \; i_B \; i_C]^T = -[i_{trA} \; i_{trB} \; i_{trC}]^T. \tag{2.14}$$

It is possible to obtain the output current extracting the part that describes the switching functions of the output stage ($\mathbf{s}_{ABC}$), presented in Equation 2.4, which is

$$\mathbf{s}_{ABC} = \begin{bmatrix} 0 & 1 & 1 & 1 & 1 & 1 & 1 & 0 & 0 & 0 & 0 & 0 \\ 0 & 0 & 0 & 0 & 0 & 1 & 1 & 1 & 1 & 1 & 1 & 0 \\ 1 & 1 & 1 & 0 & 0 & 0 & 0 & 0 & 0 & 1 & 1 & 1 \end{bmatrix}. \tag{2.15}$$

For example, from $\mathbf{s}_{ABC}$, it can be seen that during the second and third stages, the switching function is $(1;0;1)^T$, and phase B is the only one with a switching function of 0. It can be inferred that the current flows through the bottom switch of phase B and returns through phases A and C. Therefore, it is possible to describe the output current during the second and third stages as the current entering the secondary half bridge of phase B ($-i_B$). Similarly, all other stages can be described by the current of one of the phases, whether it is negative or positive. This effect is illustrated in Figure 2.7.

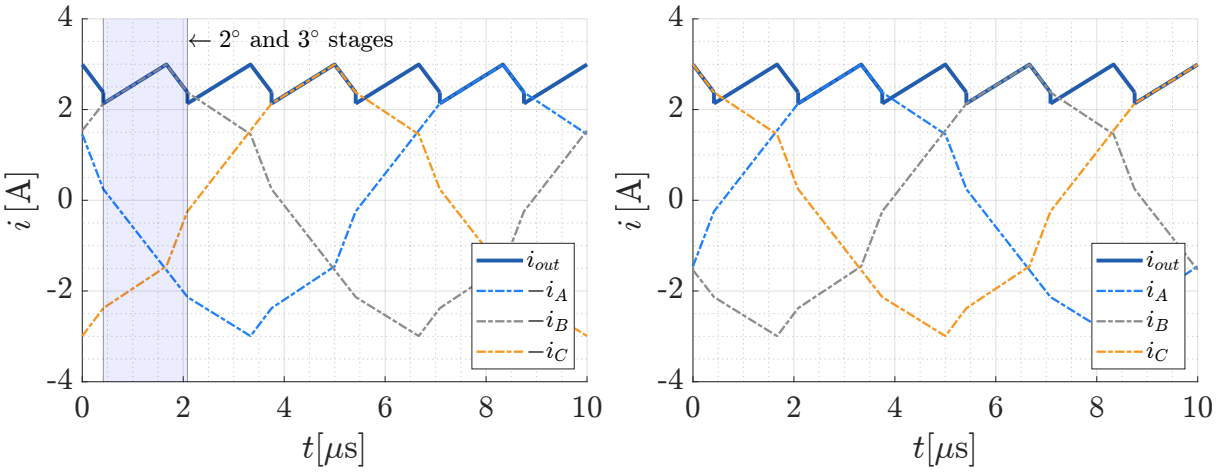

Figure 2.7 – Converter output current (i_{out}) with (a) the transformer secondary currents (i_A, i_B and i_C) or (b) the negative transformer secondary currents ($-i_A$, $-i_B$ and $-i_C$)

It is possible to obtain the average output current by

$$I_o = \begin{cases} \frac{M\,V_i\,(6\,\phi+\pi)}{12\,f_s\,\pi\,(-M^2+L_1\,L_2+3\,L_2\,L_{dab})} & \text{if } -60° \leq \phi < 0° \\ \frac{M\,V_i\,\left(-9\,\phi^2+6\,\pi\,\phi+\pi^2\right)}{12\,f_s\,\pi^2\,(-M^2+L_1\,L_2+3\,L_2\,L_{dab})} & \text{if } 0° \leq \phi \leq 60° \end{cases} \tag{2.16}$$

and the average output power by

$$P_o = I_o V_o. \tag{2.17}$$

In Figure 2.8, the average output power of the converter for all possible angles is presented. First, it can be concluded that the converter has positive power transfer between angles -30 ° to 150 °, and negative transfer between angles -180 ° to -30 ° and 150 ° to 180 °, proving the bidirectionality of the converter.

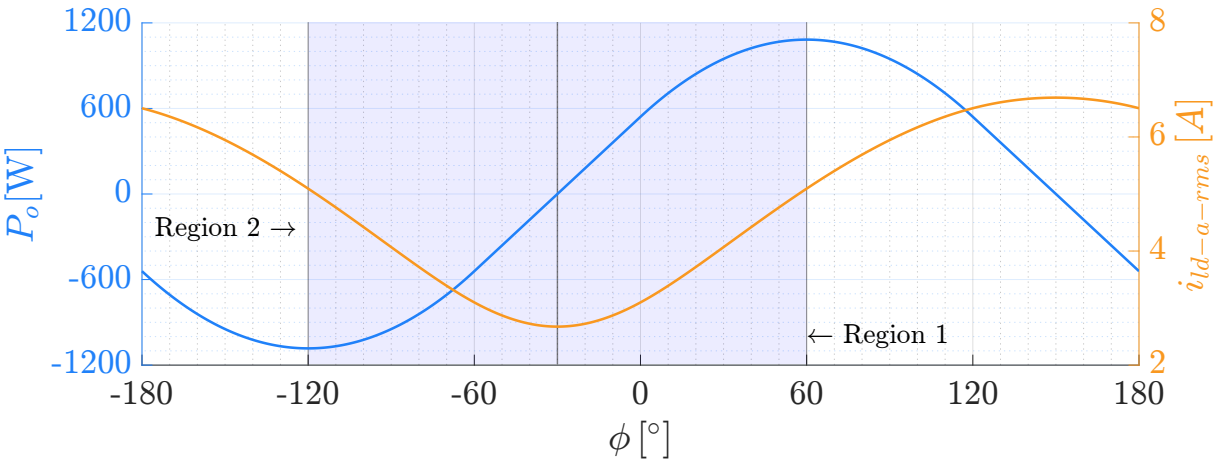

Figure 2.8 – Output power and rms current inductor L_{dab} as function of ϕ

Within the angle range from -30° to 150°, positive power transfer is achieved, and the converter operates effectively. However, beyond 60°, the rms current in the inductor L_{dab} increases significantly. A specific angle range within the positive power transfer region is chosen, known as Region 1, to avoid high inductor currents. This region allows for positive power transfer while maintaining lower inductor current levels. On the other hand, the angle range where negative power transfer occurs and also results in lower inductor rms currents is highlighted as Region 2. For the purposes of this study, the analysis focuses solely on positive power transfer and, therefore, is conducted within Region 1. The exact angle within Region 1 depends on the 3ϕ network configuration used in the converter.

2.3.3 Power switch current

The current in the switches can be described by

$$i_{sw-p} = [i_a \; i_b \; i_c]^T s_{abc}\,, \quad i_{sw-s} = [i_A \; i_B \; i_C]^T s_{ABC}.$$

In Figure 2.9, the behavior of the current flowing through the primary and secondary switches is presented.

The equations provide both the rms current and the current at the instant of switching, given by

$$i_{sw-a-rms} = \begin{cases} \frac{2\,V_i\,(2\,\pi\,M\,d-3\,\pi\,L_2+3\,M\,d\,\phi)-M\,V_i\,d\,(6\,\phi+\pi)}{18\,f_s\,\pi\,(-M^2+L_1\,L_2+3\,L_2\,L_{dab})} & \text{if } -60° \leq \phi < 0° \\ -\frac{2\,V_i\,(3\,\pi\,L_2-2\,\pi\,M\,d+3\,M\,d\,\phi)+M\,V_i\,d\,(3\,\phi+\pi)}{18\,f_s\,\pi\,(-M^2+L_1\,L_2+3\,L_2\,L_{dab})} & \text{if } 0° \leq \phi \leq 60° \end{cases}. \tag{2.18}$$

$$i_{sw-A-rms} = \begin{cases} -\frac{V_i\,(2\,L_1\,d-3\,M+6\,L_{dab}\,d)}{18\,f_s\,(-M^2+L_1\,L_2+3\,L_2\,L_{dab})} & \text{if } -60° \leq \phi < 0° \\ -\frac{V_i\,(9\,M\,\phi-3\,\pi\,M+2\,\pi\,L_1\,d+6\,\pi\,L_{dab}\,d)}{18\,f_s\,\pi\,(-M^2+L_1\,L_2+3\,L_2\,L_{dab})} & \text{if } 0° \leq \phi \leq 60° \end{cases}. \tag{2.19}$$

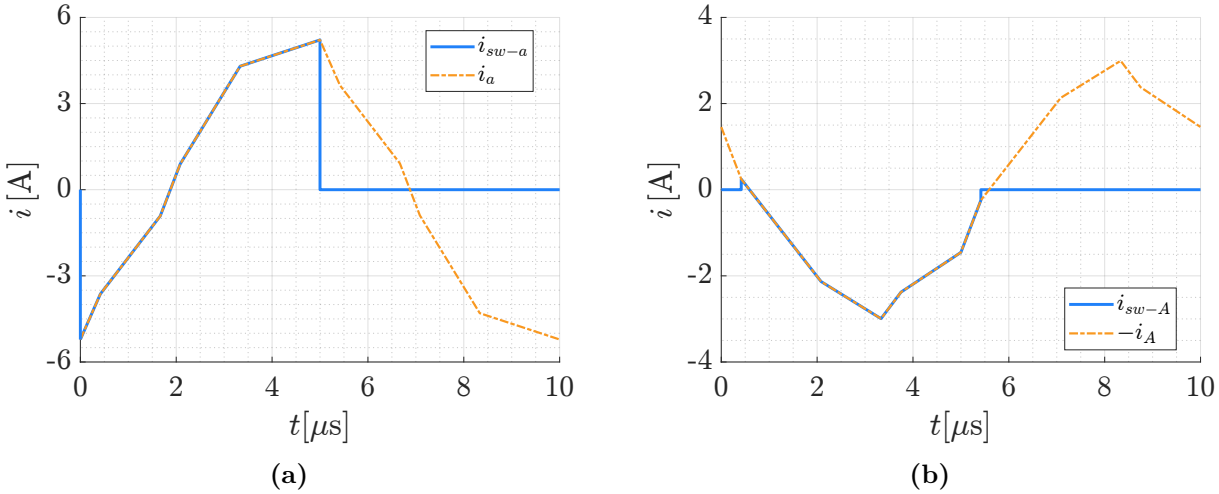

Figure 2.9 – (a) Primary power switch current (i_{sw-a}) and the current the half-bridge current (i_a) (b) Secondary power switch current (i_{sw-A}) and the current the half-bridge current ($-i_A$)

Due to the utilization of PS modulation, which have $D_1 = D_2 = 0.5$, both the primary and secondary power switches exhibit an inherent characteristic where the turn-on current is opposite to the turn-off current. This behavior is clearly depicted in Figure 2.9.

For SS operation, the switching must occur at either ZVS or ZCS. In the case of ZVS, ideally, if the output current of a half-bridge is negative at the moment of switching, ZVS is achieved. However, due to the opposite nature of the turn-on and turn-off currents, achieving ZVS during both turn-on and turn-off operations simultaneously is not possible. Therefore, in this work, the system is considered to be in ZVS or SS when ZVS is achieved during turn-on, while it is classified as hard-switching (HS) when ZVS is achieved during turn-off. Figure 2.10 illustrates the regions where ZVS occurs based on the output voltage gain d with respect to the angle ϕ, the output current I_o, or the output power P_o.

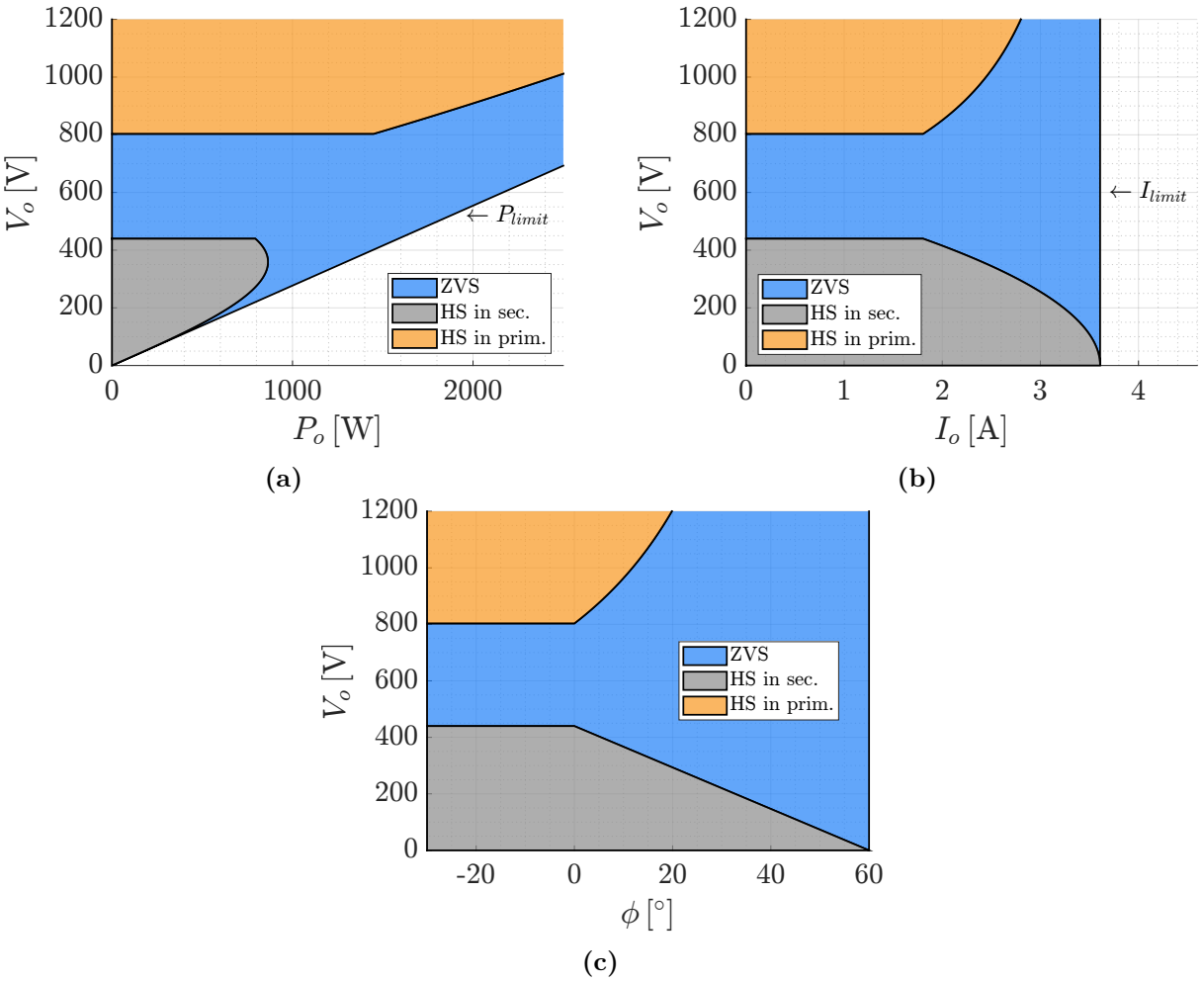

Figure 2.10 – Regions of operation of the converter with output voltage as a function of (a) output power, (b) output current, and (c) angle

2.3.4 Magnetizing inductance effect

The effect of magnetizing inductance is show in Figures 2.11 (a-c). As the inductance decreases, there is a more significant difference in the current flowing from the primary to the secondary of the transformer. However, if the inductance increases, the currents tend to become more similar.

Figure 2.11 (d) provides a comprehensive view of this effect. The lines in the graph show the ratio of the rms current from the primary to the secondary ($i_{tr-A-rms}/i_{tr-a-rms}$) for different operating angles (ϕ) and magnetizing inductance values (L_m). As the inductance increases, this ratio tends to approach 1, which is a situation with an ideal transformer.

The changes in magnetizing inductance influence the currents in the primary and secondary of the transformer, which also flow through the power switches, leading to alterations in current values during switching. Consequently, the ZVS regions are affected, as illustrated in Figure 2.12.

Reducing the magnetizing inductance results in higher currents flowing through the

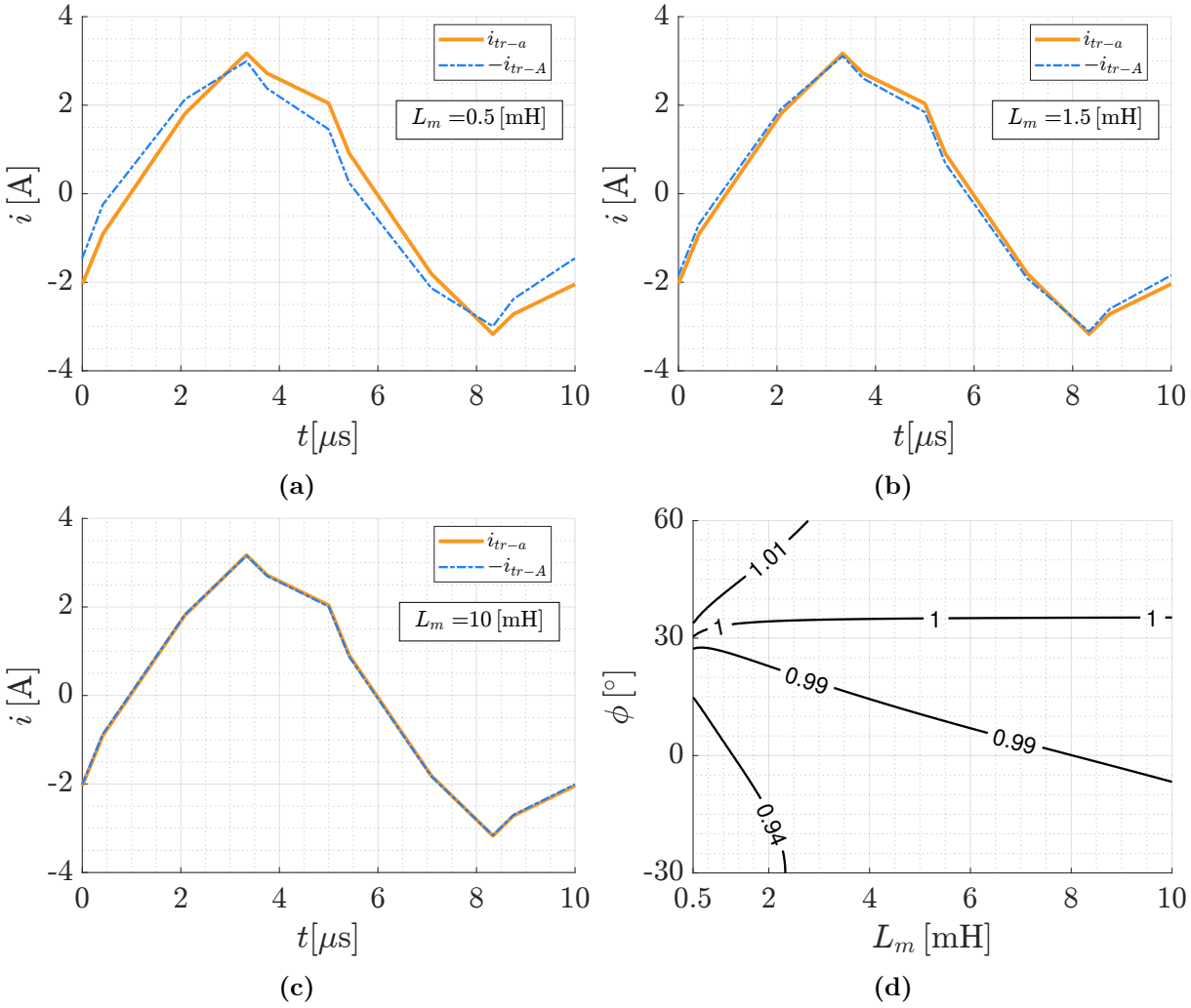

Figure 2.11 – Primary and secondary transformer current for (a) $L_m = 0.5\,\text{mH}$ (b) $L_m = 1.5\,\text{mH}$ (c) $L_m = 10\,\text{mH}$ (d) Ratio of secondary rms current over primary rms current ($i_{tr-A-rms}/i_{tr-a-rms}$) for different operating angles and different L_m ($d = 3/4$)

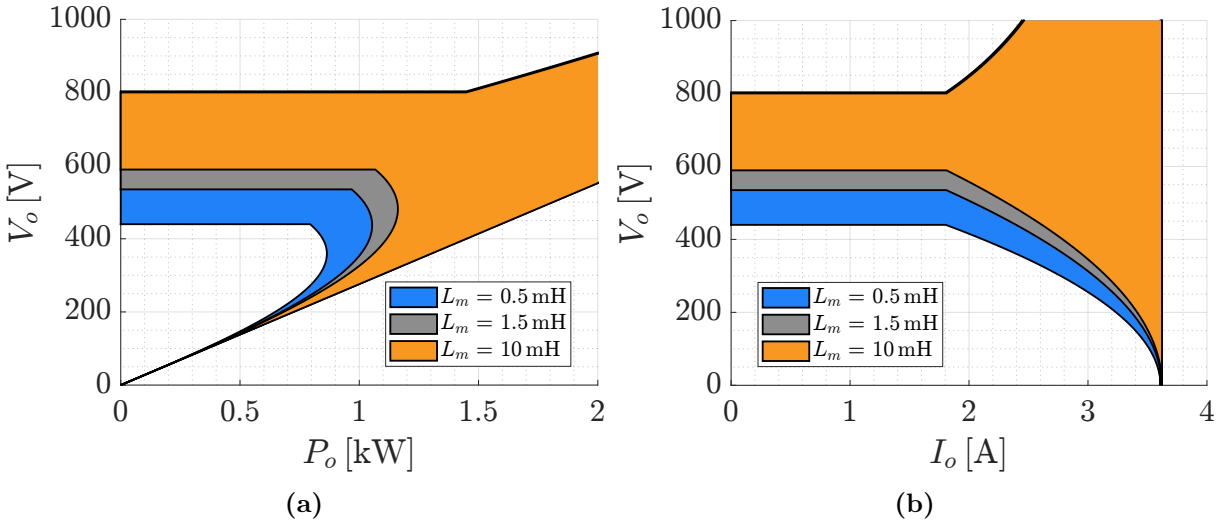

Figure 2.12 – ZVS region for three possible L_m as a function of (a) output power or (b) output current

power switches. However, it also leads to an increased ZVS region, allowing for improved switching performance and efficiency.

2.3.5 DC bus voltage ripple

The calculations performed so far considered a fixed voltage source both at the input and output of the converter. Now, the DC bus voltage ripples at both the input and output of the converter are calculated. This calculation is based on the structure shown in Figure 2.13, using the current equations derived earlier.

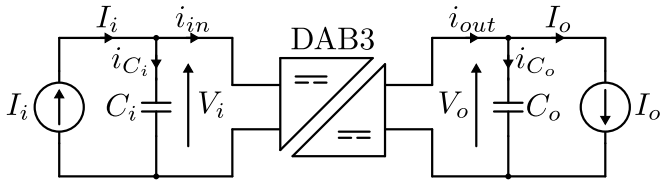

Figure 2.13 – The input and output structure of the DAB3 when fed and supplying a DC current source.

This structure assumes that both capacitors are supplied by DC current sources I_i and I_o, where all average currents flow through them, while the capacitors only handle the alternating currents.

Thus, the capacitor currents can be expressed as

$$i_{C_i} = I_i - i_{in} \qquad\qquad i_{C_o} = i_{out} - I_o. \tag{2.20}$$

By performing the integrals

$$V_i(t) = \frac{1}{C_i}\int i_{C_i}(t)\mathrm{d}t \qquad\qquad V_o(t) = \frac{1}{C_o}\int i_{C_o}(t)\mathrm{d}t, \tag{2.21}$$

it becomes possible to numerically obtain the capacitors voltage. The voltage ripple is given by the peak to peak voltage, named ΔV_i for the input and ΔV_o for the output. The voltage and current waveforms for both the input and output capacitors, with capacitance values of 500 nF each, are shown in Figure 2.14.

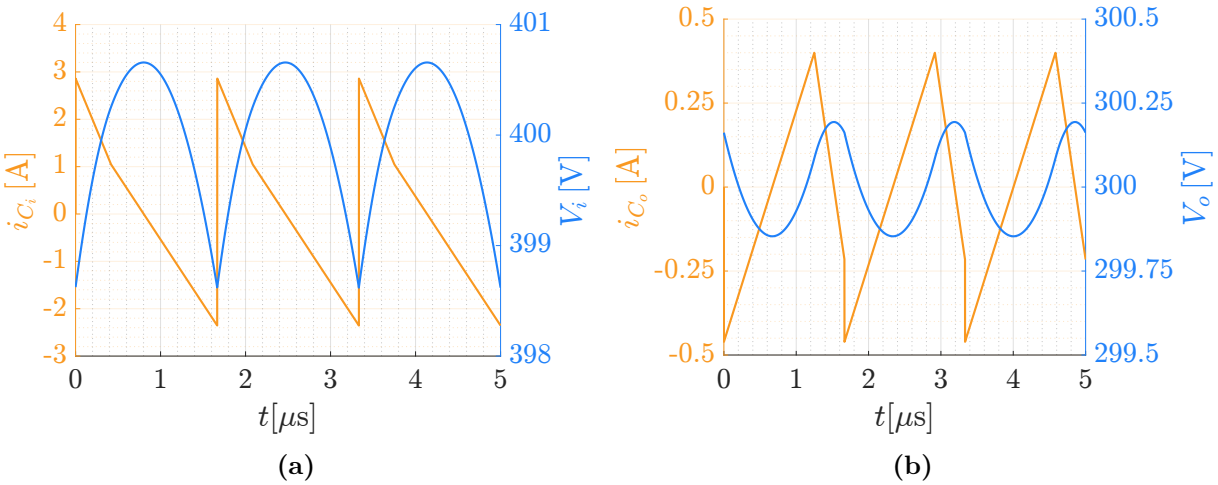

Figure 2.14 – (a) Voltage and current in the input capacitor (C_i) (b) Voltage and current in the output capacitor (C_o)

2.3.6 Theoretical equations versus simulation

The calculation procedure described earlier is applied to all six configurations. The equations accuracy is verified by utilizing parameters provided in Table 2.1 and comparing results with simulations conducted using PLECS 4.7.2. Table 2.2 presents a comparison between output power and RMS current in all elements, obtained from theoretical equations and simulation results.

Table 2.2 – Comparison of theoretical versus simulation current efforts for all 3ϕ networks.

	Transformer YY			Transformer YD		
Parameter	Theoretical	Simulation	Error [%]	Theoretical	Simulation	Error [%]
P_o	486.41 W	486.41 W	0	−778.234 W	−778.273 W	≈ 0
$i_{ld-a-rms}$	1.538 A	1.538 A	0	1.9069 A	1.9069 A	0
$i_{tr-a-rms}$	1.538 A	1.538 A	0	1.9069 A	1.9069 A	0
$i_{tr-A-rms}$	1.3037 A	1.3037 A	0	2.5198 A	2.5198 A	0
$i_{sw-a-rms}$	1.0875 A	1.0875 A	0	1.3484 A	1.3484 A	0
$i_{sw-A-rms}$	0.9218 A	0.9219 A	≈ 0	3.0861 A	3.0859 A	≈ 0
	Transformer oDY			Transformer oDD		
Parameter	Theoretical	Simulation	Error [%]	Theoretical	Simulation	Error [%]
P_o	778.171 W	778.174 W	≈ 0	507.503 W	507.506 W	≈ 0
$i_{ld-a-rms}$	3.5524 A	3.5524 A	0	1.6048 A	1.6048 A	0
$i_{tr-a-rms}$	2.0510 A	2.0509 A	≈ 0	0.9265 A	0.9265 A	0
$i_{tr-A-rms}$	1.9294 A	1.9294 A	0	0.7320 A	0.7320 A	0
$i_{sw-a-rms}$	2.5119 A	2.5119 A	0	1.1347 A	1.1374 A	≈ 0
$i_{sw-A-rms}$	1.3643 A	1.3643 A	0	0.8965 A	0.8967 A	≈ 0
	Transformer iDY			Transformer iDD		
Parameter	Theoretical	Simulation	Error [%]	Theoretical	Simulation	Error [%]
P_o	2237.4 W	2237.4 W	0	1459.2 W	1459.2 W	0
$i_{ld-a-rms}$	5.8970 A	5.8970 A	0	2.6639 A	2.6639 A	0
$i_{tr-a-rms}$	5.8970 A	5.8970 A	0	2.6639 A	2.6639 A	0
$i_{tr-A-rms}$	5.7322 A	5.7322 A	0	2.2581 A	2.2581 A	0
$i_{sw-a-rms}$	7.2223 A	7.2223 A	0	3.2626 A	3.2626 A	0
$i_{sw-A-rms}$	4.0533 A	4.0534 A	≈ 0	2.7655 A	2.7661 A	≈ 0

Another simulation is conducted considering the presence of capacitors in both the input and output. Table 2.3 presents the voltage ripple for these capacitors, obtained from the theoretical equations and the simulation results. The errors presented in both Table 2.2 and 2.3 are sufficiently low, confirming the accuracy of these equations for use in the subsequent sections.

Table 2.3 – Comparison of theoretical versus simulation voltage ripple for all 3ϕ networks.

	Transformer YY			Transformer YD		
Parameter	Theoretical	Simulation	Error [%]	Theoretical	Simulation	Error [%]
ΔV_i	32.2 mV	32.0 mV	0.62	34.9 mV	34.9 mV	0
ΔV_o	87.3 mV	87.9 mV	−0.68	296.6 mV	299.1 mV	−0.84
	Transformer oDY			Transformer oDD		
Parameter	Theoretical	Simulation	Error [%]	Theoretical	Simulation	Error [%]
ΔV_i	203.5 mV	204.9 mV	−0.69	91.1 mV	91.8 mV	−0.77
ΔV_o	34.0 mV	33.8 mV	0.59	33.6 mV	34.6 mV	−2.98
	Transformer iDY			Transformer iDD		
Parameter	Theoretical	Simulation	Error [%]	Theoretical	Simulation	Error [%]
ΔV_i	585.2 mV	589.5 mV	−0.73	262.0 mV	263.8 mV	−0.68
ΔV_o	139.2 mV	137.8 mV	1.00	96.7 mV	96.1 mV	0.62

2.4 SWITCHING ANALYSIS

In this section, capacitors are connected in parallel with the power switches to represent a parasitic parameter, and the presence of dead time is taken into account. This allows for the analysis of the switching.

In Figure 2.15, the operation of the converter with the oDY transformer during the dead time is presented. This circuit is valid for an angle between 0° to 60°. Figure 2.15 (a) illustrates the switching of the s_{a_p} switch, where the parasitic capacitors C_{a_p} and C_{a_n} need to discharge and charge, respectively, before the end of the dead time to ensure SS. Figure 2.15 (b) shows the switching of the secondary, with the parasitic capacitors C_{A_p} and C_{A_n} being charged and discharged, respectively.

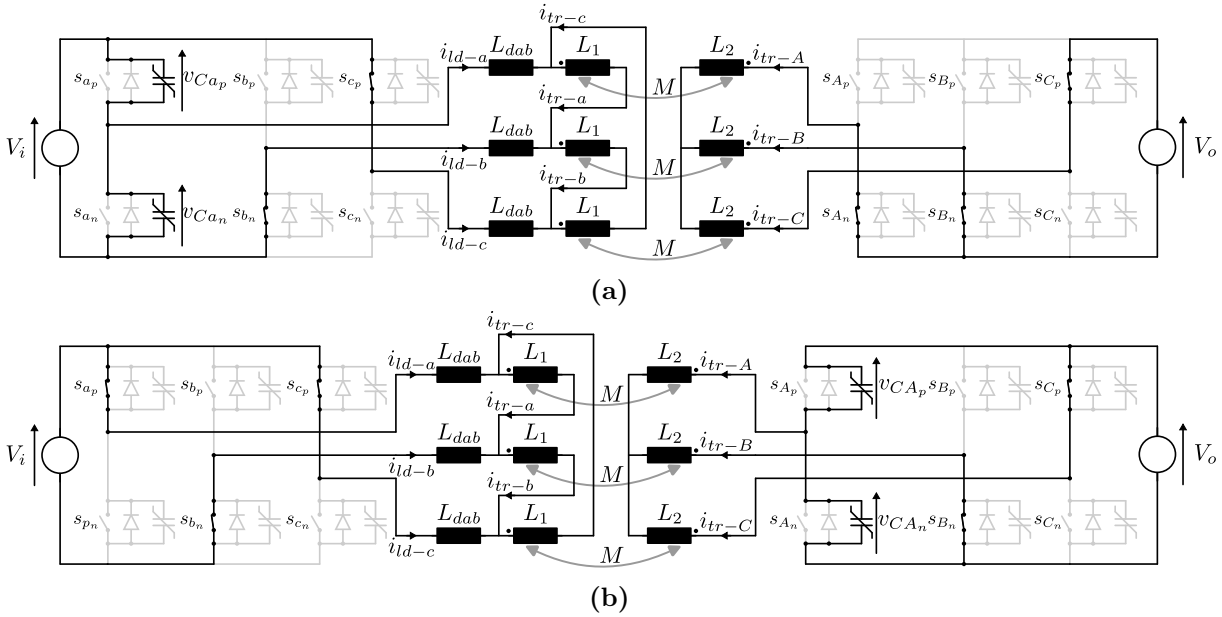

Figure 2.15 – Equivalent circuit during the dead time in ZVS or iZVS mode (a) Primary power switch (a) Secondary power switch

New states are now analyzed. For the primary-side switching, the following states are considered

$$\mathbf{x} = \begin{bmatrix} i_{tr-a} & i_{tr-b} & i_{tr-A} & i_{tr-B} & v_{Ca_p} \end{bmatrix}^T, \tag{2.22}$$

On the other hand, for the secondary-side switching, the following states are considered

$$\mathbf{x} = \begin{bmatrix} i_{tr-a} & i_{tr-b} & i_{tr-A} & i_{tr-B} & v_{CA_p} \end{bmatrix}^T. \tag{2.23}$$

The capacitors, inherent parasitic elements in power switches, exhibit a non-linear capacitance dependent on the voltage across the power switch, V_{ds}. Figure 2.16 (a) illustrates the capacitance as a function of voltage for the C2M0080120D power switch. This particular switch exhibits a maximum capacitance of 720 pF at $V_{ds} = 0\,\text{V}$ and a minimum of 85 pF at $V_{ds} = 1\,\text{kV}$.

It is a common practice to replace this variable capacitor with a fixed one to simplify calculations. Various methods exist for selecting the fixed capacitor [33, 34], such as choosing one with the same stored charge as the variable capacitor. However, these methods assume a constant output current during dead time, which is not true for DAB converter, as it involves currents with high derivatives.

A different approach is adopted in this section. The solutions for both the variable capacitor and its fixed counterpart in the differential equations are calculated. The fixed capacitor, ensuring a similar behavior for both approaches, is deemed a good estimation. This leads to a fixed capacitor value of 420 pF. The discrepancies between these two approaches will be discussed in Figures 2.17 and 2.18.

The switching is analyzed in three ways to investigate this capacitance impact:

- A numerical solution of the differential equations, where the capacitance depends on the voltage itself, as presented in Figure 2.16 (a);
- A numerical solution of the differential equations, considering a fixed capacitance of 420 pF;
- A simulation in PLECS 4.7.2 software, with fixed capacitance of 420 pF in parallel with the power switches.

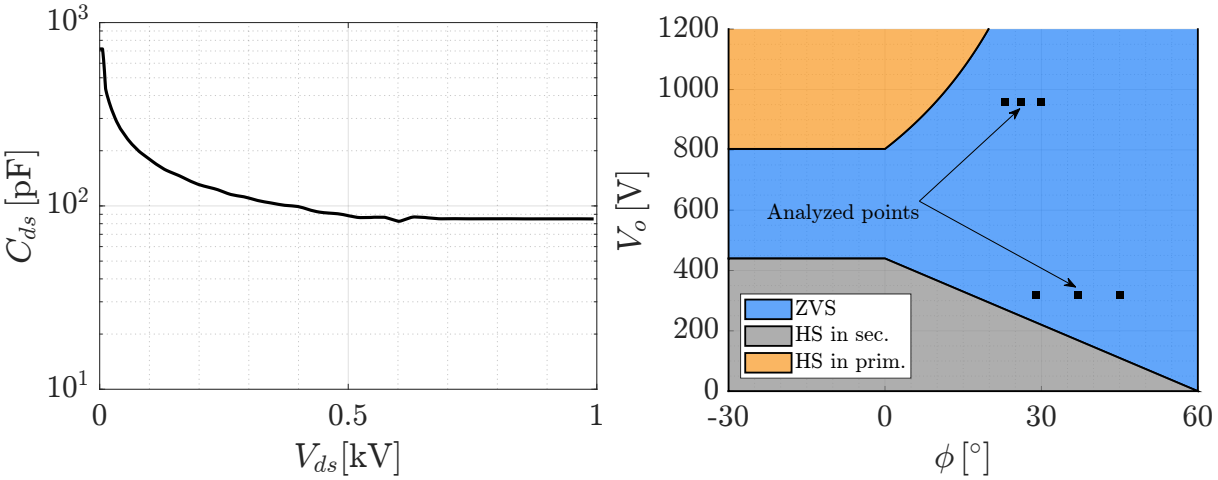

Figure 2.16 – (a) Drain-Source capacitance as a function of Drain-Source voltage for the C2M0080120D power switch [35] (b) ZVS region as a function of voltage V_o and angle ϕ.

As the system may lose ZVS in the primary or secondary side, both scenarios are studied. The loss of ZVS in the primary side is analyzed with the output voltage at 960 V ($d = 2.4$), and angles of 29 °, 37 ° and 45 ° are considered. On the other hand, the loss of ZVS in the secondary side is investigated with an output voltage of 320 V ($d = 0.8$), and angles of 23 °, 26 ° and 30 ° are studied. These points are shown in Figure 2.16 (b), alongside the ideal ZVS boundaries.

The analysis of the secondary-side power switch switching involves observing the voltage behavior across the parasitic capacitor CA_p during the discharging process, as depicted in Figure 2.17 (a), along with the corresponding discharging current, shown in Figure 2.17 (b). Figure 2.17 shows the differences among the three different solutions. It can be concluded that replacing the variable capacitor with a fixed one is a valid approximation. Additionally, the results shows a similar trend in the capacitor voltage behavior to the solutions obtained from the equations.

However, there is a distinction between the simulation and the equation, even with fixed capacitance, due to the converter effective angle when considering the dead time. The dead time and capacitance alteration modify the converter static gain. This difference

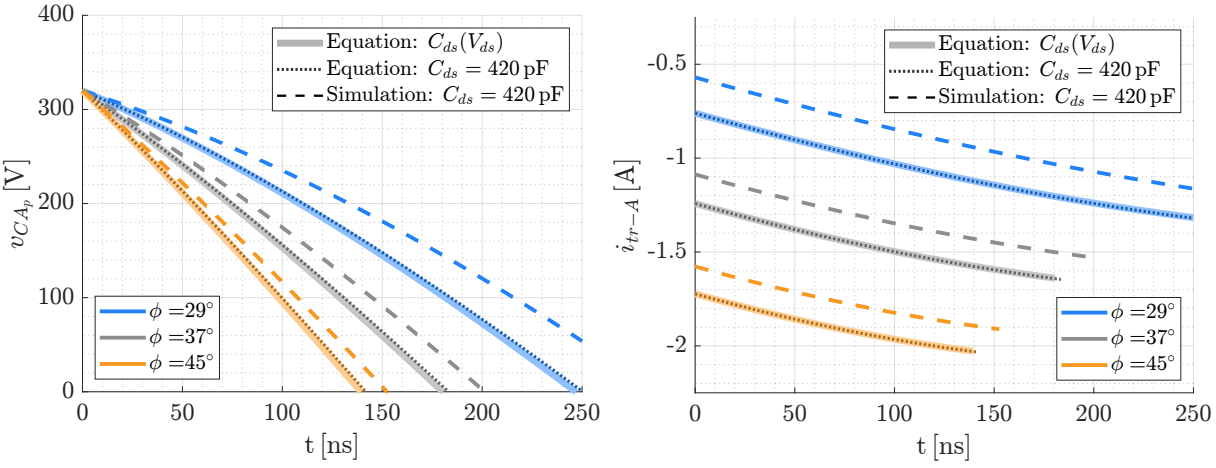

Figure 2.17 – (a) Voltage across the capacitor CA_p during dead time for different operating points (b) Current that discharges the capacitor CA_p.

becomes pronounced as the dead time nears the frequency period. This study does not consider the static gain difference caused by the dead time.

The crucial point to consider is when the voltage reaches 0 V and is subsequently clamped by the body diode, leading to a transition into another operation mode. This duration is essential to determine whether the dead time is long enough to achieve ZVS. The results of this analysis reveal that the minimum dead time required depends on the operating point. For example, with an output voltage of 960 V and with an angle of 37 °, a dead time of 200 ns achieves ZVS, while a dead time of 100 ns is insufficient.

The primary-side power switch switching analysis involves observing the voltage behavior across the parasitic capacitor Ca_p during discharging, at Figure 2.18 (a), and the corresponding discharging current, at Figure 2.18 (b).

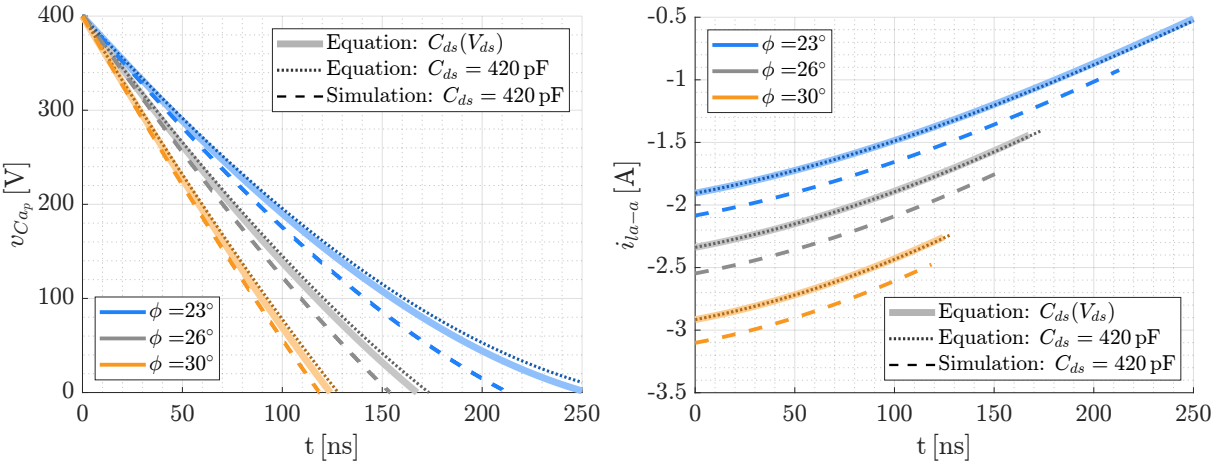

Figure 2.18 – (a) Voltage across the capacitor Ca_p during dead time for different operating points (b) Current that discharges the capacitor Ca_p.

The ideal boundary for achieving ZVS is at an angle of 17 °. However, at this

instant, the current is too low to sufficiently discharge the capacitor Ca_p. Despite not achieving ZVS, the switch operates with a voltage lower than the output voltage V_o. As the angle increases, the initial current becomes larger, leading to a faster discharge of the capacitor $C_{Q_{s1}}$ and the possibility of achieving ZVS. Therefore, it is concluded that the minimum angle for achieving ZVS with an output voltage of 320 V and a dead time of 250 ns is 23 °.

Based on Figures 2.17 and 2.18, it can be observed that a fixed capacitance value can reasonably represent the voltage behavior of the intrinsic capacitor of the power switch during the dead time. An equation is derived to describe the final capacitor voltage as a function of converter parameters and the dead time. This process is made to all 3ϕ network and for all variations in the sequence of commutation function. These equations aren't presented due to their size.

The process to determine the power switch operating mode is illustrated in Figure 2.19. If the initial current is positive, it is assumed to be in HS; if it is negative, it checks whether the voltage over the capacitor at the end of the dead time ($V_{sw}(t_{dt})$) is below zero, which is classified as ZVS. If the voltage surpasses the initial voltage ($V_{sw}(0)$), it is identified as HS. Moreover, if the voltage lies between zero and the initial voltage, it is labeled as iZVS.

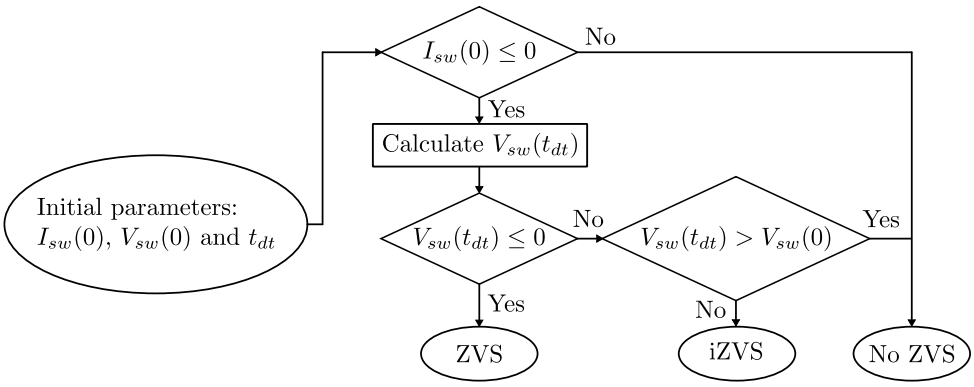

Figure 2.19 – Power switch condition identification flowchart

In this work, the calculation of switching losses involves using the switching energy for a given current and voltage at the switching instant. Further information about the switching energy equation utilized in this study can be found in Appendix C.1.2. Equations

$$E_{on} = \begin{cases} 0 & \text{if ZVS} \\ E_{on}(I_{sw}(0), V_{sw}(t_{dt})) & \text{if iZVS} \\ E_{on}(I_{sw}(0), V_{sw}(0)) & \text{if no ZVS} \end{cases} \tag{2.24}$$

$$E_{off} = \begin{cases} E_{off}(I_{sw}(0), V_{sw}(0)) & \text{if ZVS} \\ E_{off}(I_{sw}(0), V_{sw}(t_{dt})) & \text{if iZVS} \\ 0 & \text{if no ZVS} \end{cases} \tag{2.25}$$

illustrate the methodology for computing the switching loss, taking into account the discharge of the parasitic capacitor. It is assumed that the current variation during the dead time is relatively slow compared to the voltage variation.

From the obtained equations, the regions of ZVS, iZVS, and no ZVS are presented for a range of converter output voltage and output current. The effect of varying both the dead time and the intrinsic capacitance is presented. Figure 2.20 illustrates this situation. It is observed that increasing the dead time leads to a larger ZVS region. On the other hand, the ZVS region decreases as the parasitic capacitor increases. In simpler terms, a smaller parasitic capacitor enables a larger ZVS region.

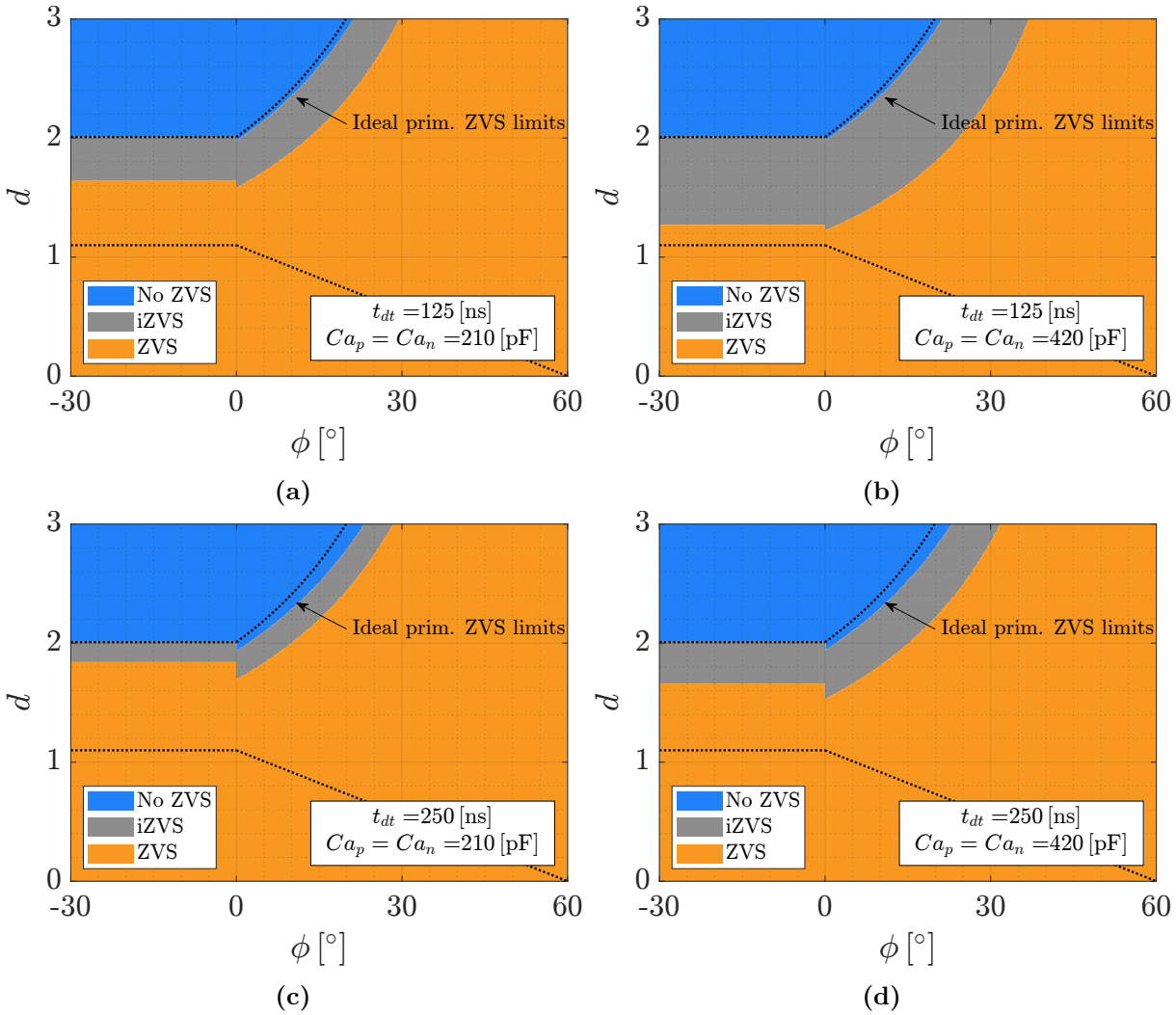

Figure 2.20 – Primary power switches ZVS, iZVS and no ZVS regions as a function of voltage gain d and angle ϕ with (a) $t_{dt} = 125\,\text{ns}$ and $Ca_p = Ca_n = 210\,\text{pF}$ (b) $t_{dt} = 125\,\text{ns}$ and $Ca_p = Ca_n = 420\,\text{pF}$ (c) $t_{dt} = 250\,\text{ns}$ and $Ca_p = Ca_n = 210\,\text{pF}$ (d) $t_{dt} = 250\,\text{ns}$ and $Ca_p = Ca_n = 420\,\text{pF}$.

Figure 2.21 presents the same analysis for the commutation of the secondary power switch. It is evident that a capacitance of 420 pF is deemed too large for this particular application, as it can lead to the loss of complete ZVS during commutation. Moreover, if the dead time is excessively long, the equation becomes ineffective due to the possibility of an extra switching event occurring, resulting in the simultaneous occurrence of two dead times. However, this effect is not considered in the current analysis, as it assumes that the dead time is sufficiently small.

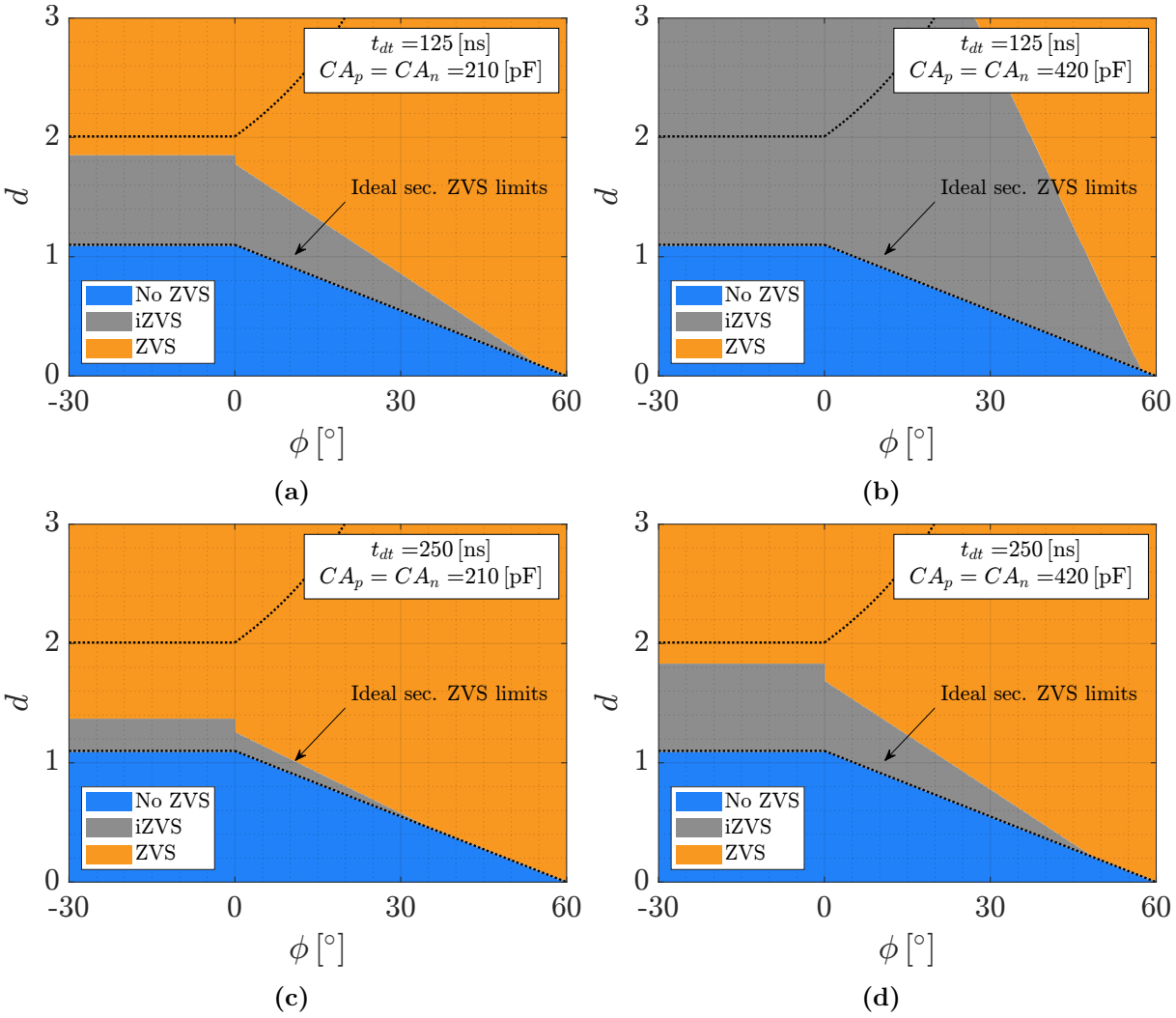

Figure 2.21 – Secondary power switches ZVS, iZVS and no ZVS regions as a function of voltage gain d and angle ϕ with (a) $t_{dt} = 125\,\text{ns}$ and $CA_p = CA_n = 210\,\text{pF}$ (b) $t_{dt} = 125\,\text{ns}$ and $CA_p = CA_n = 420\,\text{pF}$ (c) $t_{dt} = 250\,\text{ns}$ and $CA_p = CA_n = 210\,\text{pF}$ (d) $t_{dt} = 250\,\text{ns}$ and $CA_p = CA_n = 420\,\text{pF}$.

From Figures 2.20 and 2.21, a discontinuity in the transition regions from iZVS to ZVS can be observed in 0 °. This occurs because the calculations assume that dead time occurs separately. However, when the angle is close to multiples of 60 °, meaning that the switching of the primary and secondary happens closely, the capacitor discharge effect takes place simultaneously, altering the discharge pattern of the capacitors. This effect is not accounted for in the calculations.

2.5 CONCLUSION

This chapter introduced the DAB3 converter along with various modulation techniques, with a focus on the PS modulation. The three-phase transformer model was then described, treating it as three individual single-phase transformers. Additionally, six arrangement options between the three-phase transformer and the inductors were presented: YY, YD, oDY, oDD, iDY, iDD, referred as 3ϕ networks.

Next, a methodology was presented for formulating equations related to converter stress. The oDY transformer was chosen as an illustrative example. Most of these equations can be found in Appendix A for the six 3ϕ network, and a few ones were omitted due to their size. Throughout this chapter, results were depicted using graphs. An analysis was then conducted to describe various aspects, including output power, current distribution in the power switches, the influence of mutual inductance, and the ripple in the DC bus voltage. To verify the accuracy of these equations, simulations were carried out, and specific parameters were compared to demonstrate the formulation precision.

The chapter also included an analysis of the converter switching behavior. Since the DAB3 could achieve ZVS in certain operating regions, a detailed investigation was conducted to understand if this was possible. The analysis focused on the voltage across the power switches, considering the impact of the parasitic capacitor in parallel. During the switching instant, which occurred within the dead time, a new state was introduced to represent the voltage across the parasitic capacitor. Differential equations were used to examine how this capacitor discharged, and six different operating points were used to illustrate the discharge process.

Depending on the dead time, the switching process might or might not have achieved ZVS, leading to either iZVS or no ZVS operation. To help understand the converter behavior under different conditions of parasitic capacitance and dead time, a comprehensive flowchart was provided. This flowchart helped determine the converter operating mode, whether it was in ZVS, iZVS, or no ZVS mode.

Chapter

3 Reconfigurable Transformer Connection Strategy

In this chapter, the Reconfigurable Transformer Connection Strategy (RTCS) is introduced, which involves distinct 3ϕ networks utilization that were presented in Chapter 2. The main objective is to investigate the potential benefits of combining these different 3ϕ networks to expand the ZVS regions and, consequently, enhance the converter efficiency. The iDY and YY 3ϕ networks are selected to verify this enhancement, and the theoretical versus experimental efficiency is presented at various operating points. The analysis includes the investigation of different sources of losses and their respective predominant regions.

3.1 RTCS CONCEPT

PS modulation offers inherent advantages such as easy implementation and built-in ZVS capability, without the need for auxiliary components. Nonetheless, the efficiency of power conversion and the ZVS range of this modulation method decline when the voltage conversion ratio deviates from unity [23].

Previous research enhancing converter efficiency through transformer switching are presented in [36, 37]. These studies focus on altering the DAB transformer turns ratio using relays or semiconductors, and operate within a high-efficiency region.

The Reconfigurable Transformer Connection Strategy is introduced as another option to mitigate the issue of low efficiency when voltage conversion ratio deviates from unity. This strategy employs three relays to enable the three-phase transformer connection reconfiguration. Figure 3.1 (a) and (b) depict the YY and oDY 3ϕ networks, respectively. Figure 3.1 (c) demonstrates the use of relays to switch between the YY and oDY connections. When the relays are in the NC position, a YY connection is established, while switching to the NO position results in an iDY connection.

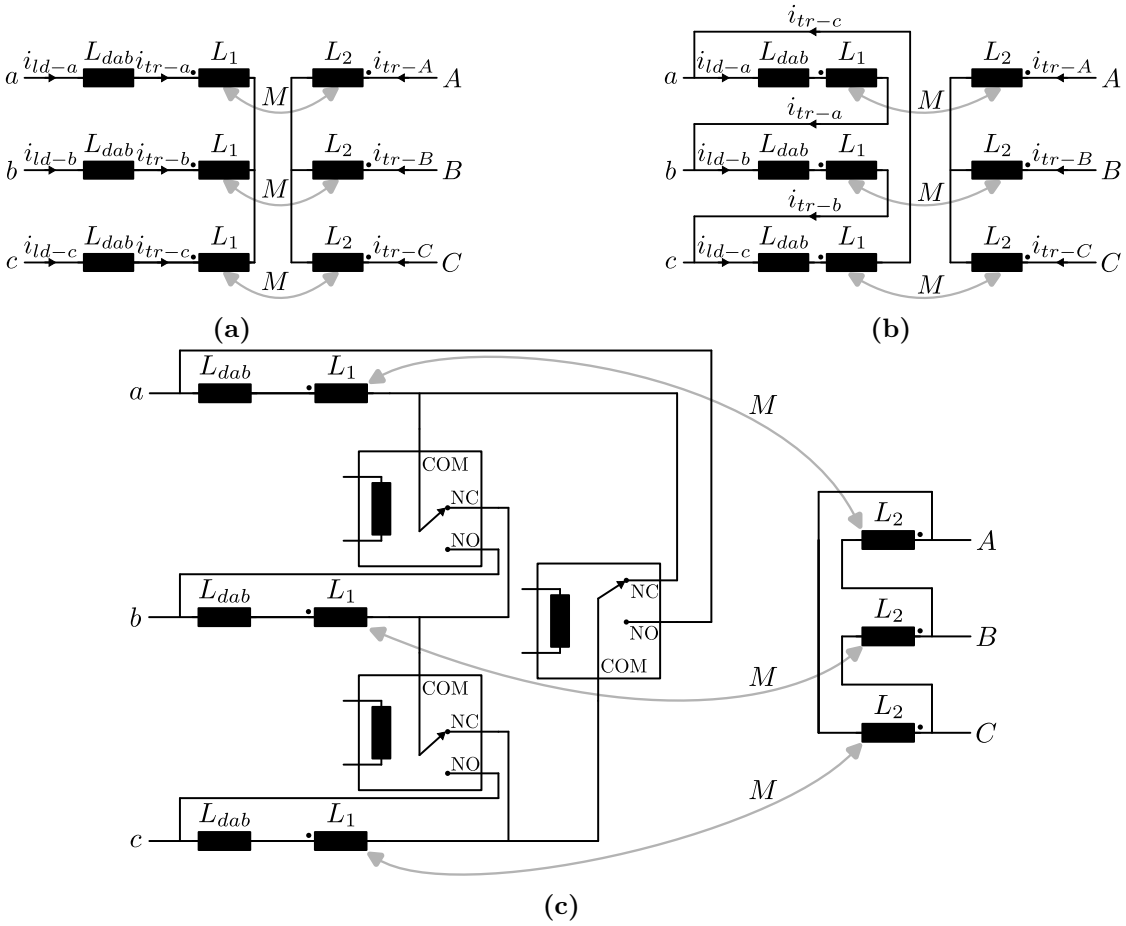

Figure 3.1 – Options of 3ϕ network: (a) YY, (b) iDY, (c) An example of using relays to switch between the YY and iDY 3ϕ network.

This flexibility enables the exploration of different combinations of 3ϕ networks to find the optimal design that operates efficiently across a wide range of conditions. Figure 3.2 presents different arrangements where one side of the transformer remains fixed while the other side is varied. For each arrangement, the values of n and L_{dab} are adjusted to cover the widest operating region within a load range of 200 V to 400 V and a maximum current of 10 A.

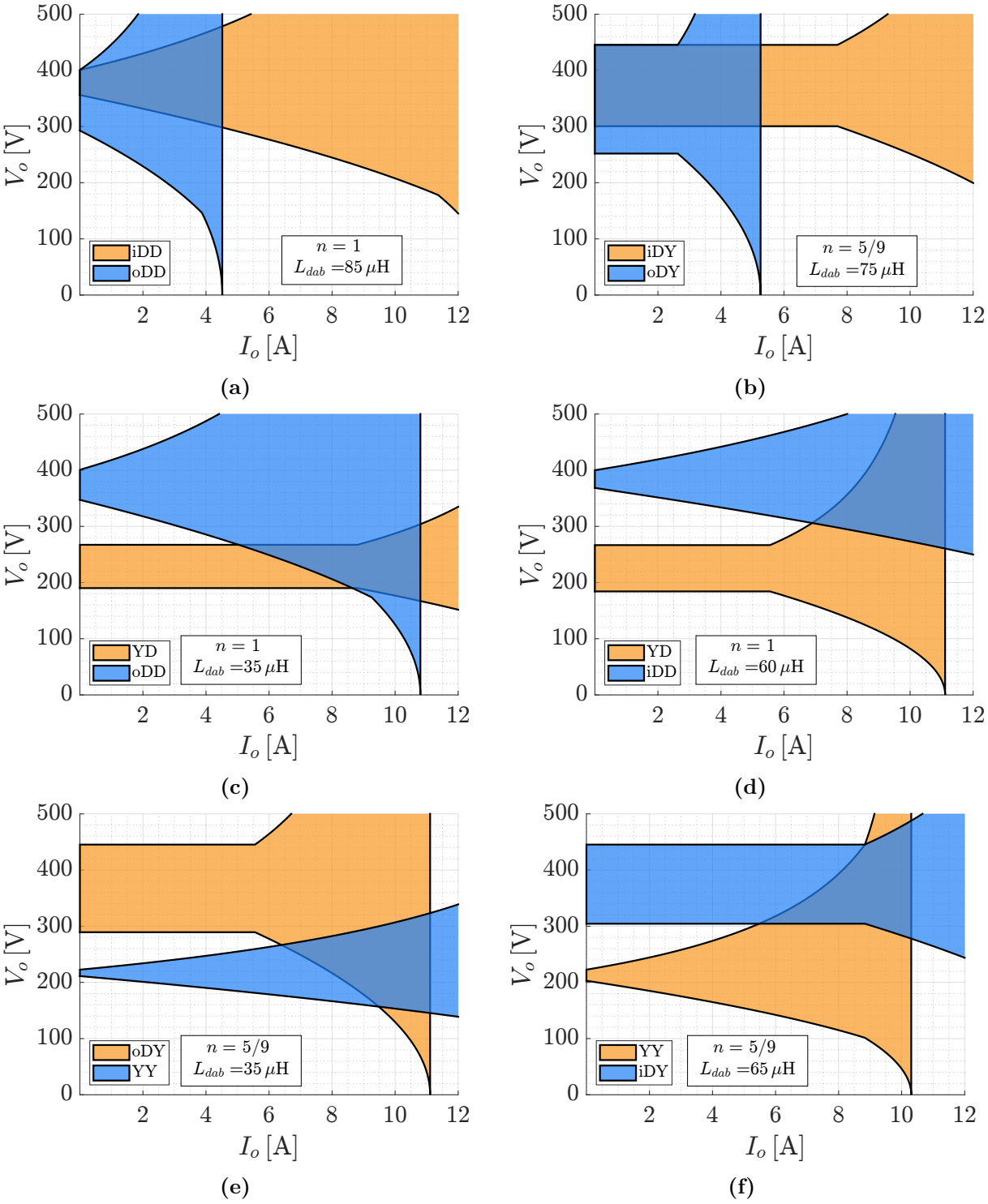

Figure 3.2 – The ZVS range for the arrangements (a) iDD and oDD (b) iDY and oDY (c) YD and oDD (d) YD and iDD (e) oDY and YY(f) YY and iDY

Furthermore, Figure 3.3 introduces an alternative configuration in which the primary side of the transformer is varied among three options, while the secondary side remains fixed. The ZVS power range for each arrangement is depicted in the respective figures, and specific values of n and L_{dab} for each option are provided. However, this particular configuration is not further analyzed in this study.

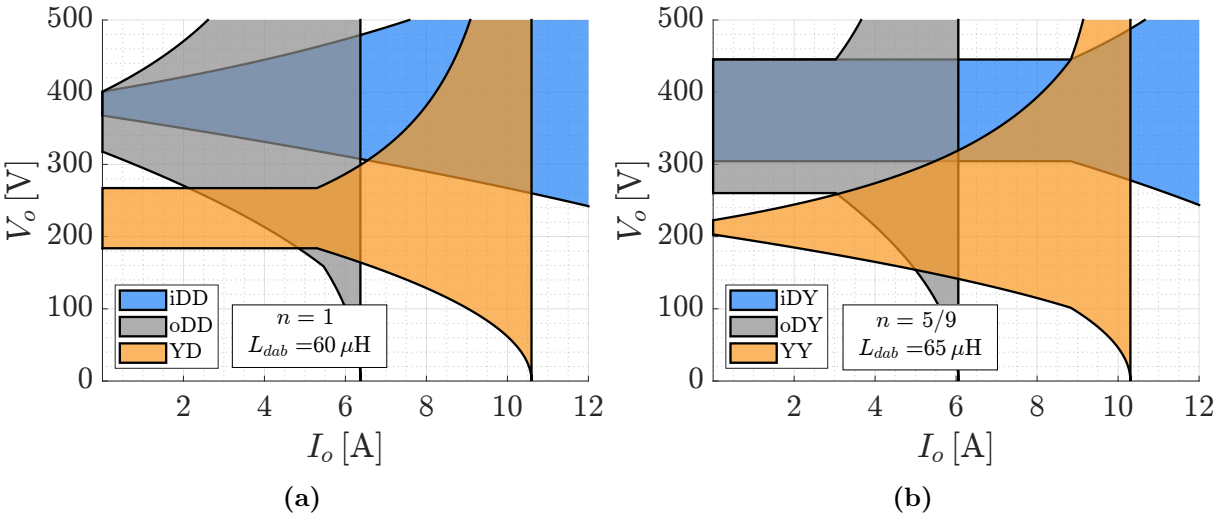

Figure 3.3 – The ZVS power range for the arrangements (a) iDD, oDD and YD ($n = 1.05$ and $L_{dab} = 90\,\mu$F) (b) iDY, oDY and YY ($n = 5/9$ and $L_{dab} = 90\,\mu$F)

3.2 RTCS APPLICATIONS

In Chapter 1, several applications of the IBDC are presented, and among them, the DAB3 can be a potential topology to be utilized. However, the RTCS has some drawbacks that limits its applications. Due to the need to switch an inductive element, the 3ϕ network, this strategy requires an interruption of the power transfer from the converter to the load. As a result, its application is restricted to loads that can tolerate such momentary interruptions. Hence, this strategy can be advantageous for applications where there are significant variations in the output and/or input voltage, and the load can handle momentary power transfer interruptions.

3.2.1 Fast DC charger

The EV charging system presented in Figure 1.2 comprises a fast DC charger with capability to charge multiple types of batteries. Figure 3.4 illustrates the typical operating output range voltage/current for general-purpose EV charger. Dots are placed on the graph representing the batteries listed in Table 1.1 according to their operating voltage and maximum charging current to demonstrate the voltage variation.

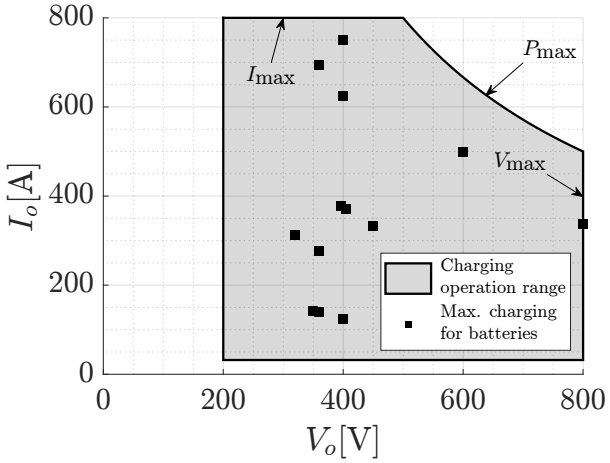

Figure 3.4 – Operating region of the charger along with dots (■) indicating the points of maximum charging power for commercial batteries.

The battery voltage can vary between 320 V and 800 V. Due to this wide voltage variation, the implementation of the RTCS can be advantageous. This strategy enables the charger to promptly identify the battery voltage level upon connection and switch the appropriate 3ϕ network to maximize the charging efficiency.

3.2.2 On-boarder chargers

Another potential application is for on-board chargers. The charger can be designed in a single-stage or two-stage configuration, with a representation of the two-stage configuration shown in Figure 3.5. The two-stage setup comprises a PFC rectifier and a DC-DC converter responsible for power flow control to the battery. It is common for the rectifier to maintain a fixed DC bus voltage for the DC-DC converter.

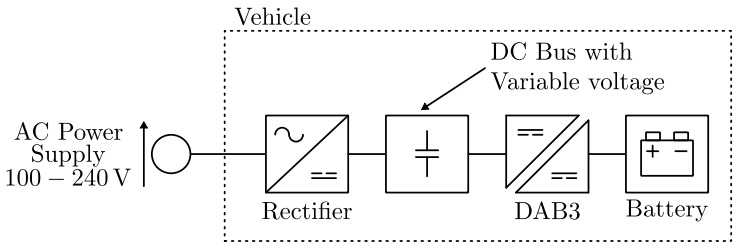

Figure 3.5 – An universal on-board battery charger with DC bus with variable voltage.

However, these chargers must be universal and capable of handling a wide input voltage variations, ranging from 100 V to 240 V. Maintaining a constant voltage for such a wide input range can be problematic. Nevertheless, if the bus voltage can be adjusted to two different levels, one for 100 V and other for 240 V, it could simplify the rectifier design. Assuming that the DC bus can be set to two possible voltage levels, the RTCS becomes an interesting option, as each 3ϕ network can be designed for one voltage level.

3.3 EXPERIMENTAL RESULTS

Experimental tests are conducted using the YY and iDY 3ϕ networks with the parameters specified in Table 3.1 to access the potential advantage of transformer connection variation.

Table 3.1 – DAB3 prototype parameters.

Parameters	Value	Parameters	Value
V_i	400 V	L_{dab}	61.6 μH
V_o	200 – 400 V	L_{tr1}	1.4 μH
I_o	0 – 10 A	L_{tr2}	0.4 μH
f_s	100 kHz	L_m	0.7 mH
n	5/9	t_{dt}	170 ns
$P_{\max}$	4 kW		

The converter design methodology is detailed in Appendix B. An overview of the main materials used in the prototype is provided in Table 3.2.

Table 3.2 – Material list.

	Function	Description	Code
s_{a-c} and s_{A-C}	Power switches	SIC MOSFET 1200V/36A	C2M0080120D
L_{dab}	Serie inductor	Inductor 61.6 μH	2x E55/28/25-N87
Transformer	Transformer	Three-phase transformer $n = 5/9$	4x E71/33/32-3C94
C_p and C_s	Bus capacitor	Capacitor 800 V 40 μF	MHBS455400 800VDC
$C_{DC-\text{block}}$	Serie capacitor	Capacitor 220 V 5.6 μF	75MW4560

Figure 3.6 depicts the prototype. The image showcases the command and buffer board responsible for PWM, along with two three-phase inverters, one for the primary side and another for the secondary side. The relay board is also shown, responsible for online switching the transformer connection. This board comprises nine relays, which are adequate to access all 3ϕ networks illustrated in Figure 2.5 (b-g). However, these relay boards are not utilized in the subsequent results. An online connection switch remains a topic for future analysis.

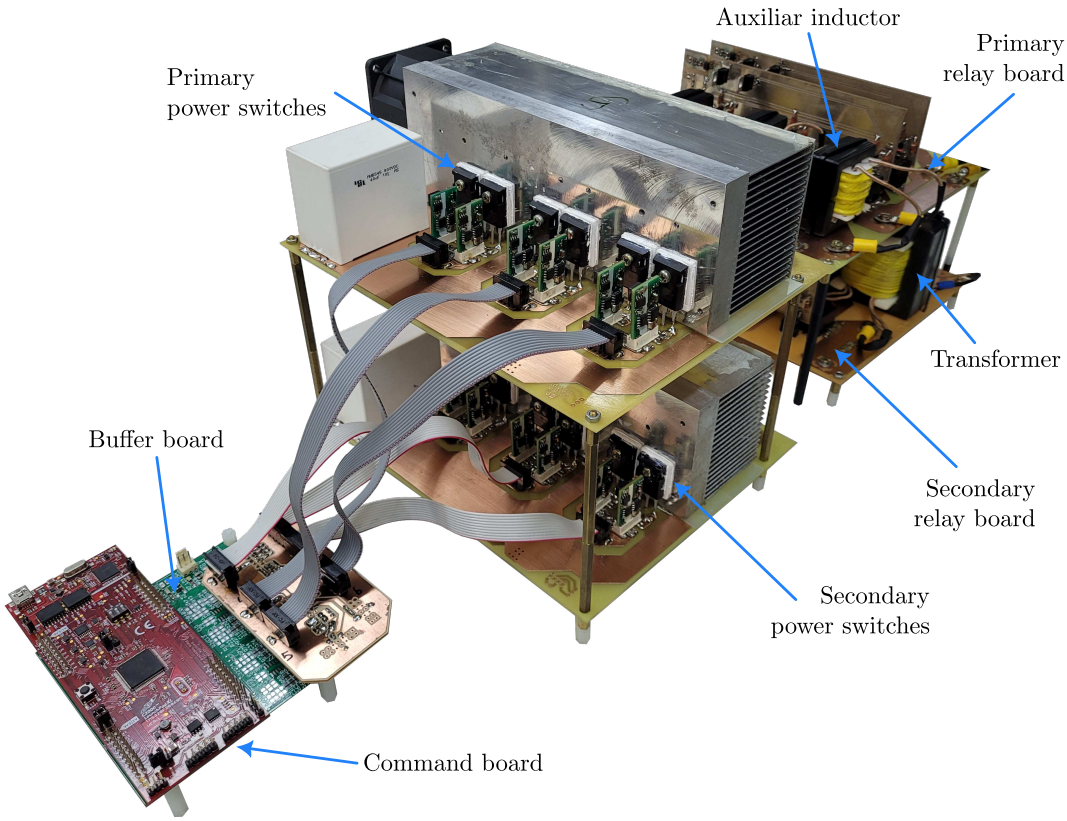

Figure 3.6 – Prototype.

3.3.1 Test Setup

To perform fixed input and output voltage tests on the converter, two voltage sources (v_{in} and v_{out}) and a bank of resistors (R_L) are utilized. The test setup schematic in Figure 3.7 illustrates the configuration.

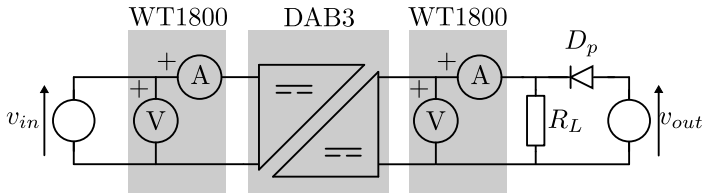

Figure 3.7 – Test setup schematic.

The voltage source connected to the converter output ensures a constant voltage across the resistor bank. As the DAB3 converter supplies more current, the voltage source needs to provide less current to maintain the clamped voltage. In the schematic, the position of the wattmeter is also indicated. DAB3 converter input and output power are measured using a wattmeter, enabling the calculation of the converter efficiency.

For safeguarding the output voltage, a diode named D_p is employed since both voltage sources are unidirectional. If the current supplied by the DAB3 converter is significant and causes the voltage across the resistor to exceed the clamped value, diode D_p stops conducting, preventing that current enters into the output power supply.

The equipment used for the experiments includes:

- Wattmeter: WT1800 High Performance Power Analyzer
- Voltage source: TS500-40 Programmable DC Power Supply (500 Vdc and 40 Adc)
- Voltage source: TopCon DC power supply (600 Vdc and 20 Adc)
- Osciloscope: WaveSurfer 3024z 200 MHz

The test setup can be observed in Figure 3.8.

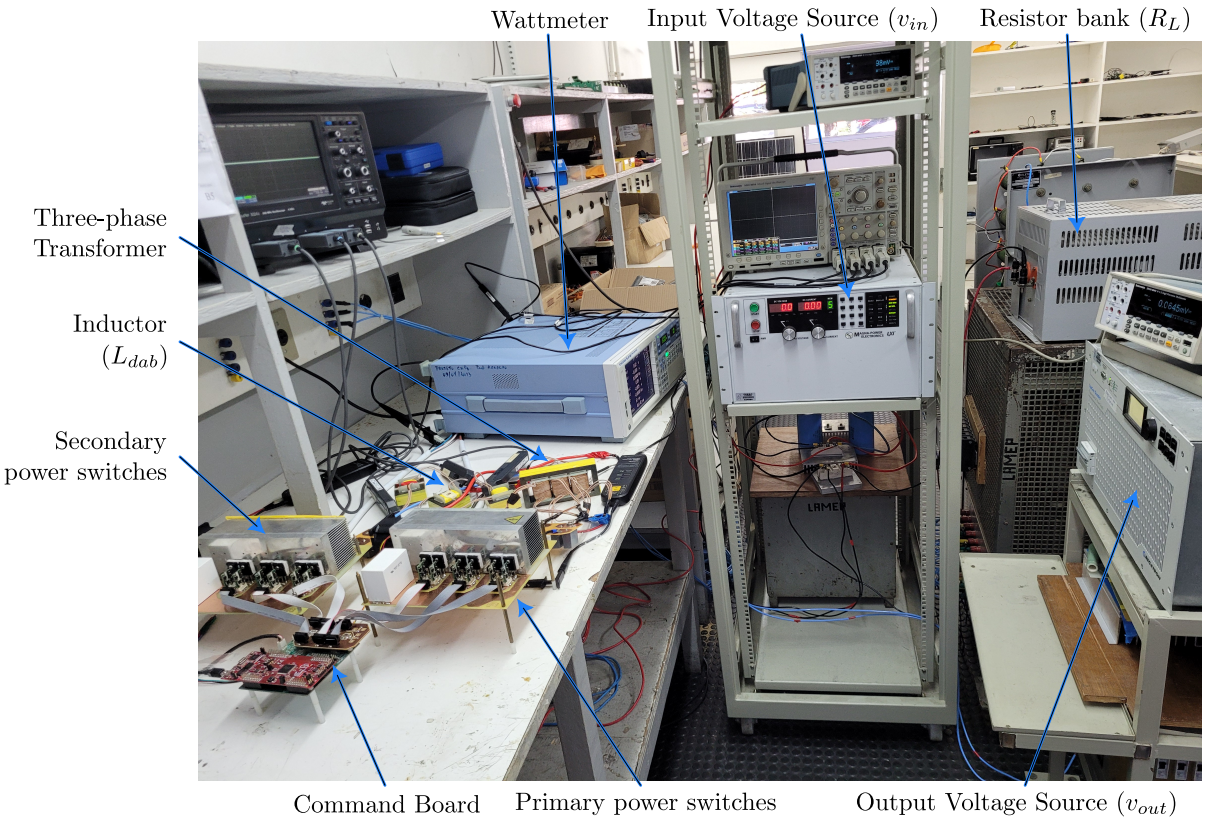

Figure 3.8 – Test setup

3.3.2 Converter operation

This section show the converter operation. Figure 3.9 presents the ideal ZVS regions for both transformers. The iDY transformer achieves ZVS at a higher voltage, around 400 V, while the YY transformer reaches ZVS at a lower voltage, approximately 200 V, resulting in higher efficiency for each configuration in its respective ZVS region.

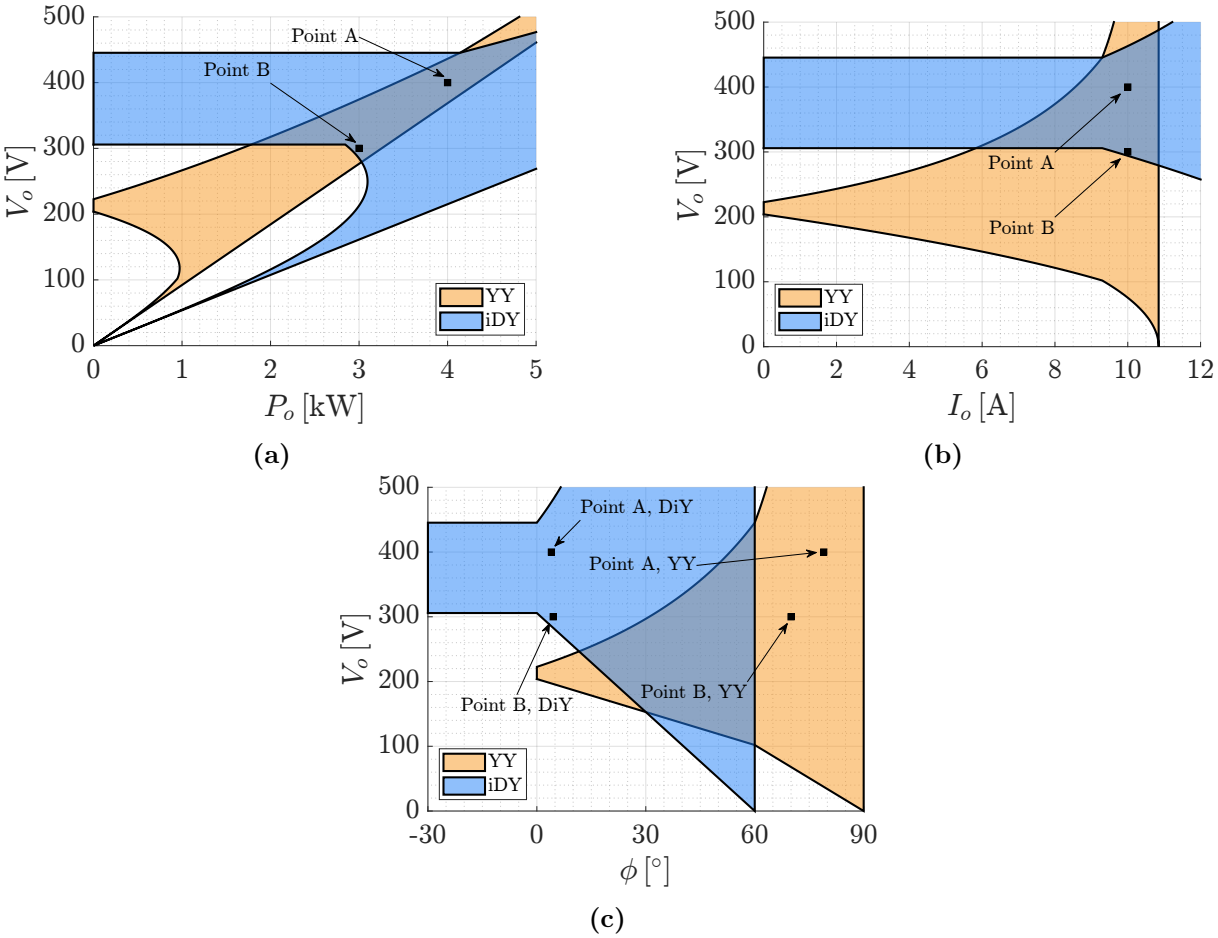

Figure 3.9 – ZVS regions for transformers YY and iDY as a function of the output voltage with (a) output power, (b) output current or (c) angle

Two operational points, denoted A and B, are tested for each 3ϕ network to verify the proper operation of the converter. These points are illustrated in Figure 3.9 and summarized in Table 3.3. The DAB3 converter exhibits the characteristic that the output current does not depend on the load but rather on the angle. However, for points A and B, it is necessary to adjust the practical angle to maintain the output current at 10 A, due to differences in efficiency.

Table 3.3 – Parameters for presented inductor currents waveforms.

Points	V_o [V]	P_o [kW]	Angle ϕ [°]	Efficiency η [%]
iDY: A	400	4	4	97.3
iDY: B	300	3	3.5	96.7
YY: A	400	4	75	94.3
YY: B	300	3	70	95.4

The inductor currents in the three phases, obtained from both theoretical equations and experimental tests, are depicted in Figure 3.10.

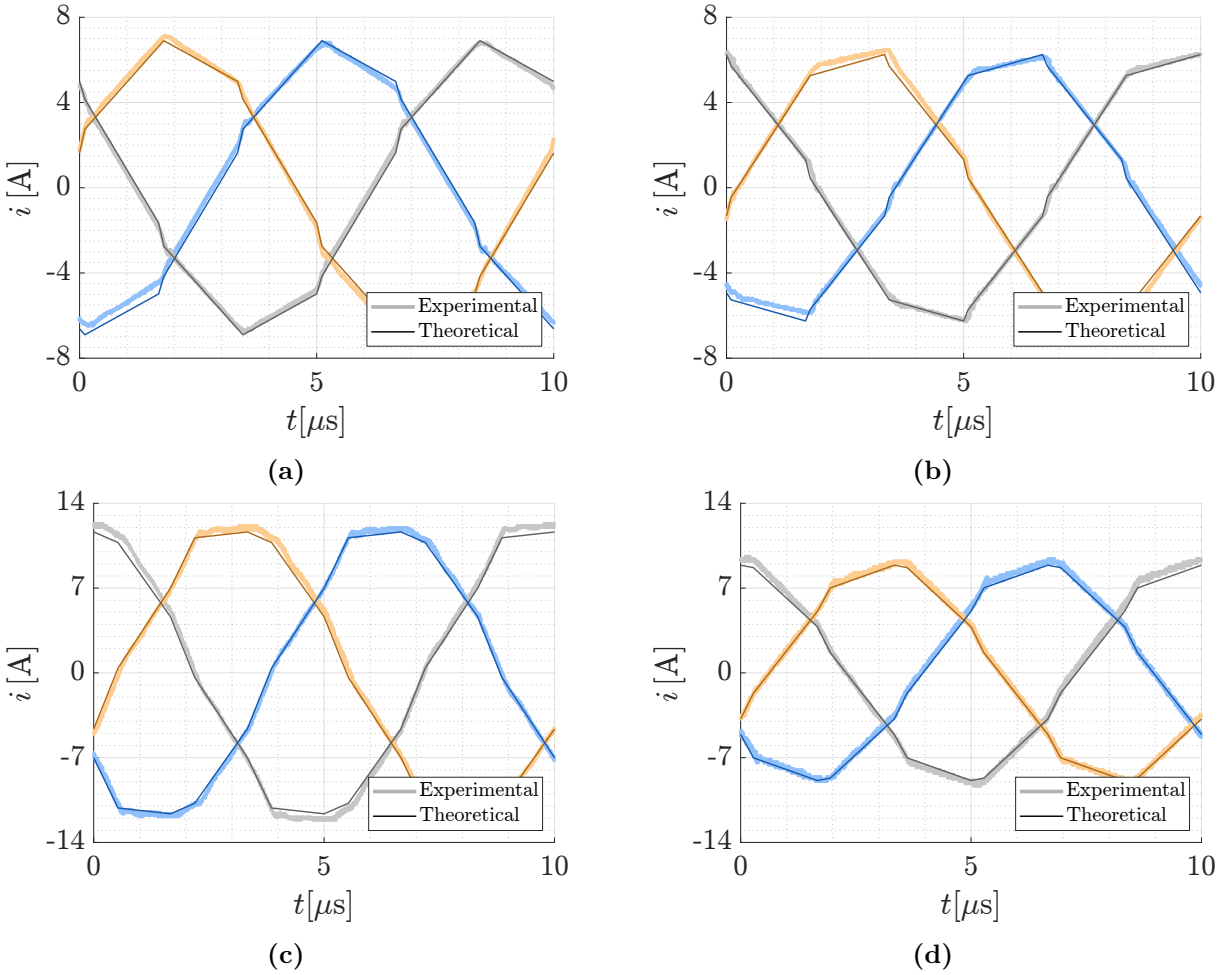

Figure 3.10 – The three phase inductor (L_{dab}) currents for iDY (a) point A (b) point B and for YY (c) point A (d) point B

The converter efficiency is influenced by the operation mode, whether it is SS or HS. Figure 3.11 provides a visual representation of the ZVS, iZVS, and no ZVS regions for each power switch (primary and secondary) and each 3ϕ network.

Figure 3.11 (a-b) illustrates the ZVS regions for the YY transformer. In the first graph, it can be observed that the primary power switch exhibits a wide ZVS region, while the second graph shows that the secondary power switch has a smaller ZVS region. This difference is due to the current in the secondary power switch having a derivative that leads to a more negative current, which facilitates the switching process. On the other hand, this behavior does not occur for the primary switches, as the current tends to be positive, requiring a more negative initial current to enter the ZVS region.

Figure 3.11 (c-d) show the ZVS regions for the iDY transformer. In this case, both the primary and secondary power switches have considerable iZVS regions. It is also noteworthy that the region in the iDY configuration mainly depends on the voltage level and is less affected by the current level.

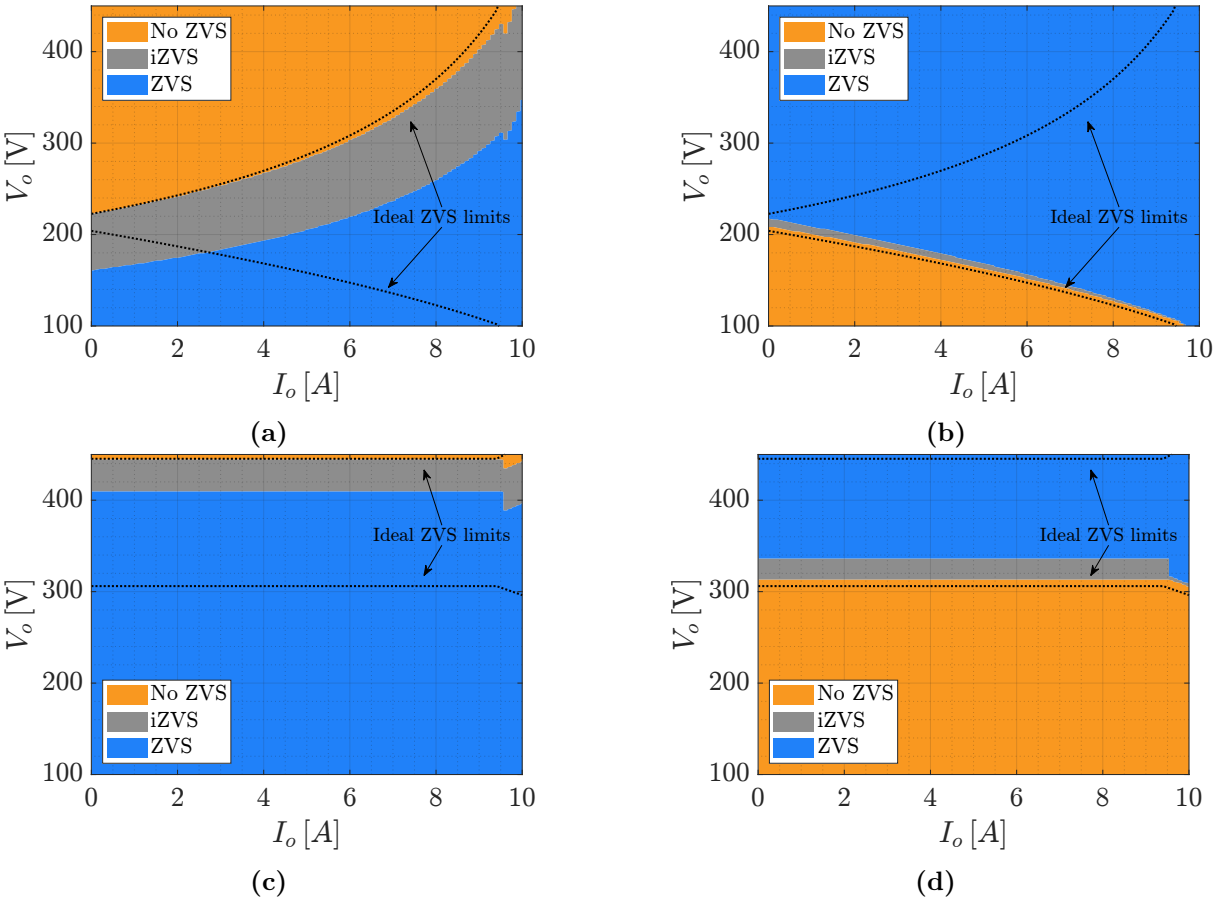

Figure 3.11 – ZVS, iZVS, and no ZVS regions as a function of voltage gain d and output current I_o for (a) secondary power switch and YY transformer (b) primary power switch and YY transformer (c) secondary power switch and iDY transformer (d) primary power switch and iDY transformer

3.3.3 Converter efficiency

The main objective here is to demonstrate the potential efficiency improvement achieved through the RTCS. Multiple efficiency curves are presented to validate its effectiveness, and the methodology for calculating losses is detailed in Appendix C. To ensure accurate efficiency measurement, the converter operates for 30 minutes before recording the efficiency at each operating point, allowing it to reach a steady-state temperature regime. The converter efficiency is presented in Figure 3.12 for point A with both the iDY and YY 3ϕ network.

Additionally, Figure 3.13 displays the estimated individual loss components and the corresponding measured total loss from the prototype for operating points A and B of the 3ϕ network. The percentage errors are also presented, ranging from 10 % to 22 %. The iDY transformer exhibits lower error percentages since it operates within the ZVS region for the given operating points, whereas the YY transformer shows higher errors due to operating outside the ZVS region. Despite the considerable percentage error in the loss calculations, the theoretical predictions effectively capture the overall loss behavior.

Figure 3.14 (a-e) show the efficiency of the converter for different output voltage

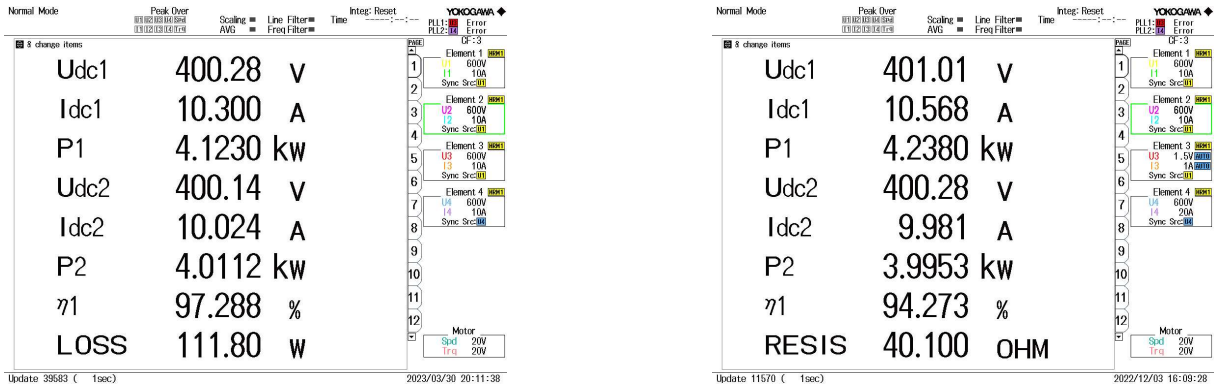

(a) **(b)**

Figure 3.12 – Converter efficiency measured with a wattmeter for point A with (a) iDY 3ϕ network and (b) YY 3ϕ network.

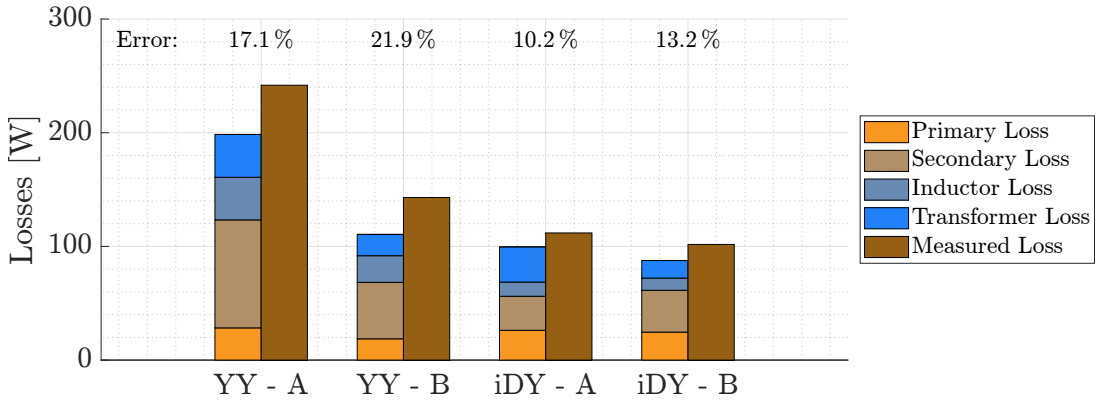

Figure 3.13 – Measured and calculated loss for DAB3 for the operation points A and B

values. The continuous lines represent the theoretical efficiency, while the square dots (■) indicate the measured efficiency. Figure 3.14 (f) shows the experimental points along with the ideal ZVS regions.

Figure 3.15 (a) and (b) display the theoretical efficiency of both transformers as a function of output voltage (V_o) and output current (I_o). The results reveal two optimal operating points: the iDY transformer demonstrates best performance within the voltage range of approximately 300 V to 400 V, while the YY transformer exhibits optimal efficiency at a lower voltage range, specifically around 200 V to 250 V.

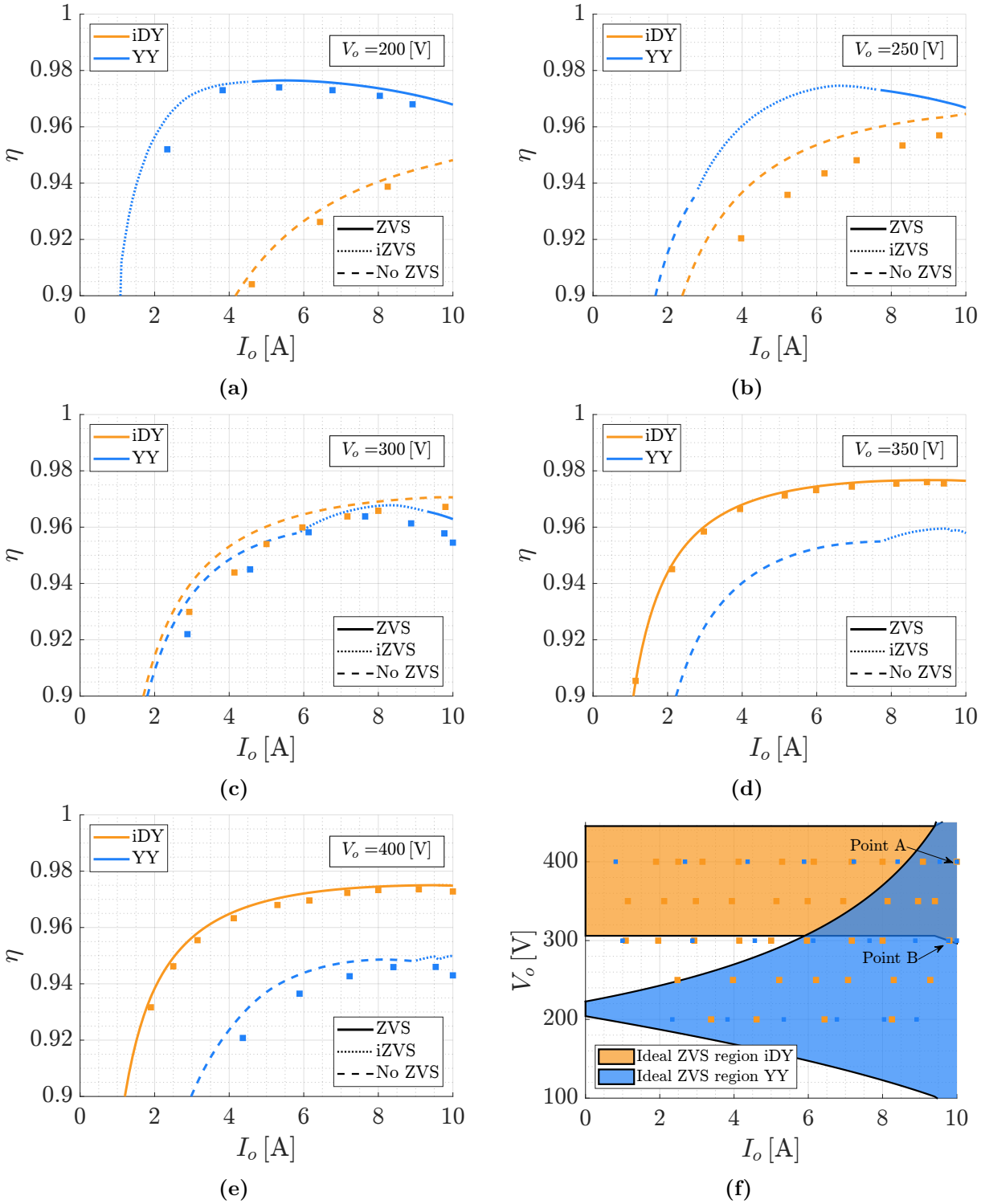

Figure 3.14 – Theoretical (——) and experimental (■) efficient of DAB3 for different V_o as a function of I_o (a) $V_o = 200$ [V] (b) $V_o = 250$ [V] (c) $V_o = 300$ [V] (d) $V_o = 350$ [V] (e) $V_o = 400$ [V] (f) Ideal ZVS regions and the experimental points (■) of both 3ϕ network

Considering the scenario where one 3ϕ network operates with a voltage below 300 V and the other with a voltage above 300 V, Figure 3.15 (c) depicts the theoretical efficiency of this merged system. Notably, the efficiency of this configuration exceeds 95% for almost the entire operating region, with the exception of currents below 4 A, where the efficiency

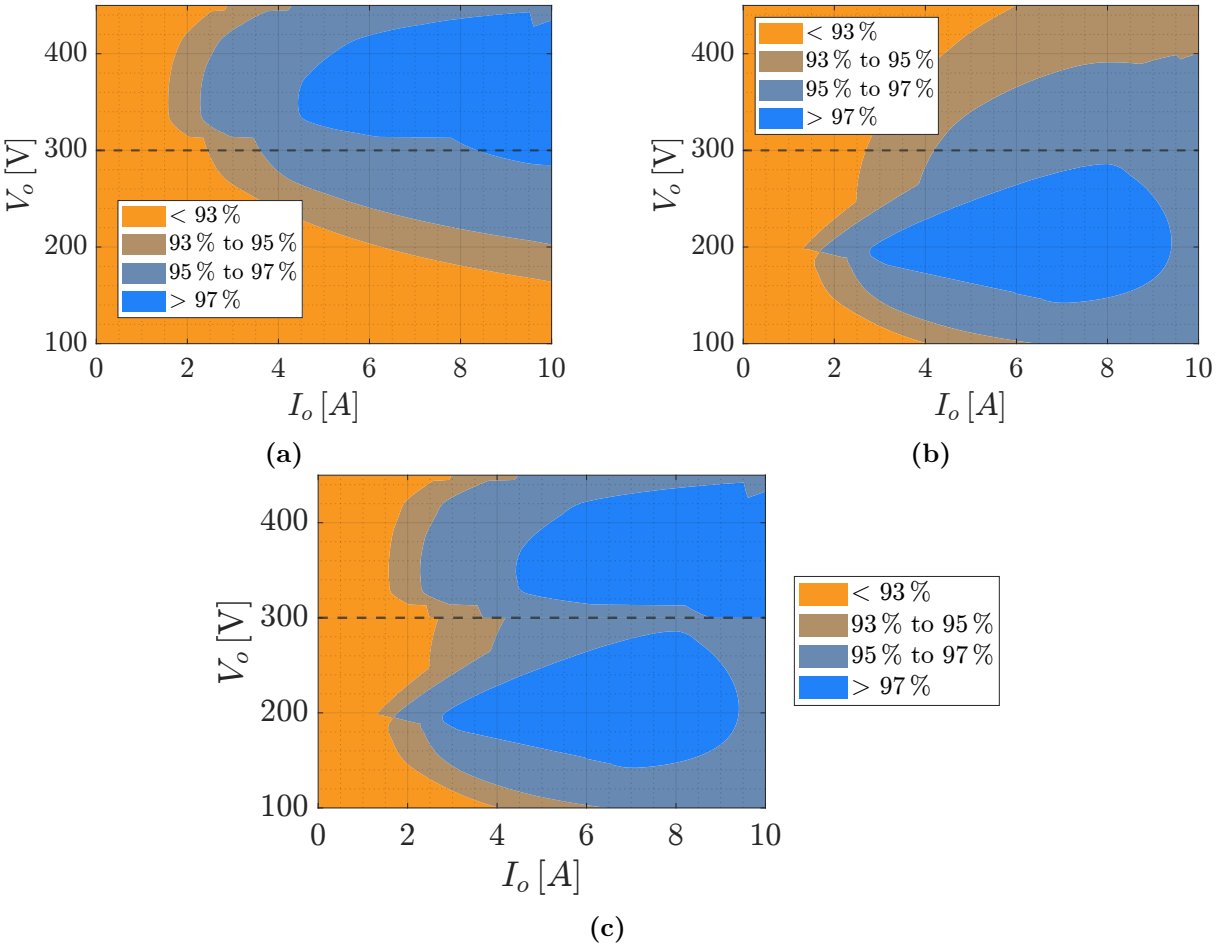

Figure 3.15 – Converter theoretical efficiency as function of V_o and I_o for the transformers (a) iDY (b) YY (c) Merged iDY with YY assuming a division in 300 V

experiences a reduction.

Once it is considered that the loss model is close enough to the practice, the following is an analysis of the theoretical main source losses. The considered loss components are: switching loss for both primary and secondary power switches, conduction loss for both primary and secondary power switches, coil loss from both inductor and transformer, and core loss for both inductor and transformer.

Figure 3.16 illustrates the reduction in converter efficiency due to switching losses. In the ideal ZVS region, the converter demonstrates high efficiency; however, as it approaches the transition edge, it enters the iZVS region. In this region, the converter operates with partial ZVS, experiencing losses during both turn-on and turn-off transitions. Furthermore, when it goes out of the ZVS region, it enters the no ZVS region, where there are losses during turn-on. As a result, this region exhibits the highest losses.

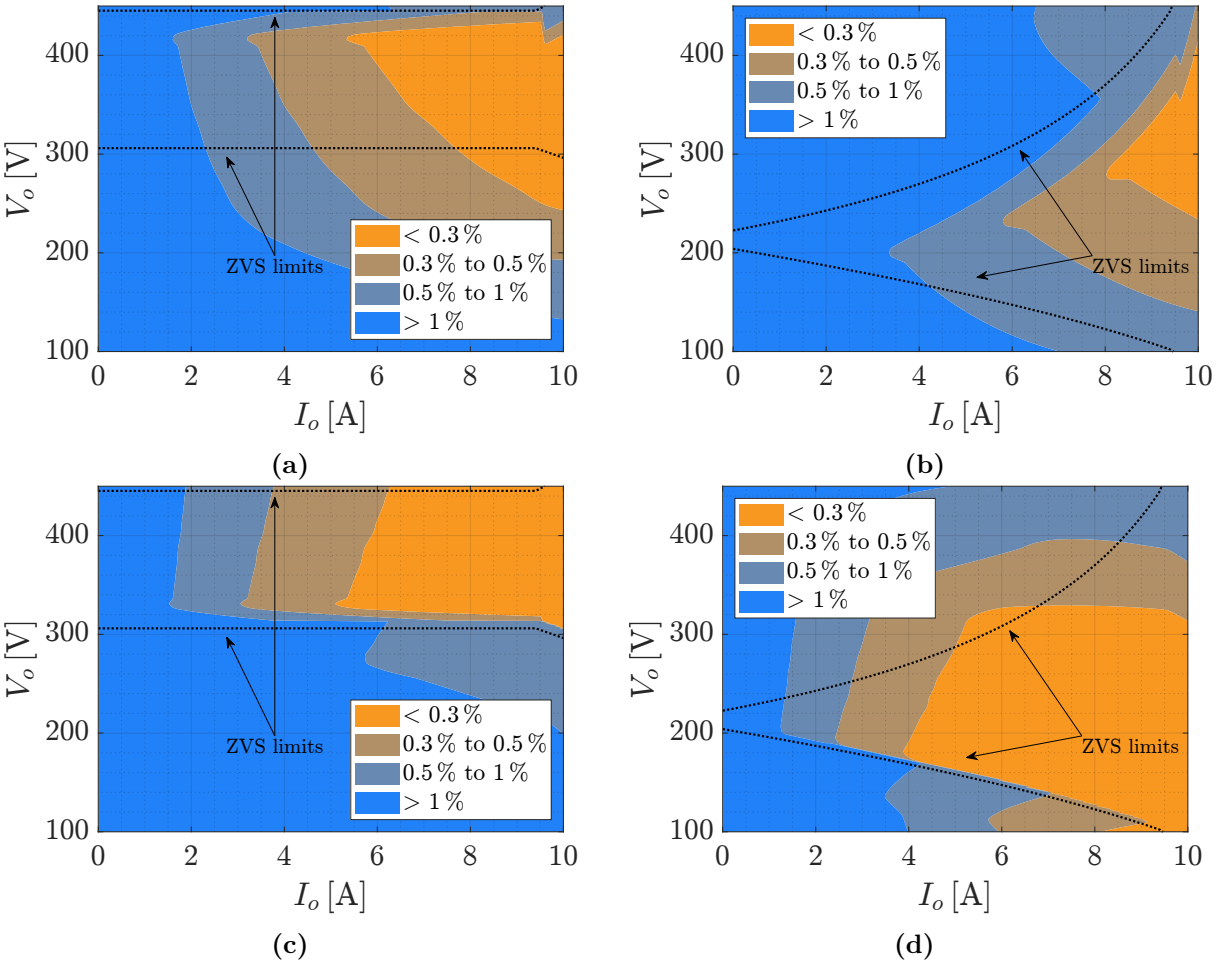

Figure 3.16 – Reduction in converter efficiency due to switching losses for (a) primary power switches with iDY transformer, (b) primary power switches with YY transformer, (c) secondary power switches with iDY transformer, and (d) secondary power switches with YY transformer

In Figure 3.17, the graph illustrates the reduction in converter efficiency due to conduction losses. These losses are dependent on the RMS current passing through the power switch. It is evident that both transformers have different optimal operating points, which are close to the ideal ZVS region. This is particularly true for the iDY transformer, where a significant portion of the region with a reduction in efficiency less than 0.4 % falls within the ZVS region. Therefore, this is a loss that is also reduced when operating within the ZVS region, as the RMS current naturally decreases in relation to the power processed by the converter.

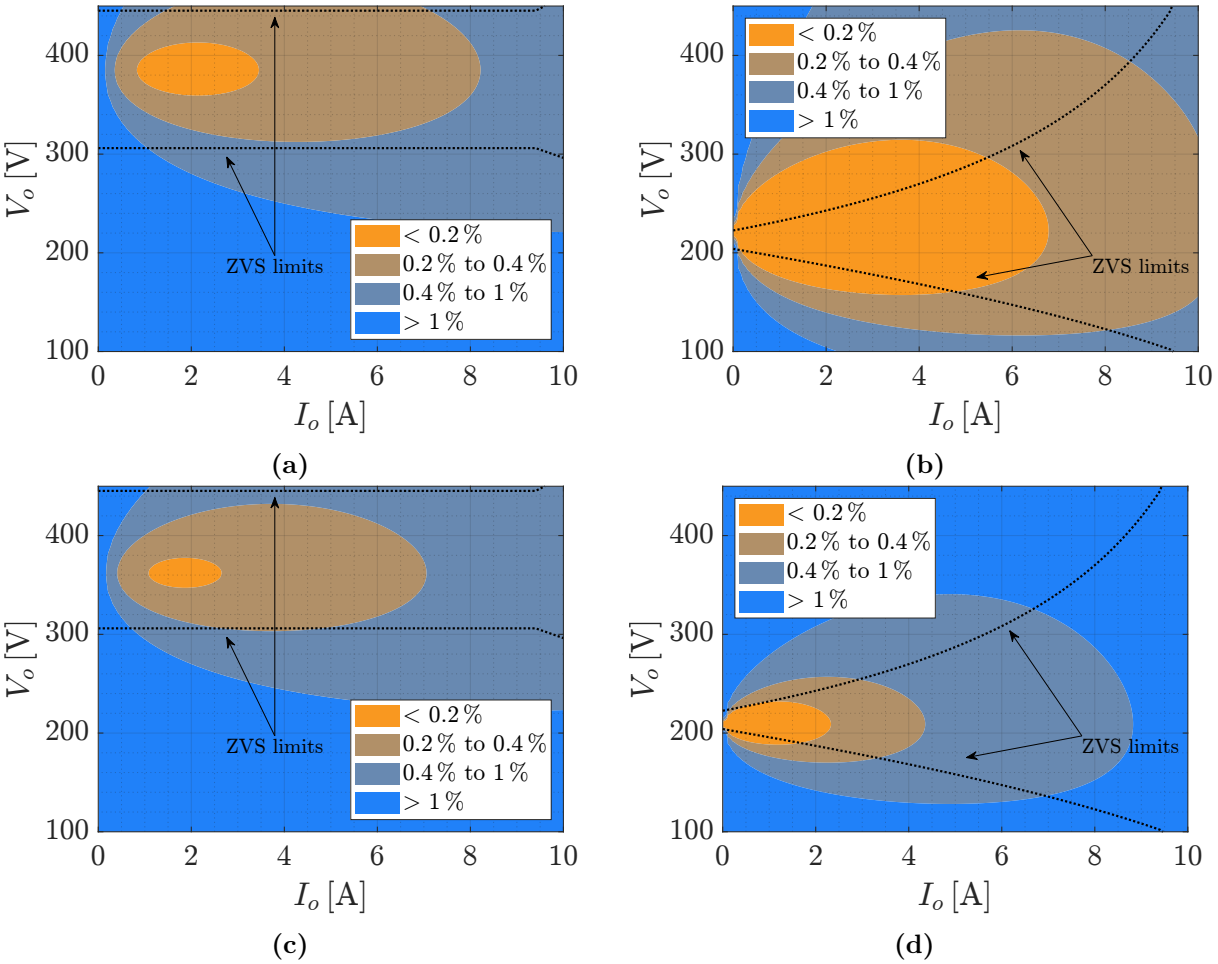

Figure 3.17 – Reduction in converter efficiency due conduction loss for (a) primary power switches with iDY transformer (b) primary power switches with YY transformer (c) secondary power switches with iDY transformer (d) secondary power switches with YY transformer

Figure 3.18 illustrates the decrease in converter efficiency due to coil losses. These losses are determined by the RMS current at each frequency, obtained through Fourier series analysis, along with the equivalent resistance at that frequency, calculated using Dowell equations. The analysis includes losses up to the 20th harmonic. Similar to conduction losses, coil losses are another source of loss that naturally reduces when the system operates within the ZVS region. This conclusion is valid for both the inductor coil losses and the transformer coil losses.

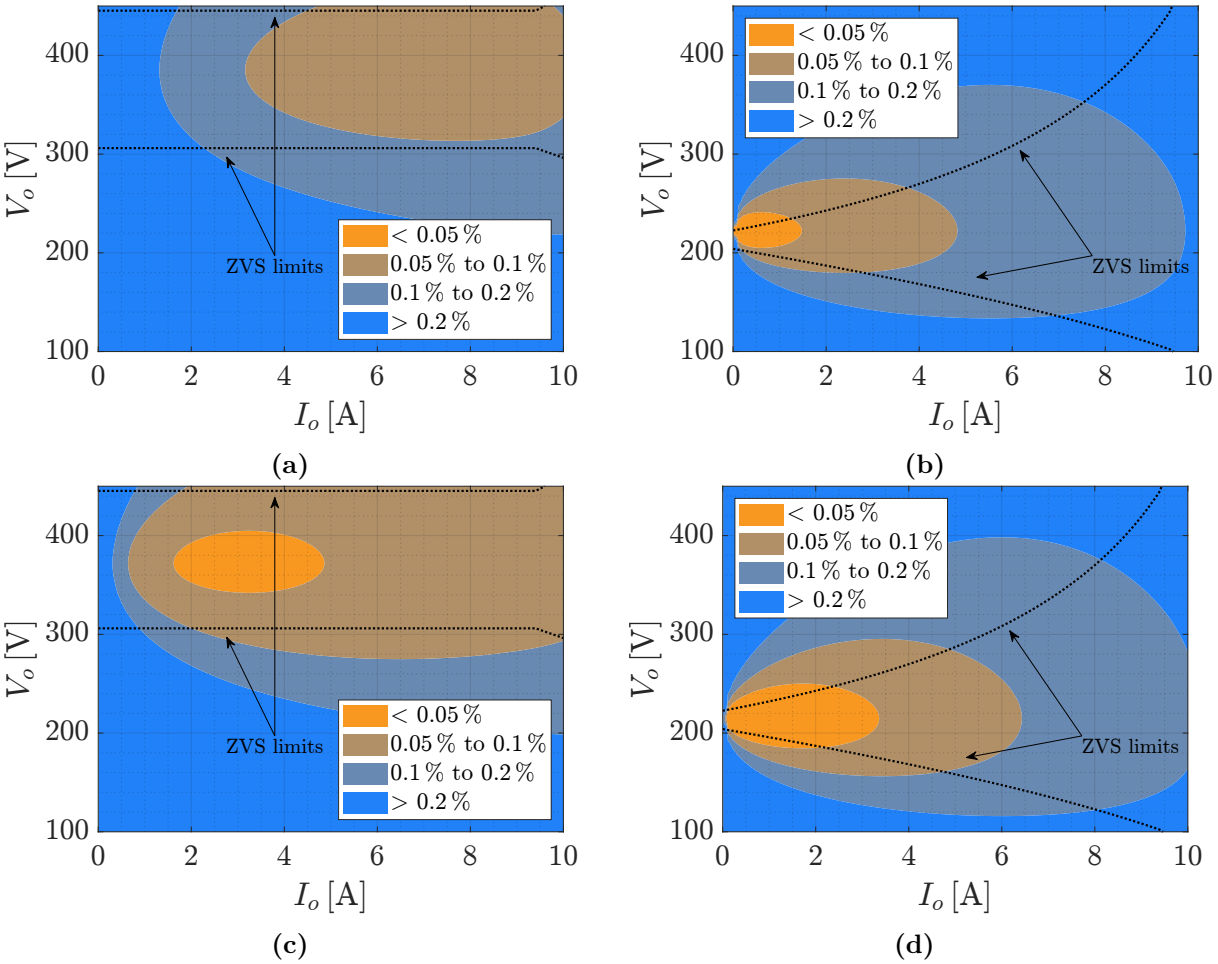

Figure 3.18 – Reduction in converter efficiency due coil loss for (a) inductor with iDY transformer (b) inductor with YY transformer (c) transformer with iDY transformer (d) transformer with YY transformer

Figure 3.19 (a) and (b) depicts the reduction in converter efficiency due to inductor core. These losses are dependent on the magnetic flux applied to the inductor, which is influenced by the operating point. It can be observed that the ZVS region offers the most favorable conditions for reducing core losses in the inductor for both 3ϕ network. On the other hand, Figures 3.19 (c) and (d) present the reduction in converter efficiency due to transformer core. These losses are determined by the voltage applied to the secondary side of the transformer and, theoretically, are independent of the current level that the converter must handle. Since both transformers have a star connection on the secondary side, they exhibit the same loss for the same voltage level.

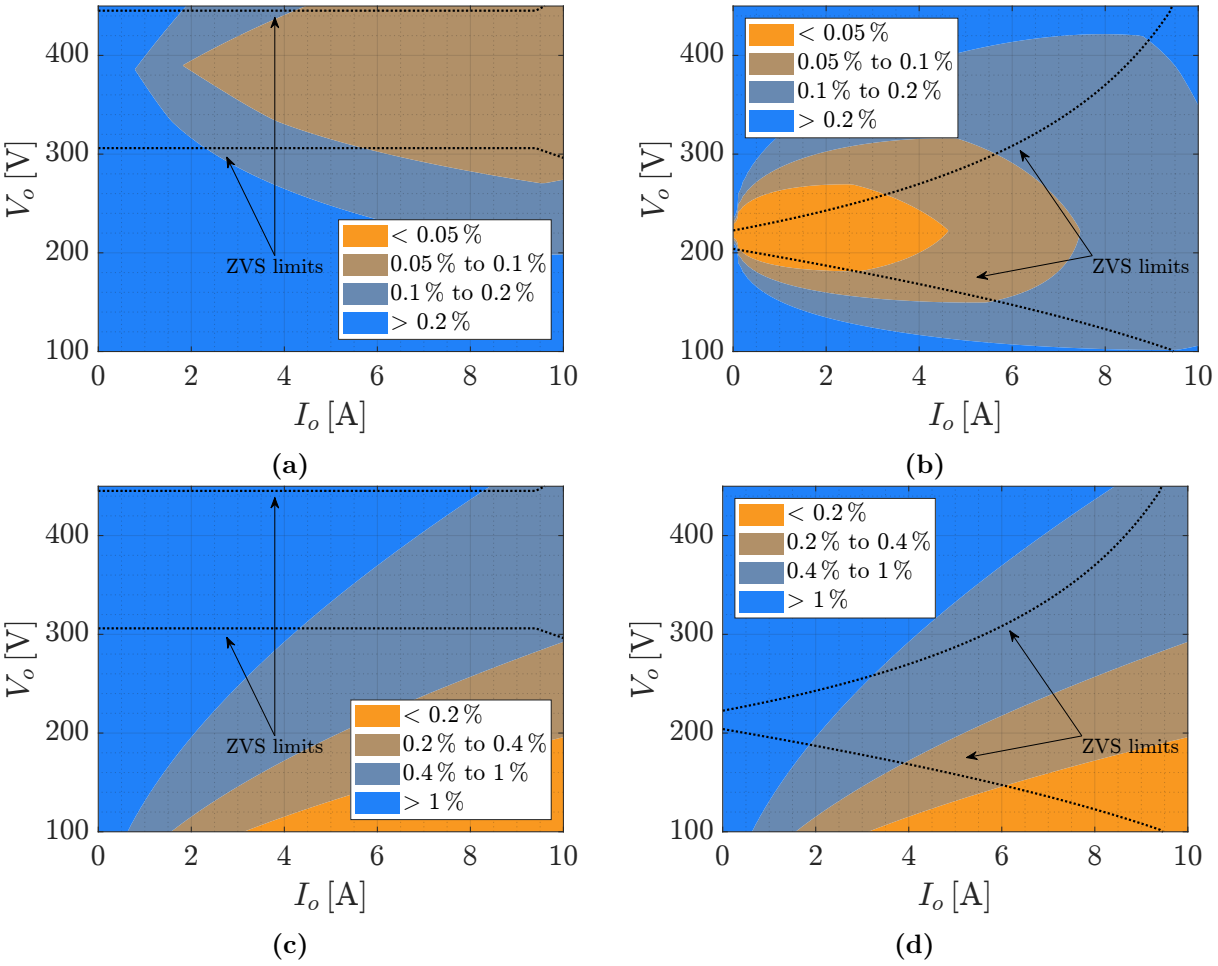

Figure 3.19 – Reduction in converter efficiency due core loss for (a) inductor with iDY transformer (b) inductor with YY transformer (c) transformer with iDY transformer (d) transformer with YY transformer

3.4 CONCLUSION

In this chapter, a Reconfigurable Transformer Connection Strategy was introduced. The idea behind this approach was to exploit the fact that DAB3 ZVS region changed depending on its connection configuration, leading to different optimal operating points for the converter. By using three NO NC relays, the switching of this transformer could be controlled. To assess the potential advantages of this strategy, the ideal ZVS regions calculated in Chapter 2 were presented. All combinations where one side of the 3ϕ network was fixed were explored, including: iDD and oDD; iDY and oDY; YD and oDD; YD and iDD; oDY and YY; YY and iDY. Visual representations of the ZVS regions for these combinations were provided, with varying n and L_{dab} values, covering a wide range from 200 V to 400 V and 0 A to 10 A in the load.

The pair YY and iDY was chosen to compare one of the cases. To verify the converter correct operation, two points, A and B, were selected, and theoretical and practical inductor currents were shown for each. This confirmed the proper functioning of the converter with both transformer options. Additionally, an efficiency analysis of

the converter was conducted, considering various sources of losses, such as conduction losses, switching losses, coil losses, core losses, and series capacitor losses. The theoretical efficiency was compared with the practical efficiency obtained, validating the loss model.

Finally, comments were made regarding sources of losses for each transformer in different operating regions. It was observed that not only switching losses but most losses were reduced when the converter operated in the ZVS region due to the inherently lower stresses in this region. However, this conclusion did not apply to core losses in the transformer, as they only depended on the output voltage.

Chapter

4 DAB3 optimization design converters using RTCS.

In this chapter, it is assumed that the loss calculation presented in the previous chapter is valid. Consequently, the investigation focuses on whether the RTCS can improve at least one of the following aspects: price, volume and/or efficiency. Thus, an optimization routine is presented for a conventional DAB3, followed by the optimization with the RTCS. The DC-DC stage of a fast charger is chosen for optimization to illustrate, as this is an application that needs to handle significant voltage variations in the load. A comparison between these two cases is conducted, and the results are discussed.

4.1 ALGORITHMIC APPROACH FOR OPTIMAL DESIGN

During the prototype assemblying presented in the previous chapter, separate design methodologies were employed for the inductor and transformer. Additionally, a typical switching frequency was used for the considered power level. However, in this chapter, an unified design approach is adopted, since all converter main losses are integrated into a single routine. The aim is to achieve high efficiency by extrapolating the loss models that were validated with the prototype in the previous section to a theoretical design.

The initial step is to select the design variables, which are: number of turns in the inductor (N_L); inductor air gap length (l_g); number of turns in the primary winding (N_p); number of turns in the secondary winding (N_s); switching frequency (f_s); and 3ϕ network. Subsequently, a routine is developed to assess whether the converter can operate under a given set of parameters and calculate the total converter loss. The process is outlined in Figure 4.1. The algorithm considers fixed core materials for the transformer and inductor, predetermined wire properties and a constant dead time.

The first step involves setting the error flag e_{flag} to low and the total loss P_{tot} to a very high value, for example, infinity. Throughout the algorithm, both e_{flag} and P_{tot} can have their values altered. Then, the algorithm estimates the parameters of the magnetic elements, including L_{dab}, M, L_1, and L_2, using the equations presented in Appendix B.

Now, with the magnetic elements determined, the subsequent stages involve utilizing

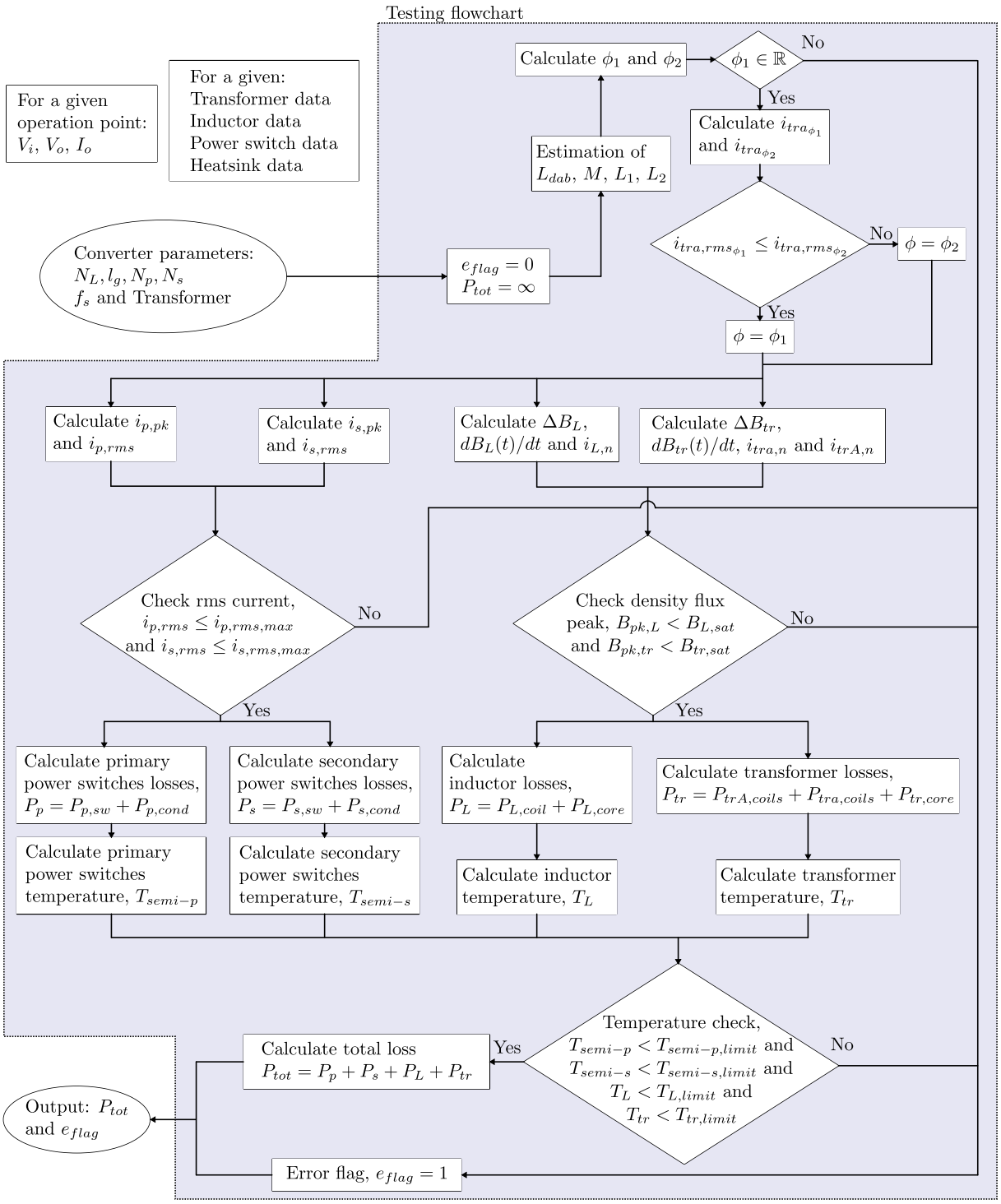

Figure 4.1 – Viability check and total loss calculation flowchart

equations presented in Appendix A to calculate the converter stress. The algorithm proceeds to identify the possible angles ϕ_1 and ϕ_2. It verifies the existence of real values for these angles and selects the one that results in the lowest RMS current through the transformer for further calculations. Next, it computes all the necessary parameters for measuring the losses. Additionally, the algorithm checks if the RMS current in the power switches remains within the allowable limit and confirms that the peak flux in both the inductor and

transformer is below the core saturation level. If these conditions are met, it estimates the losses in the power switches, inductor, and transformer. Based on these losses, it evaluates the temperature elevation and compares them against acceptable limits. If the temperature value falls within the acceptable range, the total loss is calculated. If any of the constraints are not met, the error flag e_{flag} is set to high, and the losses are not calculated. The algorithm provides an output that includes the error flag indicating whether any constraint is violated and the value of the total losses.

The algorithm in Figure 4.2 is designed to explore and vary the converter parameters iteratively until an optimal solution is achieved. It utilizes the algorithm presented in Figure 4.1 to assess the feasibility of different points and compute the total loss. This systematic approach enables the exploration of various parameter combinations and facilitates the identification of the most efficient converter design.

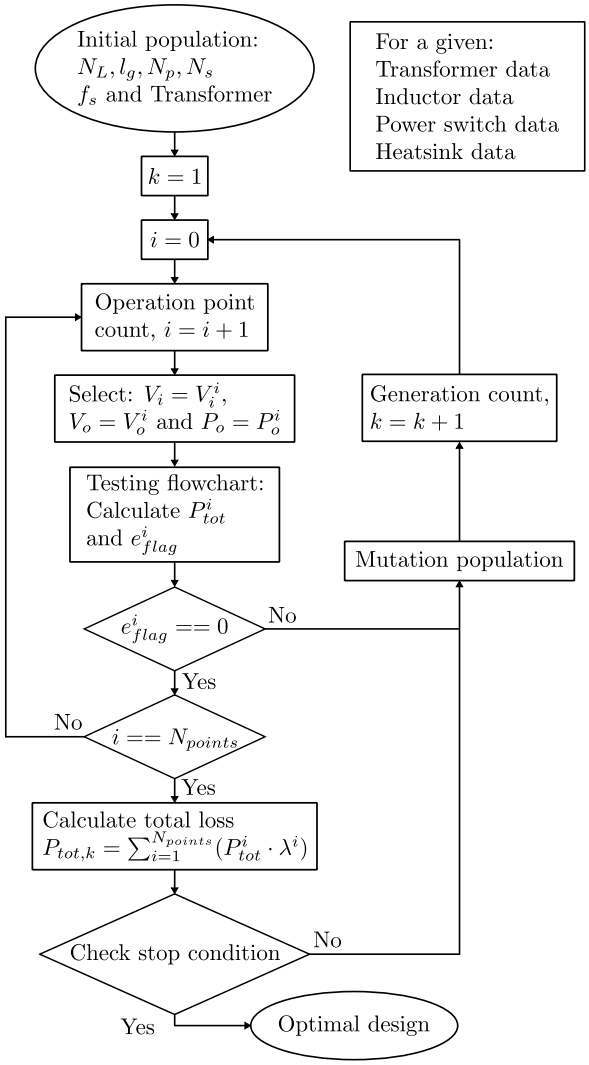

Figure 4.2 – Design flowchart for obtaining optimum parameters for conventional DAB3

The algorithm aims to optimize the converter for N_{points} operating points. The objective is to minimize the sum of converter losses for these operating points. The losses can be weighted by the vector λ. If the converter fails to operate at least at one of the operating points, the parameters are mutated, and the algorithm attempts to find a population set in which all operations points are operable and have the lowest sum of losses, achieving the optimal design.

With the goal of designing a system that incorporates two 3ϕ network, a new parameter called V_{div} is introduced. This parameter represents the optimal voltage at which the transformer switching occurs. Figure 4.3 illustrates an example of the utilization of this new parameter. In this graph, Transformer_1 and Transformer_2 represent options for two 3ϕ networks.

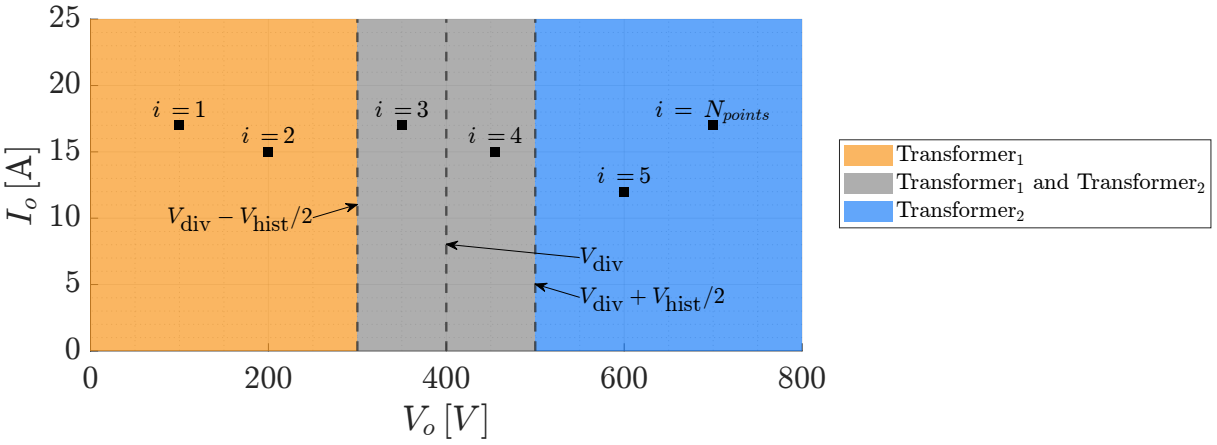

Figure 4.3 – Example of hysteresis operation with $V_{\text{div}} = 400\,\text{V}$ and $V_{\text{hist}} = 200\,\text{V}$ for 6 points to be optimized.

The graph presents six operation points that are subject to optimization. Points 1 to 3 correspond to operation with the first 3ϕ network, while points 4 to 6 correspond to operation with the second 3ϕ network. To ensure a safe margin for transformer switching, a hysteresis parameter called V_{hist} is introduced. The range $(V_{\text{div}} - V_{\text{hist}}/2)$ to $(V_{\text{div}} + V_{\text{hist}}/2)$ is designated as the hysteresis region, within which both 3ϕ networks must be capable of operating. Specifically, points 3 and 4 must satisfy the operational requirements for both networks.

Figure 4.4 presents the methodology for designing the converter considering two 3ϕ networks. Unlike the option with a single 3ϕ network, here, each transformer can operate at a different frequency. Thus, the algorithm takes into account a total of 9 parameters: N_L, l_g, N_p, N_s, f_{s1}, f_{s2}, Transformer_1, Transformer_2 and V_{div}. It follows a similar approach to the algorithm for a single transformer, but with an additional step. Before calculating the losses and error flag for each operating point, the algorithm checks the hysteresis, based on V_{div}, to determine if that specific operating point should be associated with a particular transformer. If it is not necessary, the operating point is ignored, since it does not need to be able to operate in that operation point.

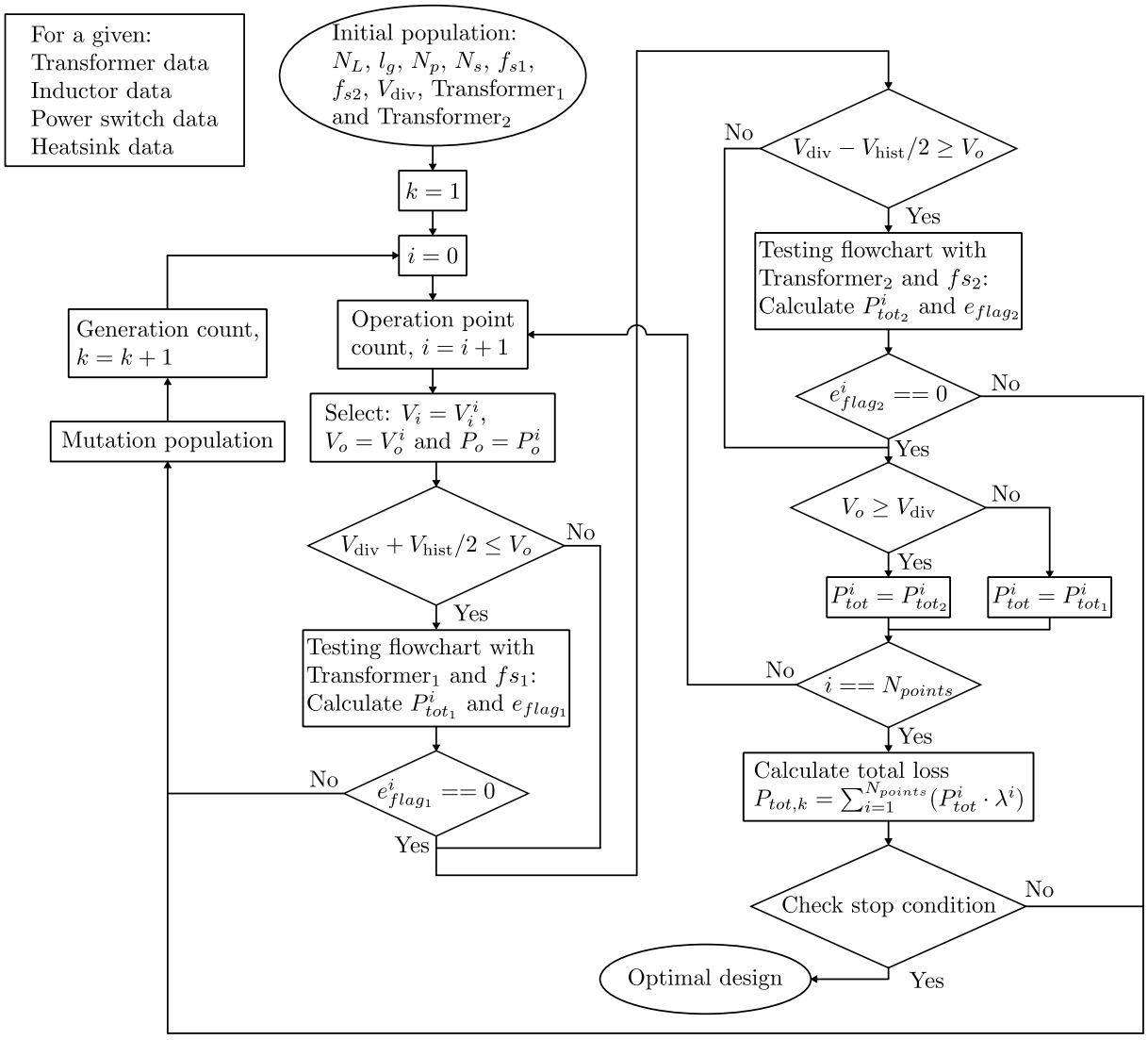

Figure 4.4 – Design flowchart for obtaining optimum parameters for DAB3 with RTCS

MATLAB R2022a software is used for the optimization routines, employing the Particle Swarm Optimization (PSO) algorithm for both flowcharts presented in Figure 4.2 and 4.4. In PSO, particles, representing individuals, search for the best solution in a multi-dimensional problem space. Each particle maintains its own knowledge and adjusts its position and velocity based on its experience and communication with other particles. Through iterative updates to their positions and velocities, particles strive to converge towards an optimal solution [38].

The flowchart presented in Figure 4.5 illustrates the methodology used to calculate the optimal design for multiple combinations of components. In this flowchart, the block for calculating the optimal design can consider either a single 3ϕ network or the RTCS.

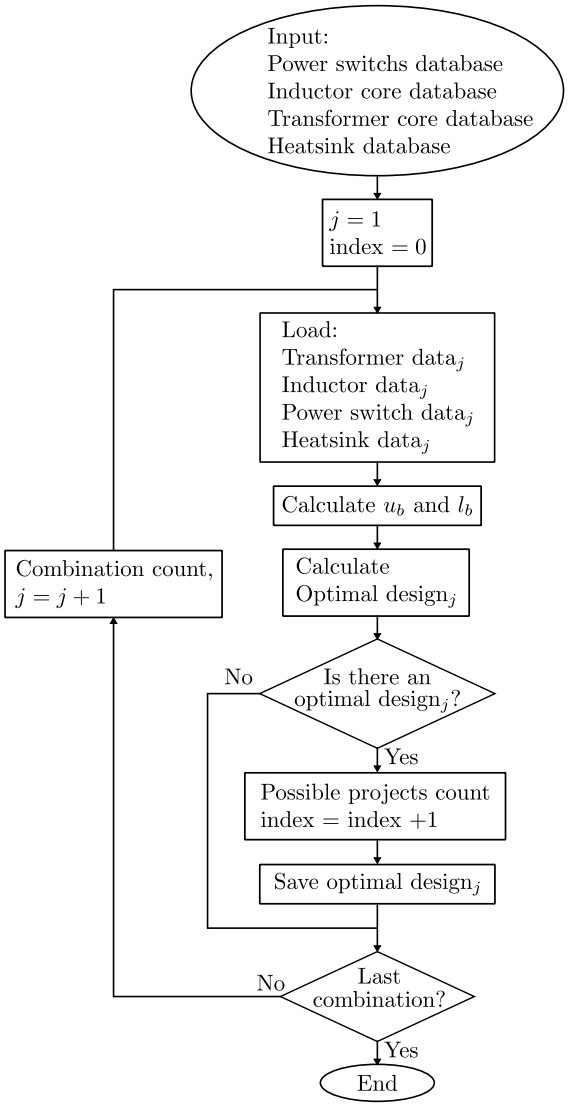

Figure 4.5 – Design flowchart for multiples components combinations

The flowchart starts by loading a database, and then a set of components, including a transformer, inductor, power switch, and heatsink. With these components, the upper bounds (u_p) and lower bounds (l_b) for the optimization routes are calculated. For example, the maximum number of turns is calculated in this stage. Some limits are independent of the loaded components, such as the gap in the inductor, set at a maximum value of 1.5 mm, and the switching frequency, which must be between 20 kHz and 150 kHz.

4.2 THEORETICAL DESIGN OF A GENERAL-PURPOSE EV CHARGER MODULE

In this section, the theoretical design of a general-purpose EV charger module is conducted using the two algorithms presented in Figure 4.2 and Figure 4.4. Considering the application requirement to handle a wide variation in load voltage and current, the implementation of the second 3ϕ network can be advantageous. Additionally, since it involves battery charging, interrupting the charging process momentarily to switch the

relays and then resuming battery charging should not pose any issues. Both algorithms design the DAB3 converter with the same loss model and modulation scheme, allowing for a fair evaluation of the impact of incorporating a second transformer on efficiency, volume, and/or cost reduction.

Figure 3.4 presents the operating range of output voltage/current for general-purpose EV charger modules. Assuming the fast charger consists of 32 sub-modules in parallel, with each sub-module comprising a DAB3, Figure 4.6 shows the operating range of output voltage/current for a single sub-module. The dots indicate the selected operating points for optimization. The converter has maximum power of 12.5 kW, with a maximum voltage of 800 V and a maximum current of 25 A. The input voltage is also assumed to be 800 V.

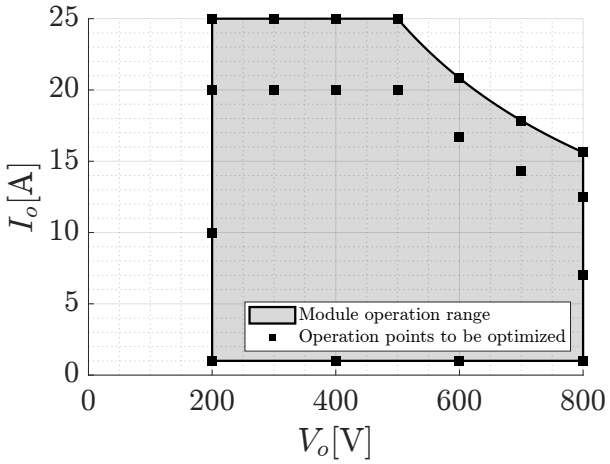

Figure 4.6 – Operating region of a sub-module along with dots (■) representing the selected operating points for optimization

The optimization focuses on high-current operating points since it is assumed that the converter will mostly operate at high current levels. Even if the battery requires slower charging, instead of reducing power through the converter, specific converters can be turned off. Hence, the sub-module converter tends to operate at high current. The weighting vector λ is set to one for all points with current above 10 A, while points with lower current are assigned a very small value. This ensures that the system can operate in low-current regions but prioritizes high efficiency for higher current points.

Various designs are explored, taking into account different materials for the optimization process. The power switches, heatsinks, and cores of both the transformer and the inductor are considered with specific materials, which are listed in Table 4.1 for power switches, Table 4.2 for heatsinks, and Table 4.3 for transformer and inductor cores. Some parameters are kept fixed throughout the optimization, such as using 588x38AWG litz wires for all windings and a constant dead time of 200 ns. Additionally, it is assumed that the same power switch and heatsink are utilized for both the primary and secondary sides. A voltage hysteresis (V_{hist}) of 200 V is also considered in the analysis.

Table 4.1 – Discrete silicon carbide MOSFETs database for theoretical design.

Code	Blocking Voltage	R_{ds-on}	Total Gate Charge	Unit Price
C3M0016120K	1200 V	16 mΩ	211 nC	$70.4
C3M0021120K	1200 V	21 mΩ	162 nC	$33.0
C3M0032120K	1200 V	32 mΩ	118 nC	$25.5
C3M0040120K	1200 V	40 mΩ	99 nC	$19.1
C3M0075120K	1200 V	75 mΩ	53 nC	$13.7

Table 4.2 – Miniature cooling aggregates database for theoretical design.

Code	Dimensions	Thermal resistance	Volume	Unit Price
LAM5K15024	50x50x150 mm	0.27 K/W	375 cm^3	$52.7
LAM4K15012	40x40x150 mm	0.65 K/W	240 cm^3	$54.0
LAM3K15012	30x30x150 mm	1.50 K/W	135 cm^3	$36.2

Table 4.3 – Cores database for theoretical design.

Inductors core			Transformers core		
Code	Volume	Unit Price	Code	Volume	Unit Price
E80/38/20 N97	62.2 cm^3	$11.2	E100/60/28 N97	163.8 cm^3	$22.3
E70/32/33 N97	74.9 cm^3	$10.0	E80/38/20 N97	62.2 cm^3	$11.2
E55/28/21 N97	38.2 cm^3	$6.5			

The components database presented lead to 90 ($5 \times 3 \times 3 \times 2$) unique combinations, and the algorithm found solutions for 24 different component combinations. These combinations and their respective total losses are depicted in Figure 4.7.

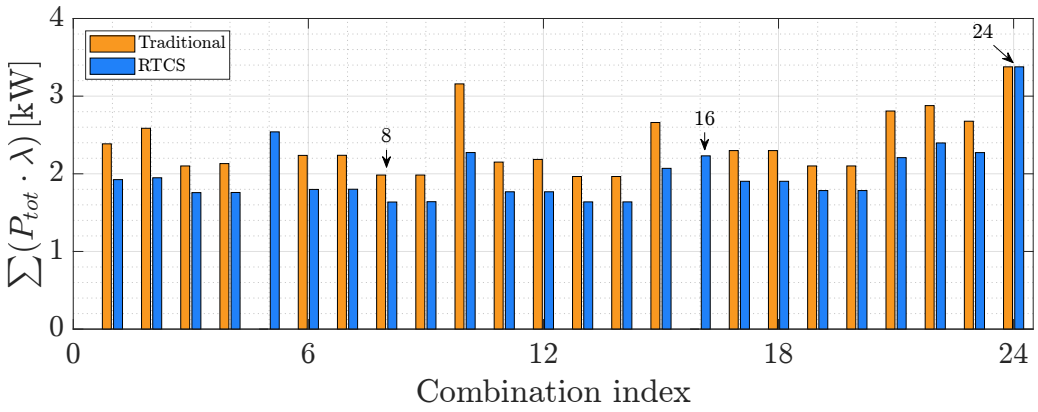

Figure 4.7 – Design for each combination of materials

Regarding price comparison, it is calculated by considering only the inductor core, transformer core, primary and secondary heat sinks, and power switches. As for volume, it includes the volume of the inductor and transformer cores, as well as the primary and secondary heat sinks. These combinations are depicted in terms of cost and volume in Figures 4.8 (a) and (b), respectively. In those graphs, Pareto Front for each strategy is also

presented. Since the Pareto front from RTCS exhibits lower losses than the conventional approach, it also demonstrates the benefit of this strategy.

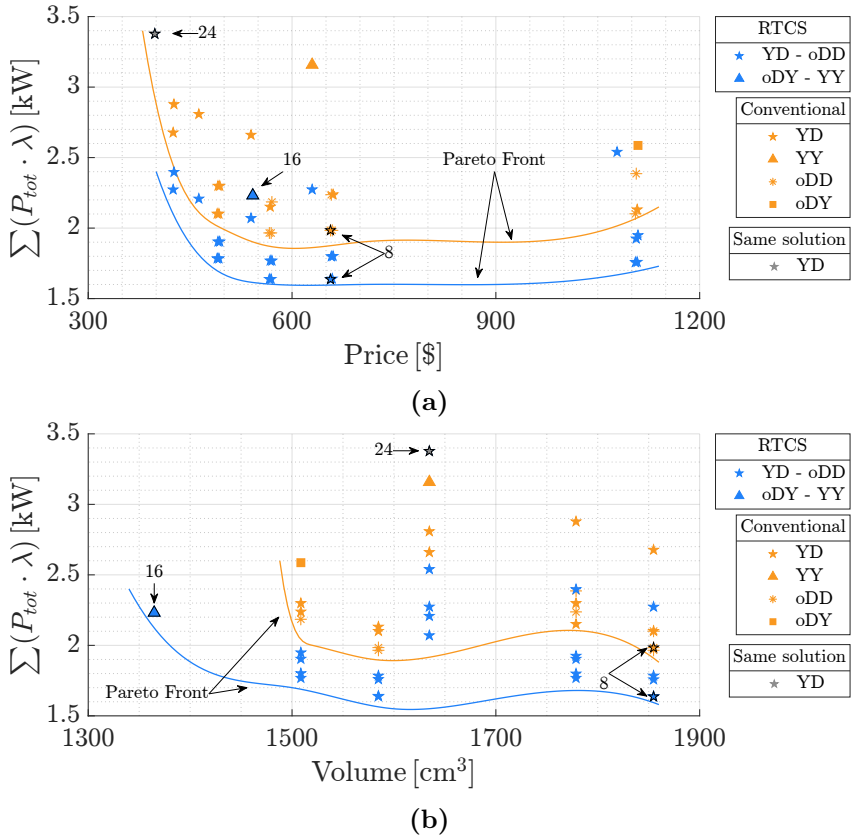

Figure 4.8 – (a) Multiple projects as functions of the sum of losses and price (b) Multiple projects as functions of the sum of losses and volume

The type of dot in Figure 4.8 indicates which 3ϕ network each component combination found to have the lowest sum of losses. Figure 4.9 displays the percentage distribution of selected 3ϕ networks chosen for each situation.

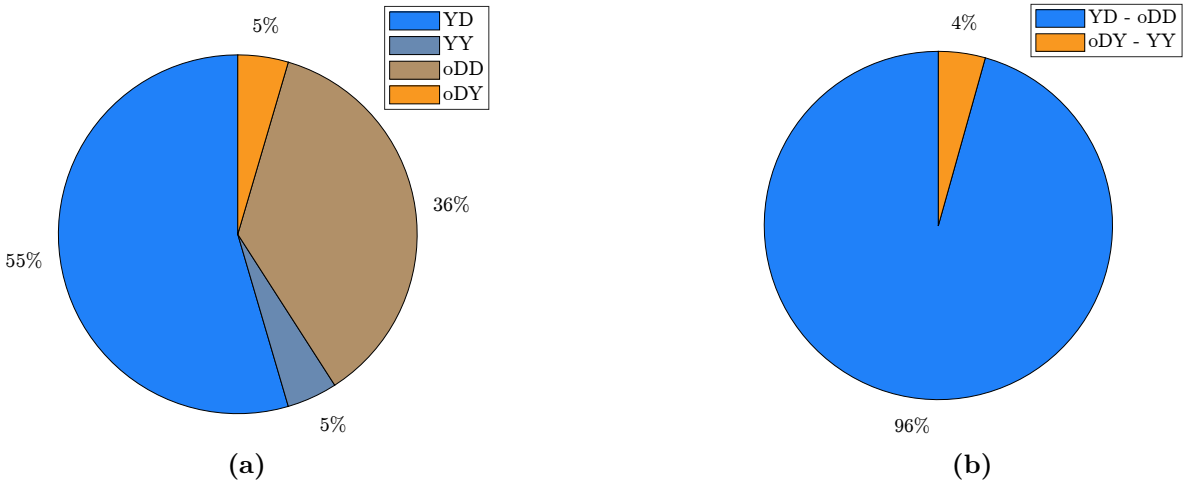

Figure 4.9 – (a) Percentage of 3ϕ networks with a single transformer (b) Percentage of pairs of 3ϕ networks with a switched transformer strategy

Figure 4.9 (a) shows the distribution of selected 3ϕ networks by the optimization routine for the conventional DAB3. It is evident that the YD configuration is the most frequently chosen. Figure 4.9 (b) illustrates the pairs of 3ϕ networks chosen, indicating that almost all designs opted for the combination of YD with oDD.

The RTCS results in lower losses compared to the conventional approach for the same set of components. The percentage difference in total losses is calculated and depicted in Figure 4.10 to show the extent of this improvement. The majority of reductions in losses fall within the range of 15 % to 20 %, with a maximum reduction of 28 %. However, in one situation, the presence of the second transformer did not provide any advantage, resulting in 0 % reduction in losses. Additionally, it is not shown in this graph, but there are two cases where the presence of the second transformer enabled the converter to be designed with a specific set of components.

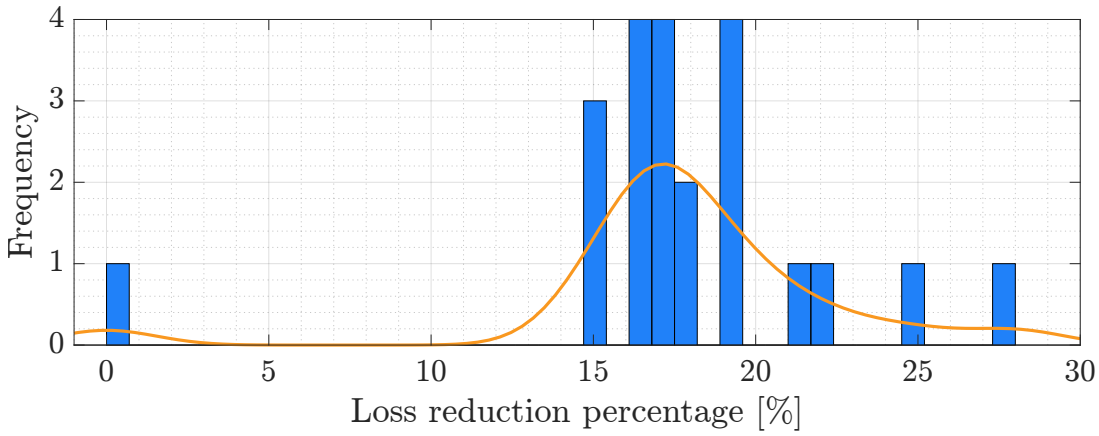

Figure 4.10 – Percentage of loss reduction with RTCS compared to the conventional

Three component combinations stand out: 8, 16, and 24. Combination 8 exhibits the lowest loss, combination 16 has the smallest volume, and combination 24 has the lowest cost. For component combination number 16, which has the smallest volume, the optimization routine did not find a viable single-transformer solution, while it did find with the RTCS. On the other hand, in project combination 24, both routines found the same solution, indicating that even the routine considering two transformers identified a point where one of the transformers is completely unused. In this case, the option to switch the transformer provides no advantage. Table 4.4 summarizes the optimal designs of this three paramaters combination, including selected 3ϕ networks, switching frequency, construction parameters of magnetic materials, inductance values, maximum operating temperature and maximum peak flux density.

Table 4.4 – Summary of optimum design for components combinations 8, 16 and 24.

	Comb. index 8			Comb. index 16		Comb. index 24
P.S.	C3M0021120K			C3M0032120K		C3M0075120K
Heatsink	LAM5K15024			LAM4K15012		LAM5K15024
Transf.	100/60/28-N97			100/60/28-N97		100/60/28-N97
Induct.	70/33/32-N97			55/28/25-N97		55/28/25-N97
	Conventional	RTCS		RTCS		Conventional
$\sum(P_{tot} \cdot \lambda)$	1984 W	1637 W		2231 W		3377 W
3ϕ network	oDD	YD	oDD	YY	oDY	YD
f_s	45.3 kHz	47.9 kHz	30.8 kHz	69.5 kHz	52.3 kHz	87.8 kHz
N_p	22	22		22		18
N_s	19	22		11		22
N_L	10	10		8		8
l_g	0.85 mm	0.73 mm		0.62 mm		0.75 mm
V_{div}	-	582 V		443 V		-
L_{dab}	60.9 μH	69.1 μH		33.1 μH		28.5 μH
L_{tr1}	5.4 μH	5.4 μH		5.4 μH		3.6 μH
L_{tr2}	4.0 μH	5.4 μH		1.3 μH		5.4 μH
L_m	3.4 mH	3.4 mH		3.4 nH		2.3 mH
T^{max}_{semi-p}	65.2 °C	50.5 °C		84.4 °C		83.2 °C
T^{max}_{semi-s}	51.4 °C	46.8 °C		87.6 °C		51.4 °C
T^{max}_{tr}	70.9 °C	70.2 °C		83.3 °C		78.0 °C
T^{max}_{L}	88.3 °C	75.9 °C		93.9 °C		100 °C
B^{max}_{L-pk}	229 mT	238 mT		239 mT		184 mT
B^{max}_{tr-pk}	211 mT	267 mT		210 mT		94 mT

Figure 4.11 presents the operating region and efficiency of both projects with components parameters 8. The absence of color in certain regions indicates that the converter cannot operate in those areas, in other words, at least one of the constraints presented in Figure 4.1 cannot be satisfied. In Figure 4.11 (a), the design with a single transformer is shown, while Figure 4.11 (b) displays the switched transformer strategy, with $V_{\text{div}} = 582$ V, where the switch between 3ϕ networks occurs. Additionally, Figures 4.11 (c) and (d) illustrate the operating regions of each individual 3ϕ network. The switched transformer strategy results in a total loss of 1637 W, which represents a reduction of 17.8 % in the total loss compared to the single transformer, which has a total loss of 1984 W.

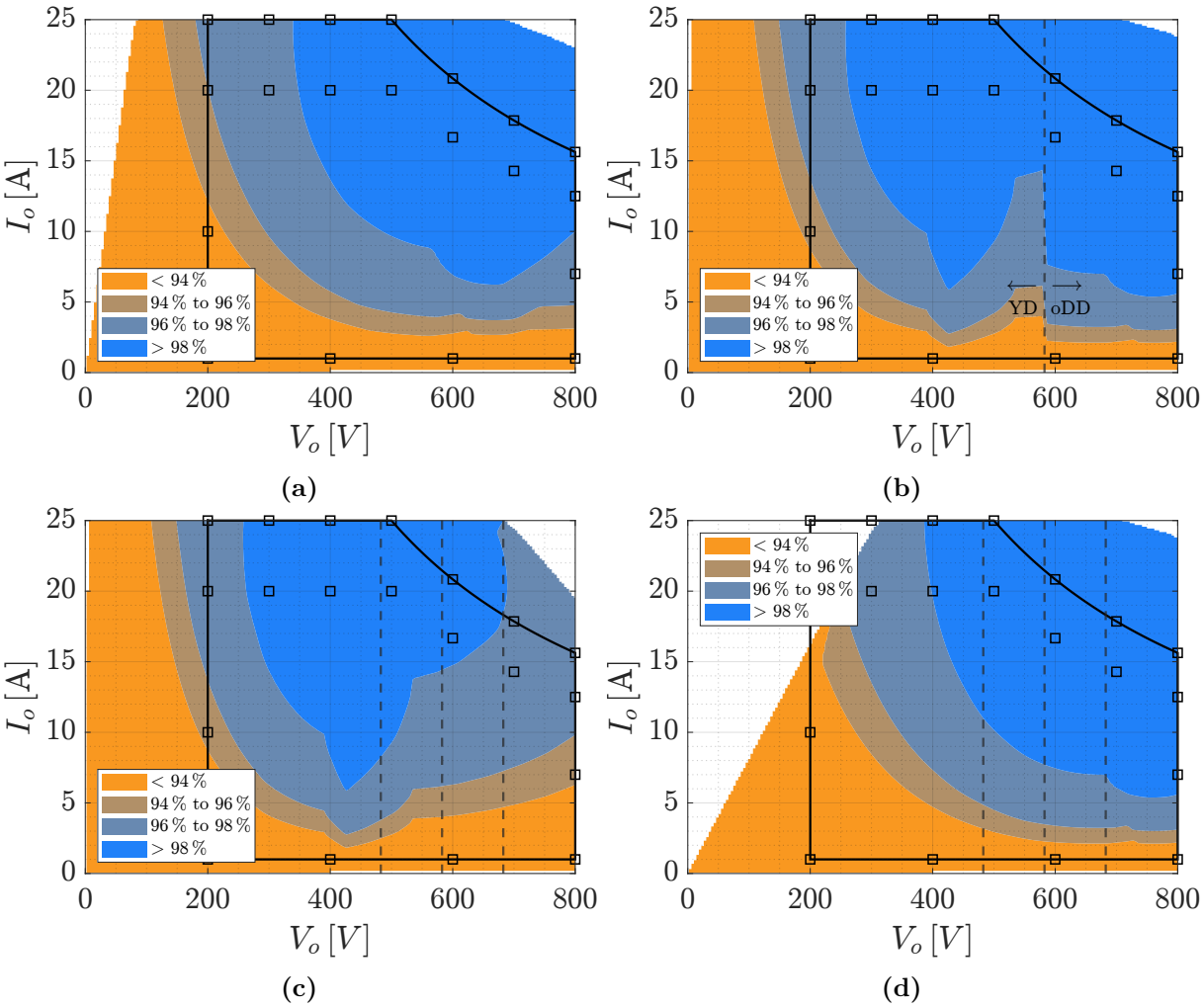

Figure 4.11 – Operating region and efficiency of DAB3 for parameters combination number 8: (a) Conventional, (b) RTCS, (c) the first 3ϕ network from the RTCS, and (d) the second 3ϕ network from the RTCS

Figure 4.11 presents the operating region and efficiency of both projects with components parameters 16. Figure 4.12 depicts the operating region and efficiency for this case. Figure 4.12 (a) shows the design considering both 3ϕ networks, with $V_{\text{div}} = 443\,\text{V}$, while Figures 4.12 (b) and (c) display the operating regions of each individual 3ϕ network.

Figure 4.13 illustrates the operating region of the project with component combination 24. In this case, both optimization routines found the same solution. Consequently, the optimal solution is achieved with a single 3ϕ network. This scenario may be influenced by the characteristics of the power switches used, as they exhibit high conduction losses and low switching losses. As a result, the presence or absence of ZVS may not have a significant impact on the overall performance in this particular case.

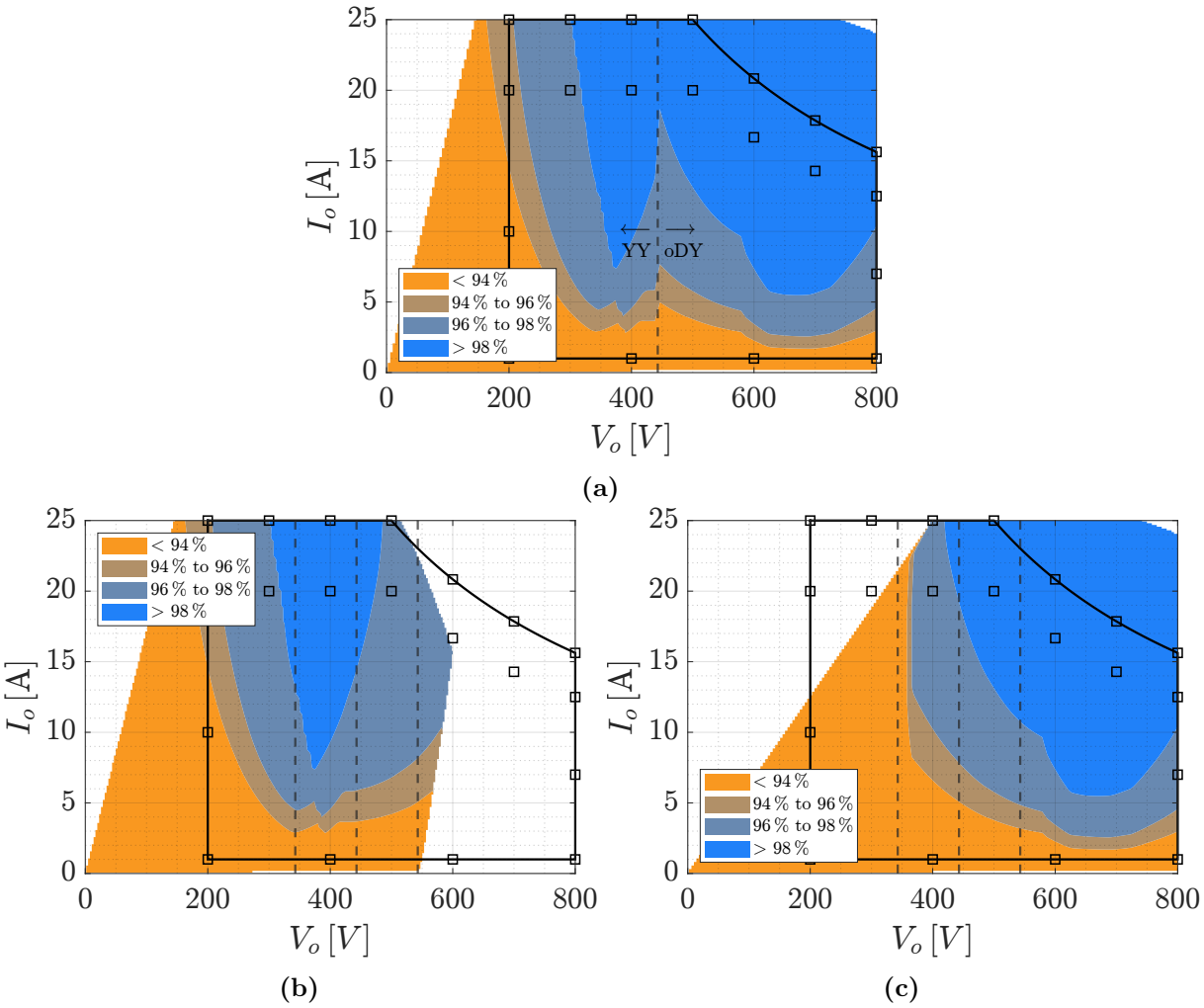

Figure 4.12 – Operating region and efficiency of DAB3 for parameters combination number 16: (a) RTCS, (b) the first 3ϕ network from the RTCS, and (c) the second 3ϕ network from the RTCS

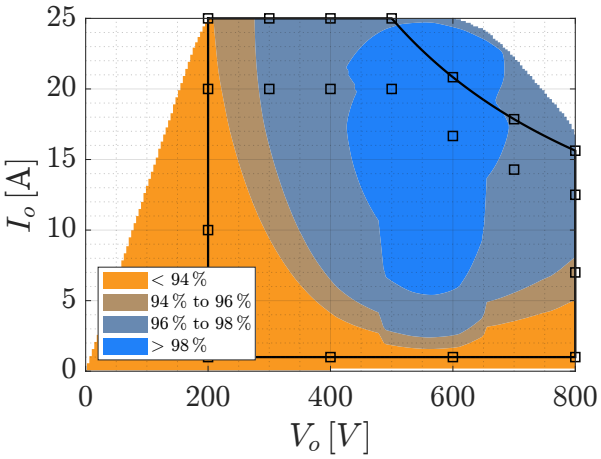

Figure 4.13 – Operating region and efficiency of DAB3 for parameters combination number 24

4.3 CONCLUSION

In this chapter, the theoretical converter design utilized the established equations from the previous chapters. An algorithm was developed to assess the feasibility of the project and calculate the losses based on the input converter parameters. Through PSO routines, the code efficiently minimized the total losses across various operating points, providing the optimal construction parameters and the best 3ϕ network for both single transformer and RTCS.

A DC-DC converter project was conducted for a fast charger, examining multiple combinations of components. The results demonstrated that implementing the RTCS led to significant reductions in losses, ranging from 15% to 20% in most cases, with some instances even achieving up to 28% reduction. Additionally, certain combinations of parameters that previously lacked the capacity to handle specific power levels now proved sufficient with the incorporation of this technique.

The algorithm modular nature allows for potential future enhancements such as:

- Adapting the algorithm to operate with variable frequencies, optimizing the converter performance at different operating points, while still utilizing existing base equations;
- Improving the accuracy of calculations for losses and temperature rise;
- Enhancing the constraints, such as incorporating checks to ensure that the voltage ripple for a given capacitor remains below a certain threshold, for both input and output DC buses;
- Adding additional parameters to the population to be optimized, such as transformer isolation thickness to control leakage inductance [39];
- Exploring different modulation techniques, which is feasible, although it would require recalculating the underlying equations to accommodate varying duty-cycle ratios ($D_1 \neq 0.5$ and $D_2 \neq 0.5$).

By incorporating these enhancements, the algorithm can offer increased versatility and effectiveness in designing optimal converters, both with and without the RTCS.

Chapter

5

Conclusion

The Three-Phase Dual Active Bridge Converter holds significant importance in the field of power electronics, especially in medium to high-power applications. It emerges as a viable solution for various critical areas, such as battery charging systems, electric vehicles, renewable energy converters, and other advanced power conversion technologies. Its remarkable flexibility in modulation techniques and potential switching strategies makes it a versatile and promising topology to address the growing challenges of energy efficiency and sustainability in our modern world.

Chapter 2 conducted a comprehensive steady-state analysis of the DAB3 using phase-shift modulation. The analysis yielded essential stress equations that formed the foundation for all subsequent chapters. Furthermore, it explored the converter switching behavior and, through analytical equations, verified its operation in the Zero Voltage Switching mode, dependent on the operating point and dead time.

In Chapter 3, the Reconfigurable Transformer Connection Strategy was introduced, along with its conception and potential applications. A prototype was built and tested at various operational points, demonstrating the validity of theoretical equations. A comparison between theoretical efficiency and experimental results showed promising efficiency gains with the implementation of this strategy.

Chapter 4 developed an algorithm for the theoretical optimal design of the converter, considering loss and thermal models used in this work. The results demonstrated that the implementation of the switched transformer strategy leads to substantial enhancements in efficiency. By employing this new strategy, it is possible to either reduce the total loss while keeping the same components, or use a smaller set of components for the design, thereby reducing the overall volume of the converter.

5.1 FUTURE WORKS

The following topics are suggested for future work:

- Develop stress and static gain equations considering parasitic capacitors, dead time

and body diode;

- Analysis of the converter with more complex modulation techniques;
- Integration of the loss model with the thermal model for a comprehensive analysis of converter performance;
- Comparison between the DAB3 and resonant versions to assess the advantages and limitations of each design;
- Development of balancing techniques for the three-phase currents to enhance the converter efficiency.

Bibliography

[1] L. Freris and D. Infield, "Electrical power generation and conditioning," *Renewable Energy in Power Systems*, 2008.

[2] M. H. Saeed, W. Fangzong, B. A. Kalwar, and S. Iqbal, "A review on microgrids' challenges perspectives," *IEEE Access*, vol. 9, pp. 166502–166517, 2021.

[3] Q. Xu, N. Vafamand, L. Chen, T. Dragicevic, L. Xie, and F. Blaabjerg, "Review on advanced control technologies for bidirectional dc/dc converters in dc microgrids," *IEEE Journal of Emerging and Selected Topics in Power Electronics*, vol. 9, pp. 1205–1221, 4 2021.

[4] M. Lee, W. Choi, H. Kim, and B. H. Cho, "Operation schemes of interconnected dc microgrids through an isolated bi-directional dc-dc converter," *Conference Proceedings - IEEE Applied Power Electronics Conference and Exposition - APEC*, vol. 2015-May, pp. 2940–2945, 5 2015.

[5] H.-S. Kim, M.-H. Ryu, J.-W. Baek, and J.-H. Jung, "High-efficiency isolated bidirectional ac–dc converter for a dc distribution system," *IEEE Transactions on Power Electronics*, vol. 28, pp. 1642–1654, 4 2013.

[6] M. Safayatullah, M. T. Elrais, S. Ghosh, R. Rezaii, and I. Batarseh, "A comprehensive review of power converter topologies and control methods for electric vehicle fast charging applications," *IEEE Access*, vol. 10, pp. 40753–40793, 2022.

[7] G. R. C. Mouli, P. Venugopal, and P. Bauer, "Future of electric vehicle charging," pp. 1–7, IEEE, 10 2017.

[8] L. Zhang, B. Shaffer, T. Brown, and G. S. Samuelsen, "The optimization of dc fast charging deployment in california," *Applied Energy*, vol. 157, pp. 111–122, 11 2015.

[9] "Enabling extreme fast charging: A technology gap assessment | department of energy," 8 2017. https://www.energy.gov/eere/vehicles/articles/enabling-extreme-fast-charging-technology-gap-assessment.

[10] S. Rivera, S. Kouro, S. Vazquez, S. M. Goetz, R. Lizana, and E. Romero-Cadaval, "Electric vehicle charging infrastructure: From grid to battery," *IEEE Industrial Electronics Magazine*, vol. 15, pp. 37–51, 6 2021.

[11] A. Khaligh and M. Dantonio, "Global trends in high-power on-board chargers for electric vehicles," *IEEE Transactions on Vehicular Technology*, vol. 68, pp. 3306–3324, 4 2019.

[12] F. Krismer, *Modeling and optimization of bidirectional dual active bridge DC-DC converter topologies*. PhD thesis, ETH Zürich, 2010. Available at `https://doi.org/10.3929/ethz-a-006395373`.

[13] J. Wang, B. Wang, L. Zhang, J. Wang, N. Shchurov, and B. Malozyomov, "Review of bidirectional dc–dc converter topologies for hybrid energy storage system of new energy vehicles," *Green Energy and Intelligent Transportation*, vol. 1, p. 100010, 9 2022.

[14] M. K. Kazimierczuk, "High-frequency magnetic components: Second edition," *High-Frequency Magnetic Components: Second Edition*, pp. 1–729, 11 2013.

[15] A. Kumar, A. H. Bhat, and P. Agarwal, "Comparative analysis of dual active bridge isolated dc to dc converter with flyback converters for bidirectional energy transfer," *2017 Recent Developments in Control, Automation and Power Engineering, RDCAPE 2017*, pp. 382–387, 5 2018.

[16] R. W. D. Doncker, M. H. Kheraluwala, and D. M. Divan, "Power conversion apparatus for dc/dc conversion using dual active bridges," 9 1989.

[17] R. W. D. Doncker, D. M. Divan, and M. H. Kheraluwala, "A three-phase soft-switched high-power-density dc/dc converter for high-power applications," *IEEE Transactions on Industry Applications*, vol. 27, pp. 63–73, 1991.

[18] N. Blasuttigh, H. Beiranvand, T. Pereira, and M. Liserre, "Comparative study of single-phase and three-phase dab for ev charging application," *2022 24th European Conference on Power Electronics and Applications (EPE'22 ECCE Europe)*, pp. 1–9, 2022.

[19] T. Jimichi, M. Kaymak, and R. W. D. Doncker, "Comparison of single-phase and three-phase dual-active bridge dc-dc converters with various semiconductor devices for offshore wind turbines," *2017 IEEE 3rd International Future Energy Electronics Conference and ECCE Asia, IFEEC - ECCE Asia 2017*, pp. 591–596, 7 2017.

[20] H. V. Hoek, M. Neubert, A. Kroeber, and R. W. D. Doncker, "Comparison of a single-phase and a three-phase dual active bridge with low-voltage, high-current output,"

2012 International Conference on Renewable Energy Research and Applications (ICRERA), 2012.

[21] J. Xue, F. Wang, D. Boroyevich, and Z. Shen, "Single-phase vs. three-phase high density power transformers," *2010 IEEE Energy Conversion Congress and Exposition, ECCE 2010 - Proceedings*, pp. 4368–4375, 2010.

[22] L. M. Cúnico, *Estratégias de projeto e modulação para o conversor DAB trifásico*. PhD thesis, INEP – Instituto de Eletrônica de Potência - UFSC - Universidade Federal de Santa Catarina, 2021. Available at `https://repositorio.ufsc.br/handle/123456789/229203`.

[23] J. Huang, Z. Li, L. Shi, Y. Wang, and J. Zhu, "Optimized modulation and dynamic control of a three-phase dual active bridge converter with variable duty cycles," *IEEE Transactions on Power Electronics*, vol. 34, pp. 2856–2873, 3 2019.

[24] J. Hu, N. Soltau, and R. W. D. Doncker, "Asymmetrical duty-cycle control of three-phase dual-active bridge converter for soft-switching range extension," *ECCE 2016 - IEEE Energy Conversion Congress and Exposition, Proceedings*, 2016.

[25] H. V. Hoek, M. Neubert, and R. W. D. Doncker, "Enhanced modulation strategy for a three-phase dual active bridge - boosting efficiency of an electric vehicle converter," *IEEE Transactions on Power Electronics*, vol. 28, pp. 5499–5507, 2013.

[26] L. M. Cunico, Z. M. Alves, and A. L. Kirsten, "Efficiency-optimized modulation scheme for three-phase dual-active-bridge dc-dc converter," *IEEE Transactions on Industrial Electronics*, vol. 68, pp. 5955–5965, 7 2021.

[27] J. Sun, L. Qiu, X. Liu, J. Zhang, J. Ma, and Y. Fang, "Optimal simultaneous pwm control for three- phase dual-active-bridge converters to minimize current stress in the whole load range," *IEEE Journal of Emerging and Selected Topics in Power Electronics*, vol. 9, pp. 5822–5837, 10 2021.

[28] Z. Li, Y. Wang, L. Shi, J. Huang, Y. Cui, and W. Lei, "Generalized averaging modeling and control strategy for three-phase dual-active-bridge dc-dc converters with three control variables," *Conference Proceedings - IEEE Applied Power Electronics Conference and Exposition - APEC*, pp. 1078–1084, 5 2017.

[29] N. S. M. Sharifuddin, N. M. L. Tan, and H. Akagi, "Evaluation of a three-phase bidirectional isolated dc-dc converter with varying transformer configurations using phase-shift modulation and burst-mode switching," *Energies*, vol. 13, p. 2836, 6 2020.

[30] N. H. Baars, J. Everts, C. G. Wijnands, and E. A. Lomonova, "Performance evaluation of a three-phase dual active bridge dc-dc converter with different transformer winding

configurations," *IEEE Transactions on Power Electronics*, vol. 31, pp. 6814–6823, 10 2016.

[31] L. M. Cunico and A. L. Kirsten, "Improved zvs range for three-phase dual-active-bridge converter with wye-extended-delta transformer," *IEEE Transactions on Industrial Electronics*, vol. 69, pp. 7984–7993, 8 2022.

[32] W. G. Hurley and W. H. Wölfle, "Transformers and inductors for power electronics: Theory, design and applications," *Transformers and Inductors for Power Electronics: Theory, Design and Applications*, 3 2013.

[33] M. Kasper, R. M. Burkart, G. Deboy, and J. W. Kolar, "Zvs of power mosfets revisited," *IEEE Transactions on Power Electronics*, vol. 31, pp. 8063–8067, 12 2016.

[34] D. Christen and J. Biela, "Analytical switching loss modeling based on datasheet parameters for mosfets in a half-bridge," *IEEE Transactions on Power Electronics*, vol. 34, pp. 3700–3710, 4 2019.

[35] CREE, "C2m0080120d silicon carbide power mosfet c2m tm mosfet technology," 2019. Available at `https://assets.wolfspeed.com/uploads/2020/12/C2M0080120D.pdf`.

[36] S. Taraborrelli, R. Spenke, and R. W. D. Doncker, "Bidirectional dual active bridge converter using a tap changer for extended voltage ranges," *2016 18th European Conference on Power Electronics and Applications, EPE 2016 ECCE Europe*, 10 2016.

[37] A. Jafari, M. S. Nikoo, F. Karakaya, and E. Matioli, "Enhanced dab for efficiency preservation using adjustable-tap high-frequency transformer," *IEEE Transactions on Power Electronics*, vol. 35, pp. 6673–6677, 7 2020.

[38] J. Kennedy and R. Eberhart, "Particle swarm optimization," pp. 1942–1948, IEEE.

[39] J. D. Pollock and C. R. Sullivan, "Design considerations for high-efficiency leakage transformers," *Conference Proceedings - IEEE Applied Power Electronics Conference and Exposition - APEC*, vol. 2015-May, pp. 162–169, 5 2015.

[40] J. Miüihlethaler, J. W. Kolar, and A. Ecklebe, "A novel approach for 3d air gap reluctance alculations," *8th International Conference on Power Electronics - ECCE Asia: "Green World with Power Electronics", ICPE 2011-ECCE Asia*, pp. 446–452, 2011.

[41] P. L. Dowell, "Effects of eddy currents in transformer windings," *Proceedings of the Institution of Electrical Engineers*, vol. 113, p. 1387, 1966.

[42] C. K. Leung, S. Baek, S. Dutta, and S. Bhattacharya, "Design considerations of high voltage and high frequency three phase transformer for solid state transformer application," *2010 IEEE Energy Conversion Congress and Exposition, ECCE 2010 - Proceedings*, pp. 1551–1558, 2010.

[43] L. Juarez, C. Branco, and C. Neto, "Sistema de conversão de energia eólica de alta eficiência utilizando o conversor delta tipo-t e minimização das perdas da máquina baseada em modelo," 2016.

[44] K. Peng, S. Eskandari, and E. Santi, "Characterization and modeling of sic mosfet body diode," *Conference Proceedings - IEEE Applied Power Electronics Conference and Exposition - APEC*, vol. 2016-May, pp. 2127–2135, 5 2016.

[45] S. Geng, M. Chu, W. Wang, P. Wan, X. Peng, H. Lu, and P. Li, "Modelling and optimization of winding resistance for litz wire inductors," *IET Power Electronics*, vol. 14, pp. 1834–1843, 8 2021.

[46] G. Xinchun, H. Yonghu, R. Yi, al, S. Kiyohara, M. Tsubaki, K. Liao, G. Zhang, J. Chen, and Y. Liu, "Comparative core loss calculation methods for magnetic materials under harmonics effect," *IOP Conference Series: Materials Science and Engineering*, vol. 486, p. 012019, 6 2019.

[47] M. X. C. Magnetics, "Datasheet 3c94 material specification," 2002. Available at `https://elnamagnetics.com/wp-content/uploads/library/Ferroxcube-Materials/3C94_Material_Specification.pdf`.

[48] T. Electronics, "Ferrites and accessories siferrit material n87," 2017. Available at `https://www.tdk-electronics.tdk.com/download/528882/990c299b916e9f3eb7e44ad563b7f0b9/pdf-n87.pdf`.

[49] M. J. Jacoboski, A. de Bastiani Lange, and M. L. Heldwein, "Closed-form solution for core loss calculation in single-phase bridgeless pfc rectifiers based on the igse method," *IEEE Transactions on Power Electronics*, vol. 33, pp. 4599–4604, 2018.

APPENDIX

A Basic Equations

In this appendix, the following equations are presented for all 3ϕ network configurations:

- I_o: Average output current;
- $i_{ld-a-rms}$: RMS current in the inductor;
- $i_{tr-a-rms}$: RMS current in the primary winding;
- $i_{tr-A-rms}$: RMS current in the secondary winding;
- $i_{sw-a-rms}$: RMS current in primary power switch;
- $i_{sw-A-rms}$: RMS current in secondary power switch;
- i_{sw-a}: Switching current in primary side;
- i_{sw-A}: Switching current in secondary side.

Only equations related to Region 1, from Figure 2.8, are presented.

Moreover, this work has developed several additional equations that are not presented here due to space constraints, including:

- $i_{ld-a,n}$: Inductor current in n^{th} harmonic;
- $i_{sw-a,n}$: Primary winding current in n^{th} harmonic;
- $i_{sw-A,n}$: Secondary winding current in n^{th} harmonic;
- P_{v-ind}: Inductor iGSE;
- P_{v-trs}: Transformer iGSE;
- $V_{t_{dt}-a}$: Voltage at end of dead-time in primary side;
- $V_{t_{dt}-A}$: Voltage at end of dead-time in secondary side.

A.1 YY 3ϕ NETWORK

$$I_o = \begin{cases} -\frac{M\,V_i\,\phi\,(3\,\phi-4\,\pi)}{12\,f_s\,\pi^2\,(L_2\,(L_1+L_{dab})-M^2)} & \text{if } 0^\circ \le \phi < 60^\circ \\ -\frac{M\,V_i\,\left(18\,\phi^2-18\,\pi\,\phi+\pi^2\right)}{36\,f_s\,\pi^2\,(L_2\,(L_1+L_{dab})-M^2)} & \text{if } 60^\circ \le \phi \le 90^\circ \end{cases}. \tag{A.1}$$

$$i_{ld-a-rms} = \begin{cases} \frac{\sqrt{3}\,V_i\,\sqrt{5\,\pi^3\,{L_2}^2-27\,L_2\,M\,d\,\phi^3+54\,\pi\,L_2\,M\,d\,\phi^2-10\,\pi^3\,L_2\,M\,d+5\,\pi^3\,M^2\,d^2}}{54\,f_s\,\pi^{3/2}\,|-M^2+L_1\,L_2+L_2\,L_{dab}|} & \text{if } 0^\circ \le \phi < 60^\circ \\ \frac{\sqrt{3}\,V_i\,\sqrt{5\,\pi^3\,{L_2}^2-54\,L_2\,M\,d\,\phi^3+81\,\pi\,L_2\,M\,d\,\phi^2-9\,\pi^2\,L_2\,M\,d\,\phi-9\,\pi^3\,L_2\,M\,d+5\,\pi^3\,M^2\,d^2}}{54\,f_s\,\pi^{3/2}\,|-M^2+L_1\,L_2+L_2\,L_{dab}|} & \text{if } 60^\circ \le \phi \le 90^\circ \end{cases}. \tag{A.2}$$

$$i_{tr-a-rms} = \begin{cases} \frac{\sqrt{3}\,V_i\,\sqrt{5\,\pi^3\,{L_2}^2-27\,L_2\,M\,d\,\phi^3+54\,\pi\,L_2\,M\,d\,\phi^2-10\,\pi^3\,L_2\,M\,d+5\,\pi^3\,M^2\,d^2}}{54\,f_s\,\pi^{3/2}\,|-M^2+L_1\,L_2+L_2\,L_{dab}|} & \text{if } 0^\circ \le \phi < 60^\circ \\ \frac{\sqrt{3}\,V_i\,\sqrt{5\,\pi^3\,{L_2}^2-54\,L_2\,M\,d\,\phi^3+81\,\pi\,L_2\,M\,d\,\phi^2-9\,\pi^2\,L_2\,M\,d\,\phi-9\,\pi^3\,L_2\,M\,d+5\,\pi^3\,M^2\,d^2}}{54\,f_s\,\pi^{3/2}\,|-M^2+L_1\,L_2+L_2\,L_{dab}|} & \text{if } 60^\circ \le \phi \le 90^\circ \end{cases}. \tag{A.3}$$

$$i_{tr-A-rms} = \begin{cases} \frac{\sqrt{3}\,V_i\,\sqrt{\begin{array}{l}5\,\pi^3\,{L_1}^2\,d^2+10\,\pi^3\,L_1\,L_{dab}\,d^2-27\,L_1\,M\,d\,\phi^3+54\,\pi\,L_1\,M\,d\,\phi^2\\ -10\,\pi^3\,L_1\,M\,d+5\,\pi^3\,{L_{dab}}^2\,d^2-27\,L_{dab}\,M\,d\,\phi^3+54\,\pi\,L_{dab}\,M\,d\,\phi^2\\ -10\,\pi^3\,L_{dab}\,M\,d+5\,\pi^3\,M^2\end{array}}}{54\,f_s\,\pi^{3/2}\,|-M^2+L_1\,L_2+L_2\,L_{dab}|} & \text{if } 0^\circ \le \phi < 60^\circ \\ \frac{\sqrt{3}\,V_i\,\sqrt{\begin{array}{l}5\,\pi^3\,{L_1}^2\,d^2+10\,\pi^3\,L_1\,L_{dab}\,d^2-54\,L_1\,M\,d\,\phi^3+81\,\pi\,L_1\,M\,d\,\phi^2\\ -9\,\pi^2\,L_1\,M\,d\,\phi-9\,\pi^3\,L_1\,M\,d+5\,\pi^3\,{L_{dab}}^2\,d^2-54\,L_{dab}\,M\,d\,\phi^3\\ +81\,\pi\,L_{dab}\,M\,d\,\phi^2-9\,\pi^2\,L_{dab}\,M\,d\,\phi-9\,\pi^3\,L_{dab}\,M\,d+5\,\pi^3\,M^2\end{array}}}{54\,f_s\,\pi^{3/2}\,|-M^2+L_1\,L_2+L_2\,L_{dab}|} & \text{if } 60^\circ \le \phi \le 90^\circ \end{cases}. \tag{A.4}$$

$$i_{sw-a-rms} = \begin{cases} \frac{\sqrt{6}\,V_i\,\sqrt{5\,\pi^3\,{L_2}^2 - 27\,L_2\,M\,d\,\phi^3 + 54\,\pi\,L_2\,M\,d\,\phi^2 - 10\,\pi^3\,L_2\,M\,d + 5\,\pi^3\,M^2\,d^2}}{108\,f_s\,\pi^{3/2}\,|-M^2 + L_1\,L_2 + L_2\,L_{dab}|} & \text{if } 0° \leq \phi < 60° \\ \frac{\sqrt{6}\,V_i\,\sqrt{5\,\pi^3\,{L_2}^2 - 54\,L_2\,M\,d\,\phi^3 + 81\,\pi\,L_2\,M\,d\,\phi^2 - 9\,\pi^2\,L_2\,M\,d\,\phi - 9\,\pi^3\,L_2\,M\,d + 5\,\pi^3\,M^2\,d^2}}{108\,f_s\,\pi^{3/2}\,|-M^2 + L_1\,L_2 + L_2\,L_{dab}|} & \text{if } 60° \leq \phi \leq 90° \end{cases} . \tag{A.5}$$

$$i_{sw-A-rms} = \begin{cases} \frac{\sqrt{6}\,V_i\,\sqrt{\begin{array}{l} 5\,\pi^3\,{L_1}^2\,d^2 + 10\,\pi^3\,L_1\,L_{dab}\,d^2 - 27\,L_1\,M\,d\,\phi^3 + 54\,\pi\,L_1\,M\,d\,\phi^2 \\ -10\,\pi^3\,L_1\,M\,d + 5\,\pi^3\,{L_{dab}}^2\,d^2 - 27\,L_{dab}\,M\,d\,\phi^3 + 54\,\pi\,L_{dab}\,M\,d\,\phi^2 \\ -10\,\pi^3\,L_{dab}\,M\,d + 5\,\pi^3\,M^2 \end{array}}}{108\,f_s\,\pi^{3/2}\,|-M^2 + L_1\,L_2 + L_2\,L_{dab}|} & \text{if } 0° \leq \phi < 60° \\ \frac{\sqrt{6}\,V_i\,\sqrt{\begin{array}{l} 5\,\pi^3\,{L_1}^2\,d^2 + 10\,\pi^3\,L_1\,L_{dab}\,d^2 - 54\,L_1\,M\,d\,\phi^3 + 81\,\pi\,L_1\,M\,d\,\phi^2 \\ -9\,\pi^2\,L_1\,M\,d\,\phi - 9\,\pi^3\,L_1\,M\,d + 5\,\pi^3\,{L_{dab}}^2\,d^2 - 54\,L_{dab}\,M\,d\,\phi^3 \\ +81\,\pi\,L_{dab}\,M\,d\,\phi^2 - 9\,\pi^2\,L_{dab}\,M\,d\,\phi - 9\,\pi^3\,L_{dab}\,M\,d + 5\,\pi^3\,M^2 \end{array}}}{108\,f_s\,\pi^{3/2}\,|-M^2 + L_1\,L_2 + L_2\,L_{dab}|} & \text{if } 60° \leq \phi \leq 90° \end{cases} . \tag{A.6}$$

$$i_{sw-a} = \begin{cases} -\frac{2\pi\,L_2\,V_i - M\,V_i\,(2\,\pi\,d - 3\,d\,\phi)}{18 f_s\,\pi\,(-M^2 + L_1\,L_2 + L_2\,L_{dab})} & \text{if } 0° \leq \phi < 60° \\ -\frac{2\pi\,L_2\,V_i - M\,V_i\,(3\,\pi\,d - 6\,d\,\phi)}{18 f_s\,\pi\,(-M^2 + L_1\,L_2 + L_2\,L_{dab})} & \text{if } 60° \leq \phi \leq 90° \end{cases} . \tag{A.7}$$

$$i_{sw-A} = \begin{cases} \frac{V_i\,(2\,\pi\,L_1\,d + 2\,\pi\,L_{dab}\,d) + M\,V_i\,(3\,\phi - 2\,\pi)}{18 f_s\,\pi\,(-M^2 + L_1\,L_2 + L_2\,L_{dab})} & \text{if } 0° \leq \phi < 60° \\ \frac{V_i\,(2\,\pi\,L_1\,d + 2\,\pi\,L_{dab}\,d) + M\,V_i\,(6\,\phi - 3\,\pi)}{18 f_s\,\pi\,(-M^2 + L_1\,L_2 + L_2\,L_{dab})} & \text{if } 60° \leq \phi \leq 90° \end{cases} . \tag{A.8}$$

A.2 YD 3ϕ NETWORK

$$I_o = \begin{cases} \frac{M\,V_i\,(6\,\phi-\pi)}{12\,f_s\,\pi\,(L_2\,(L_1+L_{dab})-M^2)} & \text{if } 30^\circ \leq \phi < 60^\circ \\ -\frac{M\,V_i\left(9\,\phi^2-12\,\pi\,\phi+2\,\pi^2\right)}{12\,f_s\,\pi^2\,(L_2\,(L_1+L_{dab})-M^2)} & \text{if } 60^\circ \leq \phi \leq 120^\circ \end{cases}. \tag{A.9}$$

$$i_{ld-a-rms} = \begin{cases} \frac{\sqrt{3}\,V_i\,\sqrt{5\,\pi^2\,{L_2}^2+81\,L_2\,M\,d\,\phi^2-27\,\pi\,L_2\,M\,d\,\phi-15\,\pi^2\,L_2\,M\,d+15\,\pi^2\,M^2\,d^2}}{54\,f_s\,\pi\,|-M^2+L_1\,L_2+L_2\,L_{dab}|} & \text{if } 30^\circ \leq \phi < 60^\circ \\ \frac{\sqrt{3}\,V_i\,\sqrt{5\,\pi^3\,{L_2}^2-81\,L_2\,M\,d\,\phi^3+162\,\pi\,L_2\,M\,d\,\phi^2-54\,\pi^2\,L_2\,M\,d\,\phi-12\,\pi^3\,L_2\,M\,d+15\,\pi^3\,M^2\,d^2}}{54\,f_s\,\pi^{3/2}\,|-M^2+L_1\,L_2+L_2\,L_{dab}|} & \text{if } 60^\circ \leq \phi \leq 120^\circ \end{cases}. \tag{A.10}$$

$$i_{tr-a-rms} = \begin{cases} \frac{\sqrt{3}\,V_i\,\sqrt{5\,\pi^2\,{L_2}^2+81\,L_2\,M\,d\,\phi^2-27\,\pi\,L_2\,M\,d\,\phi-15\,\pi^2\,L_2\,M\,d+15\,\pi^2\,M^2\,d^2}}{54\,f_s\,\pi\,|-M^2+L_1\,L_2+L_2\,L_{dab}|} & \text{if } 30^\circ \leq \phi < 60^\circ \\ \frac{\sqrt{3}\,V_i\,\sqrt{5\,\pi^3\,{L_2}^2-81\,L_2\,M\,d\,\phi^3+162\,\pi\,L_2\,M\,d\,\phi^2-54\,\pi^2\,L_2\,M\,d\,\phi-12\,\pi^3\,L_2\,M\,d+15\,\pi^3\,M^2\,d^2}}{54\,f_s\,\pi^{3/2}\,|-M^2+L_1\,L_2+L_2\,L_{dab}|} & \text{if } 60^\circ \leq \phi \leq 120^\circ \end{cases}. \tag{A.11}$$

$$i_{tr-A-rms} = \begin{cases} \frac{\sqrt{3}\,V_i\,\sqrt{\begin{array}{l}15\,\pi^2\,{L_1}^2\,d^2+30\,\pi^2\,L_1\,L_{dab}\,d^2+81\,L_1\,M\,d\,\phi^2-27\,\pi\,L_1\,M\,d\,\phi \\ -15\,\pi^2\,L_1\,M\,d+15\,\pi^2\,{L_{dab}}^2\,d^2+81\,L_{dab}\,M\,d\,\phi^2-27\,\pi\,L_{dab}\,M\,d\,\phi \\ -15\,\pi^2\,L_{dab}\,M\,d+5\,\pi^2\,M^2\end{array}}}{54\,f_s\,\pi\,|-M^2+L_1\,L_2+L_2\,L_{dab}|} & \text{if } 30^\circ \leq \phi < 60^\circ \\ \frac{\sqrt{3}\,V_i\,\sqrt{\begin{array}{l}15\,\pi^3\,{L_1}^2\,d^2+30\,\pi^3\,L_1\,L_{dab}\,d^2-81\,L_1\,M\,d\,\phi^3+162\,\pi\,L_1\,M\,d\,\phi^2 \\ -54\,\pi^2\,L_1\,M\,d\,\phi-12\,\pi^3\,L_1\,M\,d+15\,\pi^3\,{L_{dab}}^2\,d^2-81\,L_{dab}\,M\,d\,\phi^3 \\ +162\,\pi\,L_{dab}\,M\,d\,\phi^2-54\,\pi^2\,L_{dab}\,M\,d\,\phi-12\,\pi^3\,L_{dab}\,M\,d+5\,\pi^3\,M^2\end{array}}}{54\,f_s\,\pi^{3/2}\,|-M^2+L_1\,L_2+L_2\,L_{dab}|} & \text{if } 60^\circ \leq \phi \leq 120^\circ \end{cases}. \tag{A.12}$$

$$i_{sw-a-rms} = \begin{cases} \frac{\sqrt{6}\,V_i\,\sqrt{5\,\pi^2\,{L_2}^2+81\,L_2\,M\,d\,\phi^2-27\,\pi\,L_2\,M\,d\,\phi-15\,\pi^2\,L_2\,M\,d+15\,\pi^2\,M^2\,d^2}}{108\,f_s\,\pi\,|-M^2+L_1\,L_2+L_2\,L_{dab}|} & \text{if } 30^\circ \leq \phi < 60^\circ \\ \frac{\sqrt{6}\,V_i\,\sqrt{5\,\pi^3\,{L_2}^2-81\,L_2\,M\,d\,\phi^3+162\,\pi\,L_2\,M\,d\,\phi^2-54\,\pi^2\,L_2\,M\,d\,\phi-12\,\pi^3\,L_2\,M\,d+15\,\pi^3\,M^2\,d^2}}{108\,f_s\,\pi^{3/2}\,|-M^2+L_1\,L_2+L_2\,L_{dab}|} & \text{if } 60^\circ \leq \phi \leq 120^\circ \end{cases} . \tag{A.13}$$

$$i_{sw-A-rms} = \begin{cases} \frac{\sqrt{2}\,V_i\,\sqrt{\begin{array}{l}15\,\pi^2\,{L_1}^2\,d^2+30\,\pi^2\,L_1\,L_{dab}\,d^2+81\,L_1\,M\,d\,\phi^2\\ -27\,\pi\,L_1\,M\,d\,\phi-15\,\pi^2\,L_1\,M\,d+15\,\pi^2\,{L_{dab}}^2\,d^2\\ +81\,L_{dab}\,M\,d\,\phi^2-27\,\pi\,L_{dab}\,M\,d\,\phi-15\,\pi^2\,L_{dab}\,M\,d+5\,\pi^2\,M^2\end{array}}}{36\,f_s\,\pi\,|-M^2+L_1\,L_2+L_2\,L_{dab}|} & \text{if } 30^\circ \leq \phi < 60^\circ \\ \frac{\sqrt{2}\,V_i\,\sqrt{\begin{array}{l}15\,\pi^3\,{L_1}^2\,d^2+30\,\pi^3\,L_1\,L_{dab}\,d^2-81\,L_1\,M\,d\,\phi^3+162\,\pi\,L_1\,M\,d\,\phi^2\\ -54\,\pi^2\,L_1\,M\,d\,\phi-12\,\pi^3\,L_1\,M\,d+15\,\pi^3\,{L_{dab}}^2\,d^2-81\,L_{dab}\,M\,d\,\phi^3\\ +162\,\pi\,L_{dab}\,M\,d\,\phi^2-54\,\pi^2\,L_{dab}\,M\,d\,\phi-12\,\pi^3\,L_{dab}\,M\,d+5\,\pi^3\,M^2\end{array}}}{36\,f_s\,\pi^{3/2}\,|-M^2+L_1\,L_2+L_2\,L_{dab}|} & \text{if } 60^\circ \leq \phi \leq 120^\circ \end{cases} . \tag{A.14}$$

$$i_{sw-a} = \begin{cases} -\frac{V_i\,(2\,L_2-3\,M\,d)}{18\,f_s\,(-M^2+L_1\,L_2+L_2\,L_{dab})} & \text{if } 30^\circ \leq \phi < 60^\circ \\ -\frac{2\pi\,L_2\,V_i-M\,V_i\,(6\,\pi\,d-9\,d\,\phi)}{18 f_s\,\pi\,(-M^2+L_1\,L_2+L_2\,L_{dab})} & \text{if } 60^\circ \leq \phi \leq 120^\circ \end{cases} . \tag{A.15}$$

$$i_{sw-A} = \begin{cases} \frac{V_i\,(2\,L_1\,d-M+2\,L_{dab}\,d)}{6\,f_s\,(L_2\,(L_1+L_{dab})-M^2)} & \text{if } 30^\circ \leq \phi < 60^\circ \\ \frac{V_i\,(2\,\pi\,L_1\,d+2\,\pi\,L_{dab}\,d)+M\,V_i\,(3\,\phi-2\,\pi)}{6 f_s\,\pi\,(-M^2+L_1\,L_2+L_2\,L_{dab})} & \text{if } 60^\circ \leq \phi \leq 120^\circ \end{cases} . \tag{A.16}$$

A.3 ODY 3ϕ NETWORK

$$I_o = \begin{cases} \frac{M\,V_i\,(6\,\phi+\pi)}{12\,f_s\,\pi\,(L_2\,(L_1+3\,L_{dab})-M^2)} & \text{if } -30^\circ \le \phi < 0^\circ \\ \frac{M\,V_i\left(-9\,\phi^2+6\,\pi\,\phi+\pi^2\right)}{12\,f_s\,\pi^2\,(L_2\,(L_1+3\,L_{dab})-M^2)} & \text{if } 0^\circ \le \phi \le 60^\circ \end{cases}. \tag{A.17}$$

$$i_{ld-a-rms} = \begin{cases} \frac{V_i\,\sqrt{15\,\pi^2\,{L_2}^2+81\,L_2\,M\,d\,\phi^2+27\,\pi\,L_2\,M\,d\,\phi-15\,\pi^2\,L_2\,M\,d+5\,\pi^2\,M^2\,d^2}}{18\,f_s\,\pi\,|-M^2+L_1\,L_2+3\,L_2\,L_{dab}|} & \text{if } -30^\circ \le \phi < 0^\circ \\ \frac{V_i\,\sqrt{15\,\pi^3\,{L_2}^2-81\,L_2\,M\,d\,\phi^3+81\,\pi\,L_2\,M\,d\,\phi^2+27\,\pi^2\,L_2\,M\,d\,\phi-15\,\pi^3\,L_2\,M\,d+5\,\pi^3\,M^2\,d^2}}{18\,f_s\,\pi^{3/2}\,|-M^2+L_1\,L_2+3\,L_2\,L_{dab}|} & \text{if } 0^\circ \le \phi \le 60^\circ \end{cases}. \tag{A.18}$$

$$i_{tr-a-rms} = \begin{cases} \frac{\sqrt{3}\,V_i\,\sqrt{15\,\pi^2\,{L_2}^2+81\,L_2\,M\,d\,\phi^2+27\,\pi\,L_2\,M\,d\,\phi-15\,\pi^2\,L_2\,M\,d+5\,\pi^2\,M^2\,d^2}}{54\,f_s\,\pi\,|-M^2+L_1\,L_2+3\,L_2\,L_{dab}|} & \text{if } -30^\circ \le \phi < 0^\circ \\ \frac{\sqrt{3}\,V_i\,\sqrt{15\,\pi^3\,{L_2}^2-81\,L_2\,M\,d\,\phi^3+81\,\pi\,L_2\,M\,d\,\phi^2+27\,\pi^2\,L_2\,M\,d\,\phi-15\,\pi^3\,L_2\,M\,d+5\,\pi^3\,M^2\,d^2}}{54\,f_s\,\pi^{3/2}\,|-M^2+L_1\,L_2+3\,L_2\,L_{dab}|} & \text{if } 0^\circ \le \phi \le 60^\circ \end{cases}. \tag{A.19}$$

$$i_{tr-A-rms} = \begin{cases} \frac{\sqrt{3}\,V_i\,\sqrt{\begin{array}{l}5\,\pi^2\,{L_1}^2\,d^2+30\,\pi^2\,L_1\,L_{dab}\,d^2+81\,L_1\,M\,d\,\phi^2+27\,\pi\,L_1\,M\,d\,\phi-15\,\pi^2\,L_1\,M\,d\\+45\,\pi^2\,{L_{dab}}^2\,d^2+243\,L_{dab}\,M\,d\,\phi^2+81\,\pi\,L_{dab}\,M\,d\,\phi-45\,\pi^2\,L_{dab}\,M\,d+15\,\pi^2\,M^2\end{array}}}{54\,f_s\,\pi\,|-M^2+L_1\,L_2+3\,L_2\,L_{dab}|} & \text{if } -30^\circ \le \phi < 0^\circ \\ \frac{\sqrt{3}\,V_i\,\sqrt{\begin{array}{l}5\,\pi^3\,{L_1}^2\,d^2+30\,\pi^3\,L_1\,L_{dab}\,d^2-81\,L_1\,M\,d\,\phi^3+81\,\pi\,L_1\,M\,d\,\phi^2\\+27\,\pi^2\,L_1\,M\,d\,\phi-15\,\pi^3\,L_1\,M\,d+45\,\pi^3\,{L_{dab}}^2\,d^2-243\,L_{dab}\,M\,d\,\phi^3\\+243\,\pi\,L_{dab}\,M\,d\,\phi^2+81\,\pi^2\,L_{dab}\,M\,d\,\phi-45\,\pi^3\,L_{dab}\,M\,d+15\,\pi^3\,M^2\end{array}}}{54\,f_s\,\pi^{3/2}\,|-M^2+L_1\,L_2+3\,L_2\,L_{dab}|} & \text{if } 0^\circ \le \phi \le 60^\circ \end{cases}. \tag{A.20}$$

$$i_{sw-a-rms} = \begin{cases} \frac{\sqrt{2}\,V_i\,\sqrt{15\,\pi^2\,{L_2}^2+81\,L_2\,M\,d\,\phi^2+27\,\pi\,L_2\,M\,d\,\phi-15\,\pi^2\,L_2\,M\,d+5\,\pi^2\,M^2\,d^2}}{36\,f_s\,\pi\,|-M^2+L_1\,L_2+3\,L_2\,L_{dab}|} & \text{if } -30^\circ \le \phi < 0^\circ \\ \frac{\sqrt{2}\,V_i\,\sqrt{15\,\pi^3\,{L_2}^2-81\,L_2\,M\,d\,\phi^3+81\,\pi\,L_2\,M\,d\,\phi^2+27\,\pi^2\,L_2\,M\,d\,\phi-15\,\pi^3\,L_2\,M\,d+5\,\pi^3\,M^2\,d^2}}{36\,f_s\,\pi^{3/2}\,|-M^2+L_1\,L_2+3\,L_2\,L_{dab}|} & \text{if } 0^\circ \le \phi \le 60^\circ \end{cases}. \tag{A.21}$$

$$i_{sw-A-rms} = \begin{cases} \dfrac{\sqrt{6}\,V_i \sqrt{\begin{array}{l} 5\,\pi^2\,{L_1}^2\,d^2 + 30\,\pi^2\,L_1\,L_{dab}\,d^2 + 81\,L_1\,M\,d\,\phi^2 + 27\,\pi\,L_1\,M\,d\,\phi - 15\,\pi^2\,L_1\,M\,d \\ +45\,\pi^2\,{L_{dab}}^2\,d^2 + 243\,L_{dab}\,M\,d\,\phi^2 + 81\,\pi\,L_{dab}\,M\,d\,\phi - 45\,\pi^2\,L_{dab}\,M\,d + 15\,\pi^2\,M^2 \end{array}}}{108\,f_s\,\pi\,\left|-M^2+L_1\,L_2+3\,L_2\,L_{dab}\right|} & \text{if } -30^\circ \le \phi < 0^\circ \\ \dfrac{\sqrt{6}\,V_i \sqrt{\begin{array}{l} 5\,\pi^3\,{L_1}^2\,d^2 + 30\,\pi^3\,L_1\,L_{dab}\,d^2 - 81\,L_1\,M\,d\,\phi^3 + 81\,\pi\,L_1\,M\,d\,\phi^2 \\ +27\,\pi^2\,L_1\,M\,d\,\phi - 15\,\pi^3\,L_1\,M\,d + 45\,\pi^3\,{L_{dab}}^2\,d^2 - 243\,L_{dab}\,M\,d\,\phi^3 \\ +243\,\pi\,L_{dab}\,M\,d\,\phi^2 + 81\,\pi^2\,L_{dab}\,M\,d\,\phi - 45\,\pi^3\,L_{dab}\,M\,d + 15\,\pi^3\,M^2 \end{array}}}{108\,f_s\,\pi^{3/2}\,\left|-M^2+L_1\,L_2+3\,L_2\,L_{dab}\right|} & \text{if } 0^\circ \le \phi \le 60^\circ \end{cases} . \tag{A.22}$$

$$i_{sw-a} = \begin{cases} -\frac{V_i\,(2\,L_2 - M\,d)}{6\,f_s\,(-M^2+L_1\,L_2+3\,L_2\,L_{dab})} & \text{if } -30^\circ \le \phi < 0^\circ \\ -\frac{2\pi\,L_2\,V_i - M\,V_i\,(\pi\,d - 3\,d\,\phi)}{6 f_s\,\pi\,(-M^2+L_1\,L_2+3\,L_2\,L_{dab})} & \text{if } 0^\circ \le \phi \le 60^\circ \end{cases} . \tag{A.23}$$

$$i_{sw-A} = \begin{cases} \frac{V_i\,(2\,L_1\,d - 3\,M + 6\,L_{dab}\,d)}{18\,f_s\,(L_2\,(L_1+3\,L_{dab}) - M^2)} & \text{if } -30^\circ \le \phi < 0^\circ \\ \frac{V_i\,(2\,\pi\,L_1\,d + 6\,\pi\,L_{dab}\,d) + M\,V_i\,(9\,\phi - 3\,\pi)}{18 f_s\,\pi\,(-M^2+L_1\,L_2+3\,L_2\,L_{dab})} & \text{if } 0^\circ \le \phi \le 60^\circ \end{cases} . \tag{A.24}$$

A.4 ODD 3ϕ NETWORK

$$I_o = \begin{cases} -\frac{M\,V_i\,\phi\,(3\,\phi - 4\,\pi)}{4\,f_s\,\pi^2\,(L_2\,(L_1+3\,L_{dab}) - M^2)} & \text{if } 0^\circ \le \phi < 60^\circ \\ -\frac{M\,V_i\left(18\,\phi^2 - 18\,\pi\,\phi + \pi^2\right)}{12\,f_s\,\pi^2\,(L_2\,(L_1+3\,L_{dab}) - M^2)} & \text{if } 60^\circ \le \phi \le 90^\circ \end{cases} . \tag{A.25}$$

$$i_{ld-a-rms} = \begin{cases} \frac{\sqrt{3}\,V_i\,\sqrt{5\,\pi^3\,{L_2}^2 - 27\,L_2\,M\,d\,\phi^3 + 54\,\pi\,L_2\,M\,d\,\phi^2 - 10\,\pi^3\,L_2\,M\,d + 5\,\pi^3\,M^2\,d^2}}{18\,f_s\,\pi^{3/2}\,|-M^2 + L_1\,L_2 + 3\,L_2\,L_{dab}|} & \text{if } 0° \leq \phi < 60° \\ \frac{\sqrt{3}\,V_i\,\sqrt{5\,\pi^3\,{L_2}^2 - 54\,L_2\,M\,d\,\phi^3 + 81\,\pi\,L_2\,M\,d\,\phi^2 - 9\,\pi^2\,L_2\,M\,d\,\phi - 9\,\pi^3\,L_2\,M\,d + 5\,\pi^3\,M^2\,d^2}}{18\,f_s\,\pi^{3/2}\,|-M^2 + L_1\,L_2 + 3\,L_2\,L_{dab}|} & \text{if } 60° \leq \phi \leq 90° \end{cases} . \tag{A.26}$$

$$i_{tr-a-rms} = \begin{cases} \frac{V_i\,\sqrt{5\,\pi^3\,{L_2}^2 - 27\,L_2\,M\,d\,\phi^3 + 54\,\pi\,L_2\,M\,d\,\phi^2 - 10\,\pi^3\,L_2\,M\,d + 5\,\pi^3\,M^2\,d^2}}{18\,f_s\,\pi^{3/2}\,|-M^2 + L_1\,L_2 + 3\,L_2\,L_{dab}|} & \text{if } 0° \leq \phi < 60° \\ \frac{V_i\,\sqrt{5\,\pi^3\,{L_2}^2 - 54\,L_2\,M\,d\,\phi^3 + 81\,\pi\,L_2\,M\,d\,\phi^2 - 9\,\pi^2\,L_2\,M\,d\,\phi - 9\,\pi^3\,L_2\,M\,d + 5\,\pi^3\,M^2\,d^2}}{18\,f_s\,\pi^{3/2}\,|-M^2 + L_1\,L_2 + 3\,L_2\,L_{dab}|} & \text{if } 60° \leq \phi \leq 90° \end{cases} . \tag{A.27}$$

$$i_{tr-A-rms} = \begin{cases} \frac{V_i\,\sqrt{\begin{array}{l} 5\,\pi^3\,{L_1}^2\,d^2 + 30\,\pi^3\,L_1\,L_{dab}\,d^2 - 27\,L_1\,M\,d\,\phi^3 + 54\,\pi\,L_1\,M\,d\,\phi^2 - 10\,\pi^3\,L_1\,M\,d \\ +45\,\pi^3\,{L_{dab}}^2\,d^2 - 81\,L_{dab}\,M\,d\,\phi^3 + 162\,\pi\,L_{dab}\,M\,d\,\phi^2 - 30\,\pi^3\,L_{dab}\,M\,d + 5\,\pi^3\,M^2 \end{array}}}{18\,f_s\,\pi^{3/2}\,|-M^2 + L_1\,L_2 + 3\,L_2\,L_{dab}|} & \text{if } 0° \leq \phi < 60° \\ \frac{V_i\,\sqrt{\begin{array}{l} 5\,\pi^3\,{L_1}^2\,d^2 + 30\,\pi^3\,L_1\,L_{dab}\,d^2 - 54\,L_1\,M\,d\,\phi^3 + 81\,\pi\,L_1\,M\,d\,\phi^2 \\ -9\,\pi^2\,L_1\,M\,d\,\phi - 9\,\pi^3\,L_1\,M\,d + 45\,\pi^3\,{L_{dab}}^2\,d^2 - 162\,L_{dab}\,M\,d\,\phi^3 \\ +243\,\pi\,L_{dab}\,M\,d\,\phi^2 - 27\,\pi^2\,L_{dab}\,M\,d\,\phi - 27\,\pi^3\,L_{dab}\,M\,d + 5\,\pi^3\,M^2 \end{array}}}{18\,f_s\,\pi^{3/2}\,|-M^2 + L_1\,L_2 + 3\,L_2\,L_{dab}|} & \text{if } 60° \leq \phi \leq 90° \end{cases} . \tag{A.28}$$

$$i_{sw-a-rms} = \begin{cases} \frac{\sqrt{6}\,V_i\,\sqrt{5\,\pi^3\,{L_2}^2 - 27\,L_2\,M\,d\,\phi^3 + 54\,\pi\,L_2\,M\,d\,\phi^2 - 10\,\pi^3\,L_2\,M\,d + 5\,\pi^3\,M^2\,d^2}}{36\,f_s\,\pi^{3/2}\,|-M^2 + L_1\,L_2 + 3\,L_2\,L_{dab}|} & \text{if } 0° \leq \phi < 60° \\ \frac{\sqrt{6}\,V_i\,\sqrt{5\,\pi^3\,{L_2}^2 - 54\,L_2\,M\,d\,\phi^3 + 81\,\pi\,L_2\,M\,d\,\phi^2 - 9\,\pi^2\,L_2\,M\,d\,\phi - 9\,\pi^3\,L_2\,M\,d + 5\,\pi^3\,M^2\,d^2}}{36\,f_s\,\pi^{3/2}\,|-M^2 + L_1\,L_2 + 3\,L_2\,L_{dab}|} & \text{if } 60° \leq \phi \leq 90° \end{cases} . \tag{A.29}$$

$$i_{sw-A-rms} = \begin{cases} \frac{\sqrt{6}\,V_i \sqrt{\begin{array}{l} 5\,\pi^3\,{L_1}^2\,d^2 + 30\,\pi^3\,L_1\,L_{dab}\,d^2 - 27\,L_1\,M\,d\,\phi^3 + 54\,\pi\,L_1\,M\,d\,\phi^2 - 10\,\pi^3\,L_1\,M\,d \\ +45\,\pi^3\,{L_{dab}}^2\,d^2 - 81\,L_{dab}\,M\,d\,\phi^3 + 162\,\pi\,L_{dab}\,M\,d\,\phi^2 - 30\,\pi^3\,L_{dab}\,M\,d + 5\,\pi^3\,M^2 \end{array}}}{36\,f_s\,\pi^{3/2}\,\left|-M^2+L_1\,L_2+3\,L_2\,L_{dab}\right|} & \text{if } 0° \leq \phi < 60° \\ \frac{\sqrt{6}\,V_i \sqrt{\begin{array}{l} 5\,\pi^3\,{L_1}^2\,d^2 + 30\,\pi^3\,L_1\,L_{dab}\,d^2 - 54\,L_1\,M\,d\,\phi^3 + 81\,\pi\,L_1\,M\,d\,\phi^2 \\ -9\,\pi^2\,L_1\,M\,d\,\phi - 9\,\pi^3\,L_1\,M\,d + 45\,\pi^3\,{L_{dab}}^2\,d^2 - 162\,L_{dab}\,M\,d\,\phi^3 \\ +243\,\pi\,L_{dab}\,M\,d\,\phi^2 - 27\,\pi^2\,L_{dab}\,M\,d\,\phi - 27\,\pi^3\,L_{dab}\,M\,d + 5\,\pi^3\,M^2 \end{array}}}{36\,f_s\,\pi^{3/2}\,\left|-M^2+L_1\,L_2+3\,L_2\,L_{dab}\right|} & \text{if } 60° \leq \phi \leq 90° \end{cases} . \tag{A.30}$$

$$i_{sw-a} = \begin{cases} -\frac{2\pi\,L_2\,V_i - M\,V_i\,(2\,\pi\,d - 3\,d\,\phi)}{6 f_s\,\pi\,(-M^2+L_1\,L_2+3\,L_2\,L_{dab})} & \text{if } 0° \leq \phi < 60° \\ -\frac{2\pi\,L_2\,V_i - M\,V_i\,(3\,\pi\,d - 6\,d\,\phi)}{6 f_s\,\pi\,(-M^2+L_1\,L_2+3\,L_2\,L_{dab})} & \text{if } 60° \leq \phi \leq 90° \end{cases} . \tag{A.31}$$

$$i_{sw-A} = \begin{cases} \frac{V_i\,(2\,\pi\,L_1\,d + 6\,\pi\,L_{dab}\,d) + M\,V_i\,(3\,\phi - 2\,\pi)}{6 f_s\,\pi\,(-M^2+L_1\,L_2+3\,L_2\,L_{dab})} & \text{if } 0° \leq \phi < 60° \\ \frac{V_i\,(2\,\pi\,L_1\,d + 6\,\pi\,L_{dab}\,d) + M\,V_i\,(6\,\phi - 3\,\pi)}{6 f_s\,\pi\,(-M^2+L_1\,L_2+3\,L_2\,L_{dab})} & \text{if } 60° \leq \phi \leq 90° \end{cases} . \tag{A.32}$$

A.5 IDY 3ϕ NETWORK

$$I_o = \begin{cases} \frac{M\,V_i\,(6\,\phi + \pi)}{12\,f_s\,\pi\,(L_2\,(L_1 + L_{dab}) - M^2)} & \text{if } -30° \leq \phi < 0° \\ \frac{M\,V_i\left(-9\,\phi^2 + 6\,\pi\,\phi + \pi^2\right)}{12\,f_s\,\pi^2\,(L_2\,(L_1 + L_{dab}) - M^2)} & \text{if } 0° \leq \phi \leq 60° \end{cases} . \tag{A.33}$$

$$i_{ld-a-rms} = \begin{cases} \frac{\sqrt{3}\,V_i\,\sqrt{15\,\pi^2\,{L_2}^2+81\,L_2\,M\,d\,\phi^2+27\,\pi\,L_2\,M\,d\,\phi-15\,\pi^2\,L_2\,M\,d+5\,\pi^2\,M^2\,d^2}}{54\,f_s\,\pi\,|-M^2+L_1\,L_2+L_2\,L_{dab}|} & \text{if } -30^\circ \leq \phi < 0^\circ \\ \frac{\sqrt{3}\,V_i\,\sqrt{15\,\pi^3\,{L_2}^2-81\,L_2\,M\,d\,\phi^3+81\,\pi\,L_2\,M\,d\,\phi^2+27\,\pi^2\,L_2\,M\,d\,\phi-15\,\pi^3\,L_2\,M\,d+5\,\pi^3\,M^2\,d^2}}{54\,f_s\,\pi^{3/2}\,|-M^2+L_1\,L_2+L_2\,L_{dab}|} & \text{if } 0^\circ \leq \phi \leq 60^\circ \end{cases} . \tag{A.34}$$

$$i_{tr-a-rms} = \begin{cases} \frac{\sqrt{3}\,V_i\,\sqrt{15\,\pi^2\,{L_2}^2+81\,L_2\,M\,d\,\phi^2+27\,\pi\,L_2\,M\,d\,\phi-15\,\pi^2\,L_2\,M\,d+5\,\pi^2\,M^2\,d^2}}{54\,f_s\,\pi\,|-M^2+L_1\,L_2+L_2\,L_{dab}|} & \text{if } -30^\circ \leq \phi < 0^\circ \\ \frac{\sqrt{3}\,V_i\,\sqrt{15\,\pi^3\,{L_2}^2-81\,L_2\,M\,d\,\phi^3+81\,\pi\,L_2\,M\,d\,\phi^2+27\,\pi^2\,L_2\,M\,d\,\phi-15\,\pi^3\,L_2\,M\,d+5\,\pi^3\,M^2\,d^2}}{54\,f_s\,\pi^{3/2}\,|-M^2+L_1\,L_2+L_2\,L_{dab}|} & \text{if } 0^\circ \leq \phi \leq 60^\circ \end{cases} . \tag{A.35}$$

$$i_{tr-A-rms} = \begin{cases} \frac{\sqrt{3}\,V_i\,\sqrt{\begin{array}{l}5\,\pi^2\,{L_1}^2\,d^2+10\,\pi^2\,L_1\,L_{dab}\,d^2+81\,L_1\,M\,d\,\phi^2+27\,\pi\,L_1\,M\,d\,\phi-15\,\pi^2\,L_1\,M\,d\\+5\,\pi^2\,{L_{dab}}^2\,d^2+81\,L_{dab}\,M\,d\,\phi^2+27\,\pi\,L_{dab}\,M\,d\,\phi-15\,\pi^2\,L_{dab}\,M\,d+15\,\pi^2\,M^2\end{array}}}{54\,f_s\,\pi\,|-M^2+L_1\,L_2+L_2\,L_{dab}|} & \text{if } -30^\circ \leq \phi < 0^\circ \\ \frac{\sqrt{3}\,V_i\,\sqrt{\begin{array}{l}5\,\pi^3\,{L_1}^2\,d^2+10\,\pi^3\,L_1\,L_{dab}\,d^2-81\,L_1\,M\,d\,\phi^3+81\,\pi\,L_1\,M\,d\,\phi^2\\+27\,\pi^2\,L_1\,M\,d\,\phi-15\,\pi^3\,L_1\,M\,d+5\,\pi^3\,{L_{dab}}^2\,d^2-81\,L_{dab}\,M\,d\,\phi^3\\+81\,\pi\,L_{dab}\,M\,d\,\phi^2+27\,\pi^2\,L_{dab}\,M\,d\,\phi-15\,\pi^3\,L_{dab}\,M\,d+15\,\pi^3\,M^2\end{array}}}{54\,f_s\,\pi^{3/2}\,|-M^2+L_1\,L_2+L_2\,L_{dab}|} & \text{if } 0^\circ \leq \phi \leq 60^\circ \end{cases} . \tag{A.36}$$

$$i_{sw-a-rms} = \begin{cases} \frac{\sqrt{2}\,V_i\,\sqrt{15\,\pi^2\,{L_2}^2+81\,L_2\,M\,d\,\phi^2+27\,\pi\,L_2\,M\,d\,\phi-15\,\pi^2\,L_2\,M\,d+5\,\pi^2\,M^2\,d^2}}{36\,f_s\,\pi\,|-M^2+L_1\,L_2+L_2\,L_{dab}|} & \text{if } -30^\circ \leq \phi < 0^\circ \\ \frac{\sqrt{2}\,V_i\,\sqrt{15\,\pi^3\,{L_2}^2-81\,L_2\,M\,d\,\phi^3+81\,\pi\,L_2\,M\,d\,\phi^2+27\,\pi^2\,L_2\,M\,d\,\phi-15\,\pi^3\,L_2\,M\,d+5\,\pi^3\,M^2\,d^2}}{36\,f_s\,\pi^{3/2}\,|-M^2+L_1\,L_2+L_2\,L_{dab}|} & \text{if } 0^\circ \leq \phi \leq 60^\circ \end{cases} . \tag{A.37}$$

$$i_{sw-A-rms} = \begin{cases} \frac{\sqrt{6}\,V_i \sqrt{\begin{array}{l} 5\,\pi^2\,{L_1}^2\,d^2 + 10\,\pi^2\,L_1\,L_{dab}\,d^2 + 81\,L_1\,M\,d\,\phi^2 + 27\,\pi\,L_1\,M\,d\,\phi - 15\,\pi^2\,L_1\,M\,d \\ +5\,\pi^2\,{L_{dab}}^2\,d^2 + 81\,L_{dab}\,M\,d\,\phi^2 + 27\,\pi\,L_{dab}\,M\,d\,\phi - 15\,\pi^2\,L_{dab}\,M\,d + 15\,\pi^2\,M^2 \end{array}}}{108\,f_s\,\pi\,\left|-M^2+L_1\,L_2+L_2\,L_{dab}\right|} & \text{if } -30^\circ \le \phi < 0^\circ \\ \frac{\sqrt{6}\,V_i \sqrt{\begin{array}{l} 5\,\pi^3\,{L_1}^2\,d^2 + 10\,\pi^3\,L_1\,L_{dab}\,d^2 - 81\,L_1\,M\,d\,\phi^3 + 81\,\pi\,L_1\,M\,d\,\phi^2 \\ +27\,\pi^2\,L_1\,M\,d\,\phi - 15\,\pi^3\,L_1\,M\,d + 5\,\pi^3\,{L_{dab}}^2\,d^2 - 81\,L_{dab}\,M\,d\,\phi^3 \\ +81\,\pi\,L_{dab}\,M\,d\,\phi^2 + 27\,\pi^2\,L_{dab}\,M\,d\,\phi - 15\,\pi^3\,L_{dab}\,M\,d + 15\,\pi^3\,M^2 \end{array}}}{108\,f_s\,\pi^{3/2}\,\left|-M^2+L_1\,L_2+L_2\,L_{dab}\right|} & \text{if } 0^\circ \le \phi \le 60^\circ \end{cases} . \tag{A.38}$$

$$i_{sw-a} = \begin{cases} -\frac{V_i\,(2\,L_2-M\,d)}{6\,f_s\,(-M^2+L_1\,L_2+L_2\,L_{dab})} & \text{if } -30^\circ \le \phi < 0^\circ \\ -\frac{2\pi\,L_2\,V_i-M\,V_i\,(\pi\,d-3\,d\,\phi)}{6 f_s\,\pi\,(-M^2+L_1\,L_2+L_2\,L_{dab})} & \text{if } 0^\circ \le \phi \le 60^\circ \end{cases} . \tag{A.39}$$

$$i_{sw-A} = \begin{cases} \frac{V_i\,(2\,L_1\,d-3\,M+2\,L_{dab}\,d)}{18\,f_s\,(L_2\,(L_1+L_{dab})-M^2)} & \text{if } -30^\circ \le \phi < 0^\circ \\ \frac{V_i\,(2\,\pi\,L_1\,d+2\,\pi\,L_{dab}\,d)+M\,V_i\,(9\,\phi-3\,\pi)}{18 f_s\,\pi\,(-M^2+L_1\,L_2+L_2\,L_{dab})} & \text{if } 0^\circ \le \phi \le 60^\circ \end{cases} . \tag{A.40}$$

A.6 IDD 3ϕ NETWORK

$$I_o = \begin{cases} -\frac{M\,V_i\,\phi\,(3\,\phi-4\,\pi)}{4\,f_s\,\pi^2\,(L_2\,(L_1+L_{dab})-M^2)} & \text{if } 0^\circ \le \phi < 30^\circ \\ -\frac{M\,V_i\left(18\,\phi^2-18\,\pi\,\phi+\pi^2\right)}{12\,f_s\,\pi^2\,(L_2\,(L_1+L_{dab})-M^2)} & \text{if } 30^\circ \le \phi \le 90^\circ \end{cases} . \tag{A.41}$$

$$i_{ld-a-rms} = \begin{cases} \frac{V_i \sqrt{5\,\pi^3\,{L_2}^2 - 27\,L_2\,M\,d\,\phi^3 + 54\,\pi\,L_2\,M\,d\,\phi^2 - 10\,\pi^3\,L_2\,M\,d + 5\,\pi^3\,M^2\,d^2}}{18\,f_s\,\pi^{3/2}\,|-M^2 + L_1\,L_2 + L_2\,L_{dab}|} & \text{if } 0° \leq \phi < 30° \\ \frac{V_i \sqrt{5\,\pi^3\,{L_2}^2 - 54\,L_2\,M\,d\,\phi^3 + 81\,\pi\,L_2\,M\,d\,\phi^2 - 9\,\pi^2\,L_2\,M\,d\,\phi - 9\,\pi^3\,L_2\,M\,d + 5\,\pi^3\,M^2\,d^2}}{18\,f_s\,\pi^{3/2}\,|-M^2 + L_1\,L_2 + L_2\,L_{dab}|} & \text{if } 30° \leq \phi \leq 90° \end{cases} . \tag{A.42}$$

$$i_{tr-a-rms} = \begin{cases} \frac{V_i \sqrt{5\,\pi^3\,{L_2}^2 - 27\,L_2\,M\,d\,\phi^3 + 54\,\pi\,L_2\,M\,d\,\phi^2 - 10\,\pi^3\,L_2\,M\,d + 5\,\pi^3\,M^2\,d^2}}{18\,f_s\,\pi^{3/2}\,|-M^2 + L_1\,L_2 + L_2\,L_{dab}|} & \text{if } 0° \leq \phi < 30° \\ \frac{V_i \sqrt{5\,\pi^3\,{L_2}^2 - 54\,L_2\,M\,d\,\phi^3 + 81\,\pi\,L_2\,M\,d\,\phi^2 - 9\,\pi^2\,L_2\,M\,d\,\phi - 9\,\pi^3\,L_2\,M\,d + 5\,\pi^3\,M^2\,d^2}}{18\,f_s\,\pi^{3/2}\,|-M^2 + L_1\,L_2 + L_2\,L_{dab}|} & \text{if } 30° \leq \phi \leq 90° \end{cases} . \tag{A.43}$$

$$i_{tr-A-rms} = \begin{cases} \frac{V_i \sqrt{\begin{array}{l} 5\,\pi^3\,{L_1}^2\,d^2 + 10\,\pi^3\,L_1\,L_{dab}\,d^2 - 27\,L_1\,M\,d\,\phi^3 + 54\,\pi\,L_1\,M\,d\,\phi^2 - 10\,\pi^3\,L_1\,M\,d \\ +5\,\pi^3\,{L_{dab}}^2\,d^2 - 27\,L_{dab}\,M\,d\,\phi^3 + 54\,\pi\,L_{dab}\,M\,d\,\phi^2 - 10\,\pi^3\,L_{dab}\,M\,d + 5\,\pi^3\,M^2 \end{array}}}{18\,f_s\,\pi^{3/2}\,|-M^2 + L_1\,L_2 + L_2\,L_{dab}|} & \text{if } 0° \leq \phi < 30° \\ \frac{V_i \sqrt{\begin{array}{l} 5\,\pi^3\,{L_1}^2\,d^2 + 10\,\pi^3\,L_1\,L_{dab}\,d^2 - 54\,L_1\,M\,d\,\phi^3 + 81\,\pi\,L_1\,M\,d\,\phi^2 \\ -9\,\pi^2\,L_1\,M\,d\,\phi - 9\,\pi^3\,L_1\,M\,d + 5\,\pi^3\,{L_{dab}}^2\,d^2 - 54\,L_{dab}\,M\,d\,\phi^3 \\ +81\,\pi\,L_{dab}\,M\,d\,\phi^2 - 9\,\pi^2\,L_{dab}\,M\,d\,\phi - 9\,\pi^3\,L_{dab}\,M\,d + 5\,\pi^3\,M^2 \end{array}}}{18\,f_s\,\pi^{3/2}\,|-M^2 + L_1\,L_2 + L_2\,L_{dab}|} & \text{if } 30° \leq \phi \leq 90° \end{cases} . \tag{A.44}$$

$$i_{sw-a-rms} = \begin{cases} \frac{\sqrt{6}\,V_i \sqrt{5\,\pi^3\,{L_2}^2 - 27\,L_2\,M\,d\,\phi^3 + 54\,\pi\,L_2\,M\,d\,\phi^2 - 10\,\pi^3\,L_2\,M\,d + 5\,\pi^3\,M^2\,d^2}}{36\,f_s\,\pi^{3/2}\,|-M^2 + L_1\,L_2 + L_2\,L_{dab}|} & \text{if } 0° \leq \phi < 30° \\ \frac{\sqrt{6}\,V_i \sqrt{5\,\pi^3\,{L_2}^2 - 54\,L_2\,M\,d\,\phi^3 + 81\,\pi\,L_2\,M\,d\,\phi^2 - 9\,\pi^2\,L_2\,M\,d\,\phi - 9\,\pi^3\,L_2\,M\,d + 5\,\pi^3\,M^2\,d^2}}{36\,f_s\,\pi^{3/2}\,|-M^2 + L_1\,L_2 + L_2\,L_{dab}|} & \text{if } 30° \leq \phi \leq 90° \end{cases} . \tag{A.45}$$

$$i_{sw-A-rms} = \begin{cases} \frac{\sqrt{6}\,V_i \sqrt{\begin{array}{l} 5\,\pi^3\,{L_1}^2\,d^2 + 10\,\pi^3\,L_1\,L_{dab}\,d^2 - 27\,L_1\,M\,d\,\phi^3 + 54\,\pi\,L_1\,M\,d\,\phi^2 - 10\,\pi^3\,L_1\,M\,d \\ +5\,\pi^3\,{L_{dab}}^2\,d^2 - 27\,L_{dab}\,M\,d\,\phi^3 + 54\,\pi\,L_{dab}\,M\,d\,\phi^2 - 10\,\pi^3\,L_{dab}\,M\,d + 5\,\pi^3\,M^2 \end{array}}}{36\,f_s\,\pi^{3/2}\,|-M^2+L_1\,L_2+L_2\,L_{dab}|} & \text{if } 0° \le \phi < 30° \\ \frac{\sqrt{6}\,V_i \sqrt{\begin{array}{l} 5\,\pi^3\,{L_1}^2\,d^2 + 10\,\pi^3\,L_1\,L_{dab}\,d^2 - 54\,L_1\,M\,d\,\phi^3 + 81\,\pi\,L_1\,M\,d\,\phi^2 \\ -9\,\pi^2\,L_1\,M\,d\,\phi - 9\,\pi^3\,L_1\,M\,d + 5\,\pi^3\,{L_{dab}}^2\,d^2 - 54\,L_{dab}\,M\,d\,\phi^3 \\ +81\,\pi\,L_{dab}\,M\,d\,\phi^2 - 9\,\pi^2\,L_{dab}\,M\,d\,\phi - 9\,\pi^3\,L_{dab}\,M\,d + 5\,\pi^3\,M^2 \end{array}}}{36\,f_s\,\pi^{3/2}\,|-M^2+L_1\,L_2+L_2\,L_{dab}|} & \text{if } 30° \le \phi \le 90° \end{cases} . \tag{A.46}$$

$$i_{sw-a} = \begin{cases} -\frac{2\pi\,L_2\,V_i - M\,V_i\,(2\,\pi\,d - 3\,d\,\phi)}{6 f_s\,\pi\,(-M^2+L_1\,L_2+L_2\,L_{dab})} & \text{if } 0° \le \phi < 30° \\ -\frac{2\pi\,L_2\,V_i - M\,V_i\,(3\,\pi\,d - 6\,d\,\phi)}{6 f_s\,\pi\,(-M^2+L_1\,L_2+L_2\,L_{dab})} & \text{if } 30° \le \phi \le 90° \end{cases} . \tag{A.47}$$

$$i_{sw-A} = \begin{cases} \frac{V_i\,(2\,\pi\,L_1\,d + 2\,\pi\,L_{dab}\,d) + M\,V_i\,(3\,\phi - 2\,\pi)}{6 f_s\,\pi\,(-M^2+L_1\,L_2+L_2\,L_{dab})} & \text{if } 0° \le \phi < 30° \\ \frac{V_i\,(2\,\pi\,L_1\,d + 2\,\pi\,L_{dab}\,d) + M\,V_i\,(6\,\phi - 3\,\pi)}{6 f_s\,\pi\,(-M^2+L_1\,L_2+L_2\,L_{dab})} & \text{if } 30° \le \phi \le 90° \end{cases} . \tag{A.48}$$

APPENDIX

B DAB3 converter prototype

This appendix outlines the design characteristics and parameters of the DAB3 converter prototype, which was constructed to obtain the experimental results presented in Chapter 3.

B.1 INVERTER DESIGN

The DAB3 consists of two three-phase inverters. Two identical inverters are built to facilitate the prototype modularity, as shown in Figure B.1.

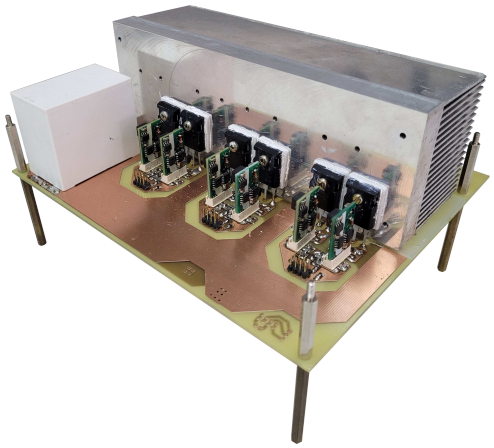

Figure B.1 – Three-phase inverter.

The C2M0080120D power switch, a Silicon Carbide MOSFET rated at 1200 V/36 A, has been selected for the DAB3. The theoretical temperature rise is analyzed by considering a heatsink with a thermal resistance of approximately 0.65 °C/W, an insulator resistance of 0.45 °C/W and a junction-to-case thermal resistance of 0.6 °C/W. The resulting temperature elevation profiles for both primary and secondary power switches, as well as for both 3ϕ network, are shown in Figure B.2. The highest temperature elevation is found in the secondary power switches with the YY transformer at 400 V and 10 A, which results in a temperature rise of 75.8 °C. Assuming an ambient temperature of 30 °C, this leads to a maximum temperature of 105.8 °C.

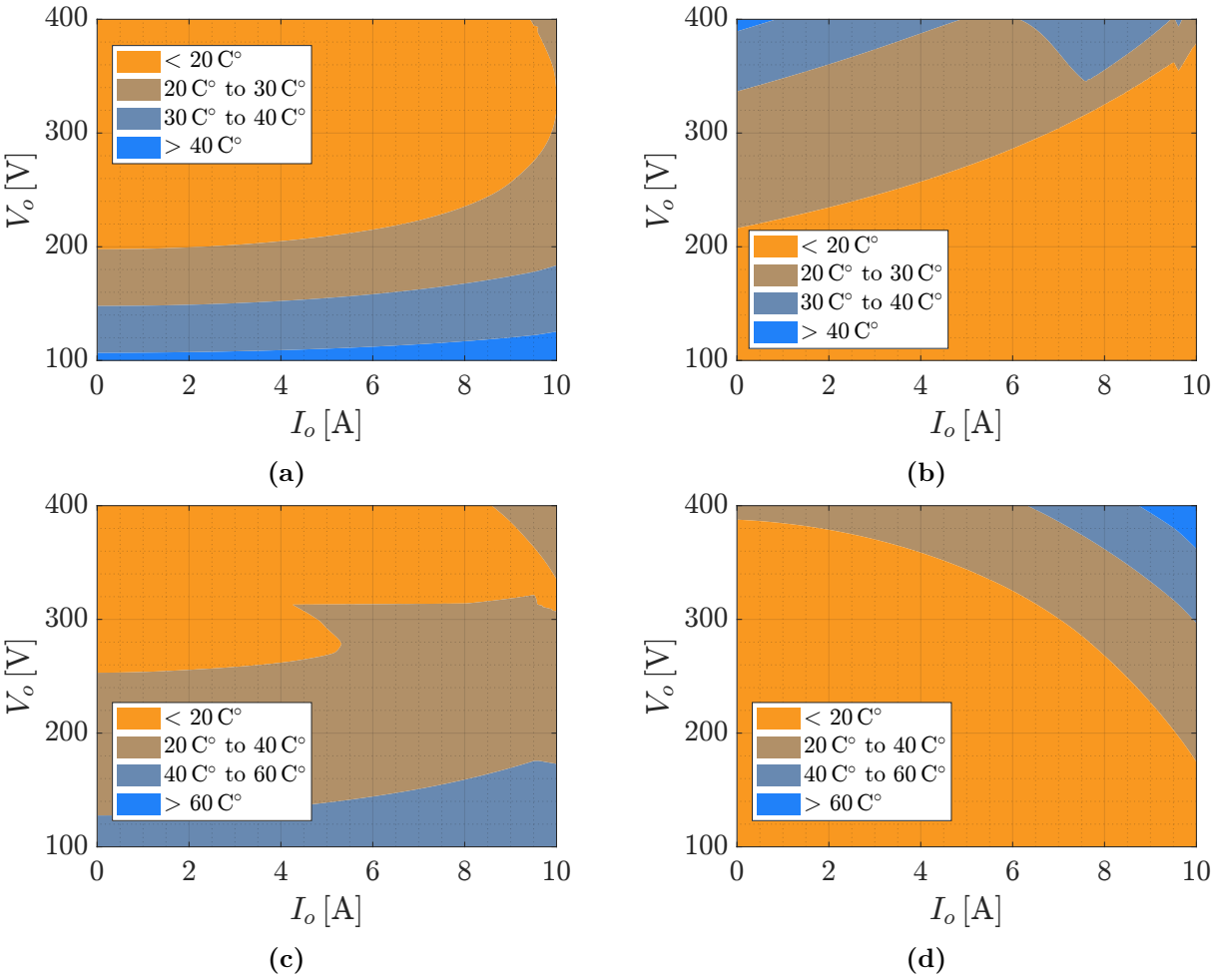

Figure B.2 – Theoretical Temperature Elevation of Primary and Secondary Power Switches: (a) iDY Primary, (b) YY Primary, (c) iDY Secondary, (d) YY Secondary

For both the input and output DC bus, the MHBS455400 800 V capacitor of 40 μF is used. Figure B.3 (a) and (b) show the voltage ripple at the input for the 3ϕ network iDY and YY, respectively. On the other hand, Figure B.3 (c) and (d) display the voltage ripple at the output of the converter for the 3ϕ network iDY and YY, respectively. With this capacitance, the maximum voltage output ripple is 78 mV with a 100 V with the iDY 3ϕ network, which corresponds to a percentage ripple of 0.08%.

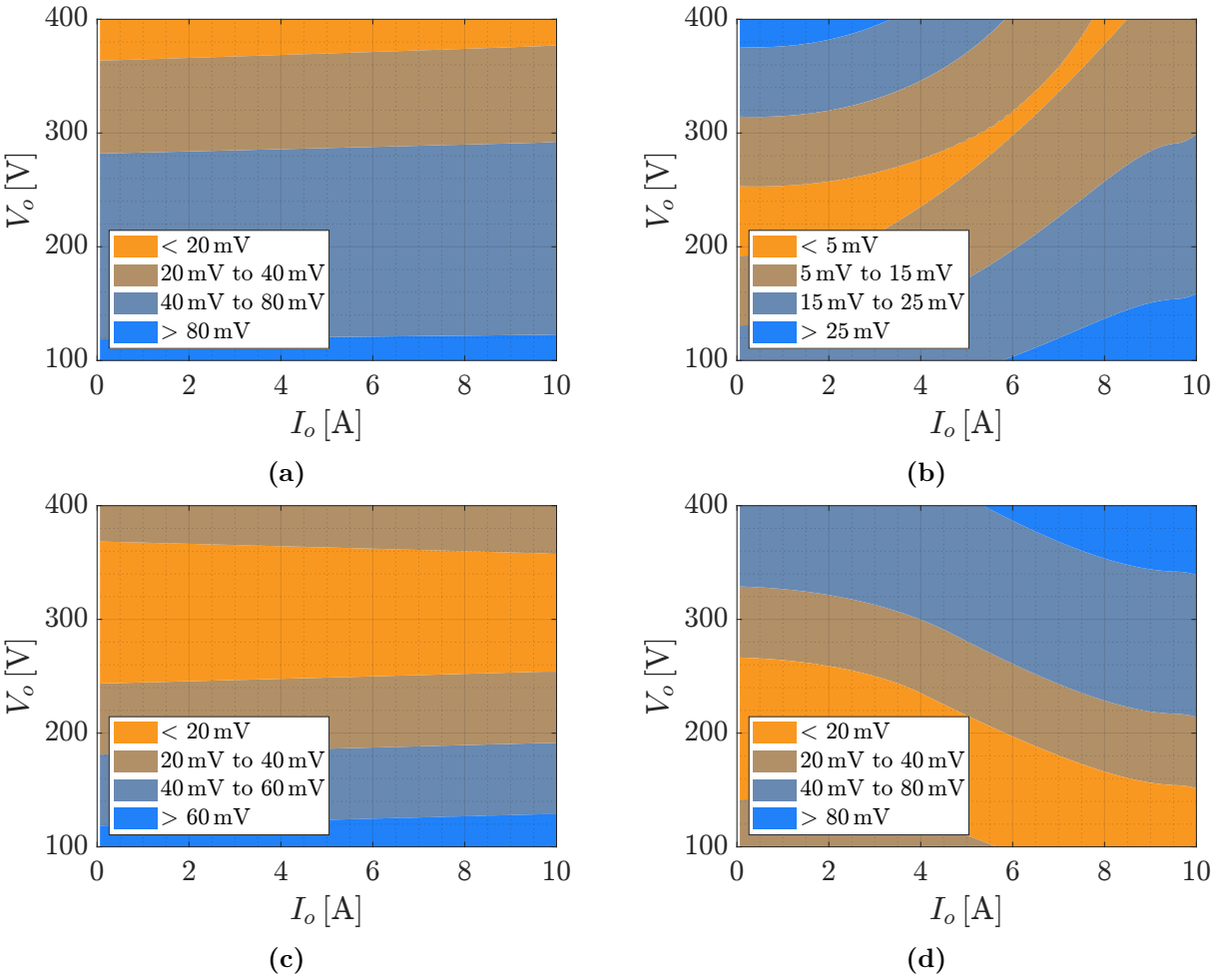

Figure B.3 – Theoretical voltage ripple: (a) iDY Primary (ΔV_i), (b) YY Primary (ΔV_i), (c) iDY Secondary (ΔV_o), (d) YY Secondary (ΔV_o)

B.2 DESIGN OF MAGNETIC COMPONENTS

In this section, the design of both the inductor and the transformer are presented.

B.2.1 Inductor Design

The design method utilized in this work is based on the approach described in [32], and incorporates the air gap estimation method proposed by [40]. For a desired inductance of 61.6 μH, this methodology led to the construction of an inductor consisting of two N87 E55/28/25 with 14 turns using 2 litz wires, 180x38AWG, in parallel, and an air gap of 1.15 mm. The inductor built is presented in Figure B.4.

Figure B.5 shows the inductor impedance measured with the Agilent 4294A impedance analyser. Figure B.5 (a) presents the inductance values for the three inductors. Significant variations in these inductance values could lead to an asymmetrical current distribution among the phases, potentially causing some phases to lose ZVS while others maintain it.

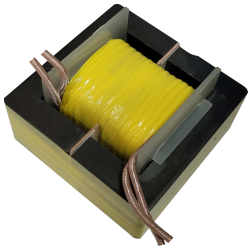

Figure B.4 – Built inductor.

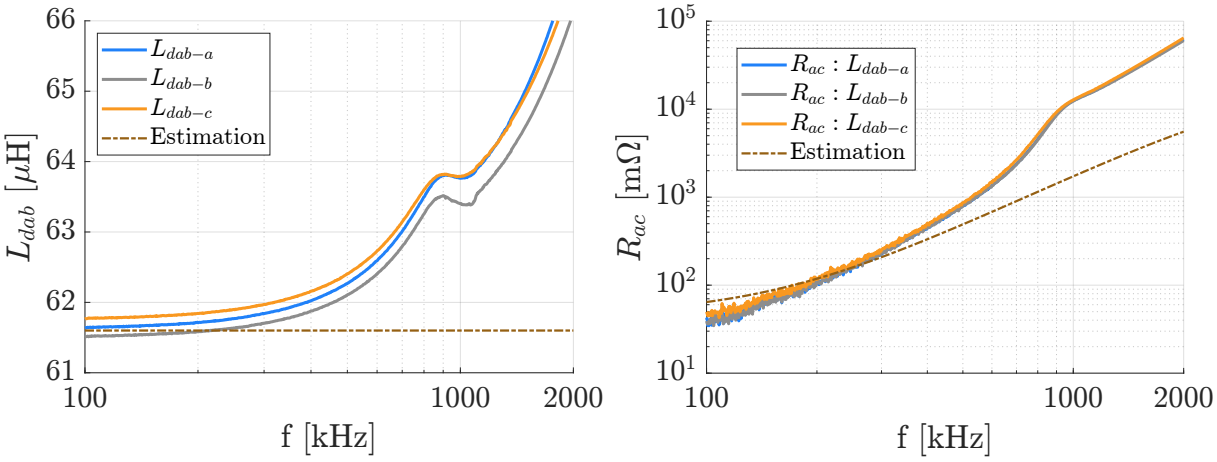

Figure B.5 – (a) Measured inductance (b) Measured resistance

Figure B.5 (b) shows the inductor coil AC resistance. The simplifications made in the analysis that can explain the error in the AC resistance are:

- Neglecting the gap effect on coil resistance;
- The proximity effects caused by parallel litz wires (two wires used in parallel) are not taken into account;
- The impedance analyzer calculates the resistance considering not only the coil resistance but also the losses in the core material;
- The Dowell equation formulations are based on transformers [41], and might not be really accurate for inductors.

Despite its simplifications, this model is considered sufficiently accurate and is used to estimate losses and temperature elevation in the inductor. Figure B.6 presents the temperature rising along the variation of output voltage and output current. The maximum temperature variation expected for the inductor with the transformers iDY and YY are respectively 42 °C and 59 °C. Assuming a temperature ambient of 30 °C, leads to a temperature of 72 °C and 89 °C, respectively.

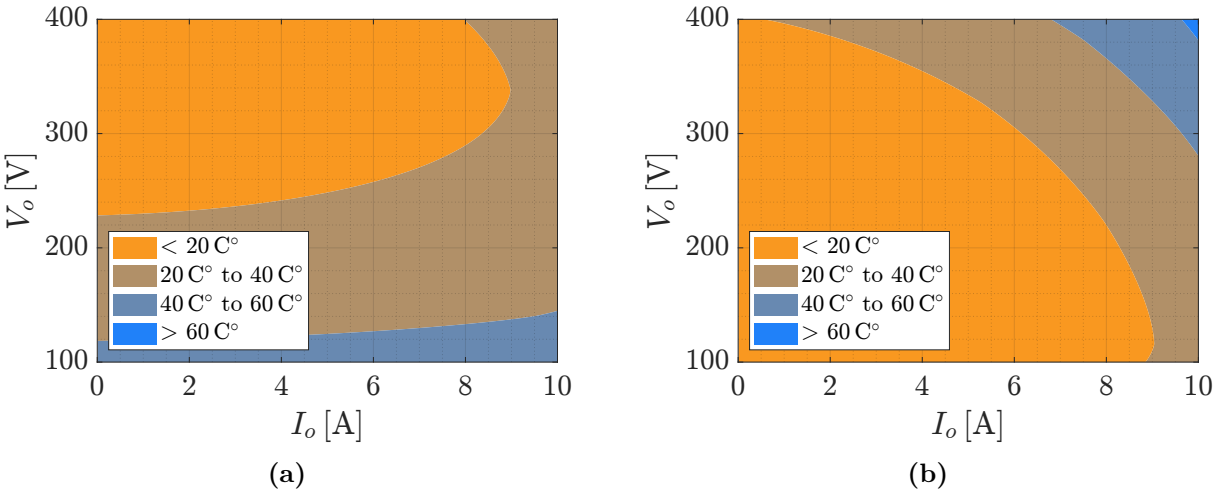

Figure B.6 – Theoretical inductor temperature elevation (a) iDY (b) YY

B.2.2 Three-phase transformer design

The three-phase transformer features a five-legged core, as shown in Figure B.7 (a) and (b). This design allows for magnetic flux paths around the three core legs between the top and bottom yokes, while the fourth and fifth core legs serve as return paths for residual flux from the top to the bottom yoke. To reduce the transformer overall height, the top and bottom core yokes have a reduced cross-sectional area since they don't need to carry the full flux from each phase. However, this reduction in yoke cross-sectional area can lead to some of the normal flux from the outer phases flowing through the fourth and fifth core legs, making the actual flux path uncertain and complicating the calculation of core losses [42].

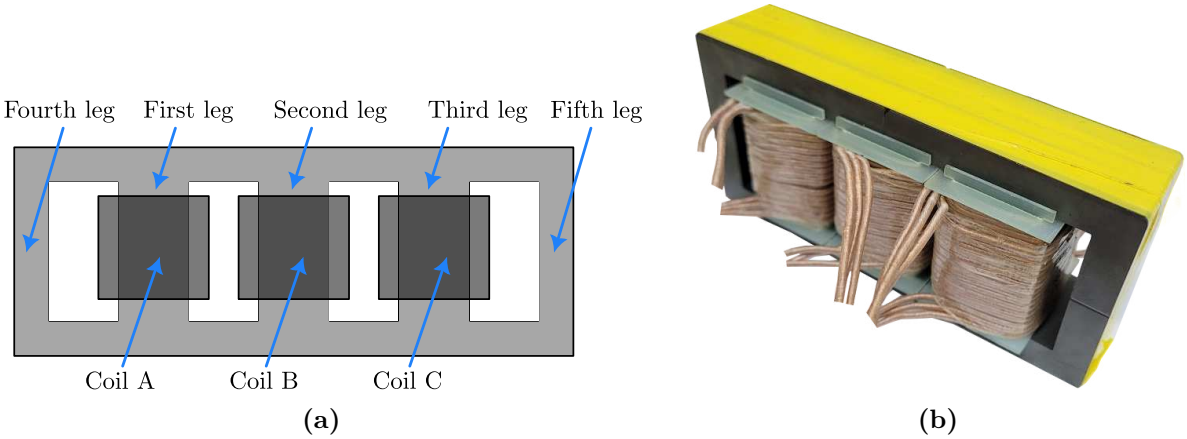

Figure B.7 – (a) Five-limb three-phase transformer (b) Built five-limb three-phase transformer.

The flux density behavior of a five-leg three-phase transformer is depicted in Figure B.8, which includes simulations conducted using the FEMM 4.2 software. The gray areas represent regions with high flux densities, while the white areas represent regions with low flux densities.

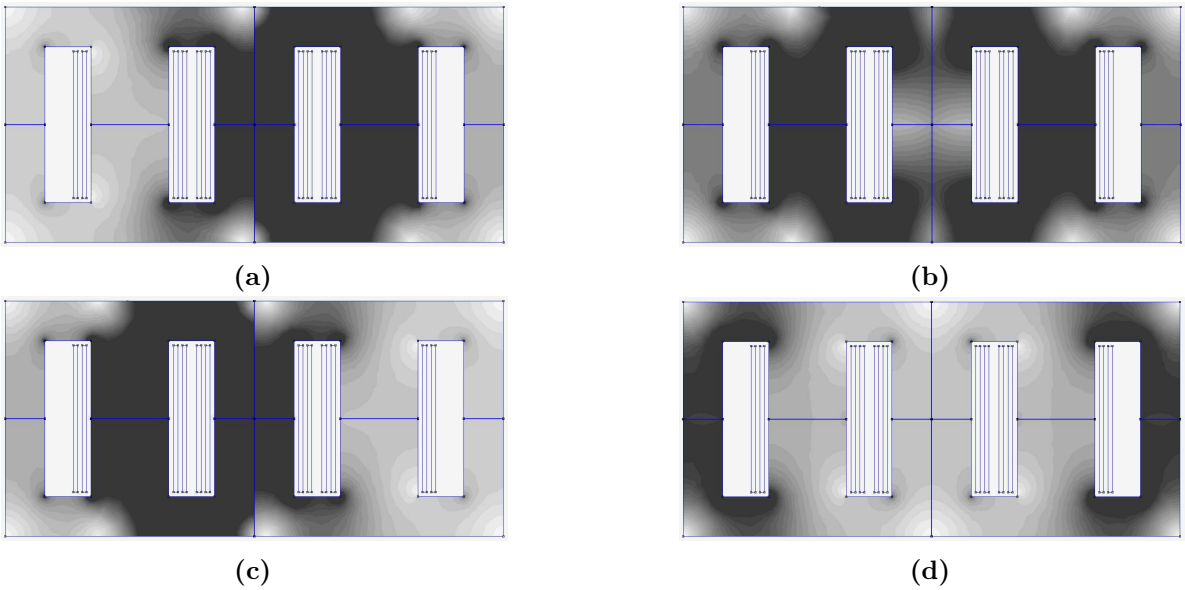

Figure B.8 – Flux density simulation in FEMM 4.2 for a 3-phase 5-leg transformer with the following abc currents (a) $i_a = 0\,\text{A}$, $i_b = -7\,\text{A}$ and $i_c = -7\,\text{A}$ (b) $i_a = 7\,\text{A}$, $i_b = 0\,\text{A}$ and $i_c = -7\,\text{A}$ (c) $i_a = -7\,\text{A}$, $i_b = 7\,\text{A}$ and $i_c = 0\,\text{A}$ (d) $i_a = 5.7\,\text{A}$, $i_b = 5.7\,\text{A}$ and $i_c = 5.7\,\text{A}$

Figures B.8 (a-c) show simulations with balanced phase currents, while Figure B.8 (d) illustrates a situation with an average current value across all phases, indicating unbalanced currents. The fourth and fifth legs of the transformer exhibit high flux density only in the presence of unbalanced currents, as seen in Figure B.8 (d). Therefore, when estimating losses, the effective core volume excludes the fourth and fifth legs, which are not subject to significant flux density in balanced current scenarios.

The design method described in [32] is employed which yields four 3C94 E71/33/32 with a transformation ratio of 5/9. The secondary winding consists of 5 turns with 3 litz wires 180x38AWG in parallel, while the primary winding is composed of 9 turns with 2 litz wires 180x38AWG in parallel.

The transformer impedance is measured using an impedance analyzer to confirm whether the values fall within the expected range. The transformer testing only considers the coupling between coils of the same phase.

The magnetizing inductance estimation, assuming a transformer without a gap, is calculated as

$$L_m = \frac{N_p^2}{l_c} \mu_0 \mu_r A_c. \tag{B.1}$$

The primary-side measured magnetizing inductance values are depicted in Figure B.9.

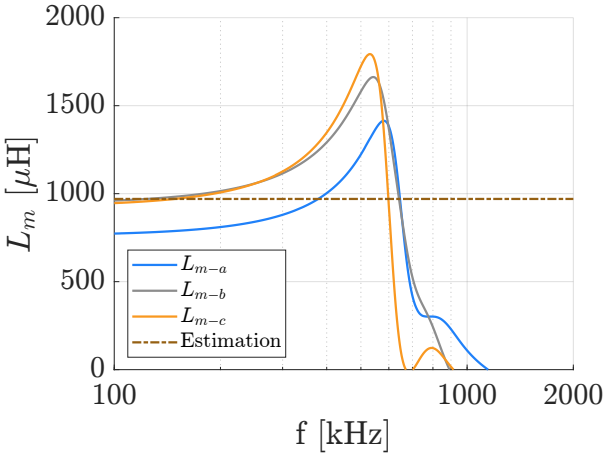

Figure B.9 – Measured magnetizing inductance referred to the primary side.

The total leakage inductance of a transformer is closely related to the volume of space occupied by its windings. When the windings are spread out further across the core, denoted by an increased value of w (window width), leakage effects are reduced. Equation

$$L_{tr1} + \frac{L_{tr2}}{n^2} = \frac{\mu_0 N_p^2 MLTb}{3w} \tag{B.2}$$

demonstrates that having fewer turns in a winding can reduce its leakage inductance [32].

The leakage inductance is measured using an impedance analyzer. The test is conducted by measuring one side of the transformer while short-circuiting the other side. Figure B.10 shows the measured leakage inductance for both sides of the transformer.

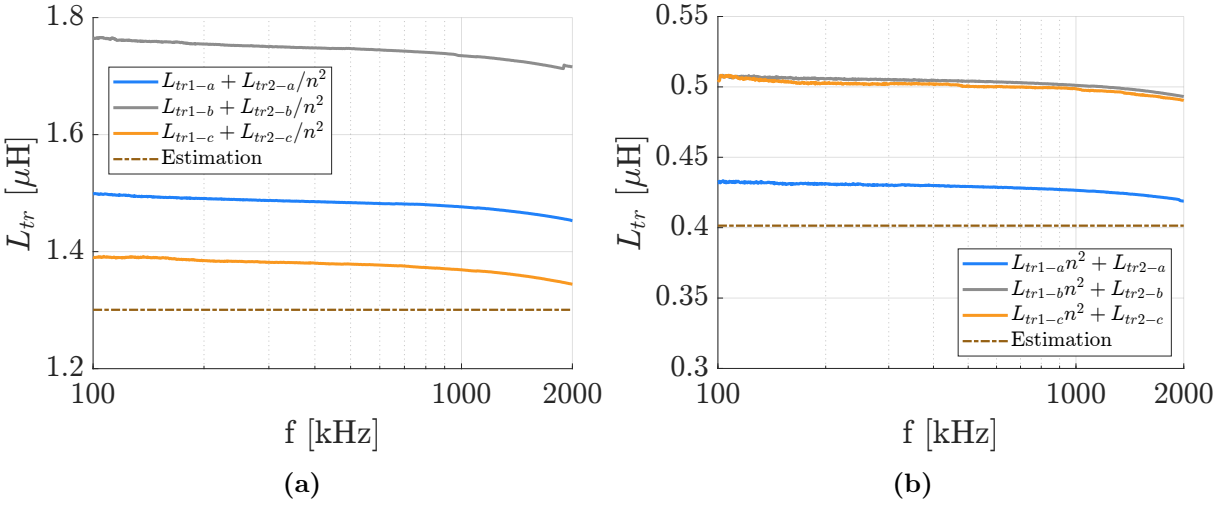

Figure B.10 – (a) Measured leakage inductance referred to the secondary side, (b) Measured leakage inductance referred to the secondary side.

This test, conducted to measure the leakage inductance, is also utilized for verifying the coil resistance. Figure B.11 presents the resistance measured alongside the theoretically calculated resistance. A comparison between Figure B.11 and Figure B.5 reveals that Dowell equations are more suitable for transformers than inductors.

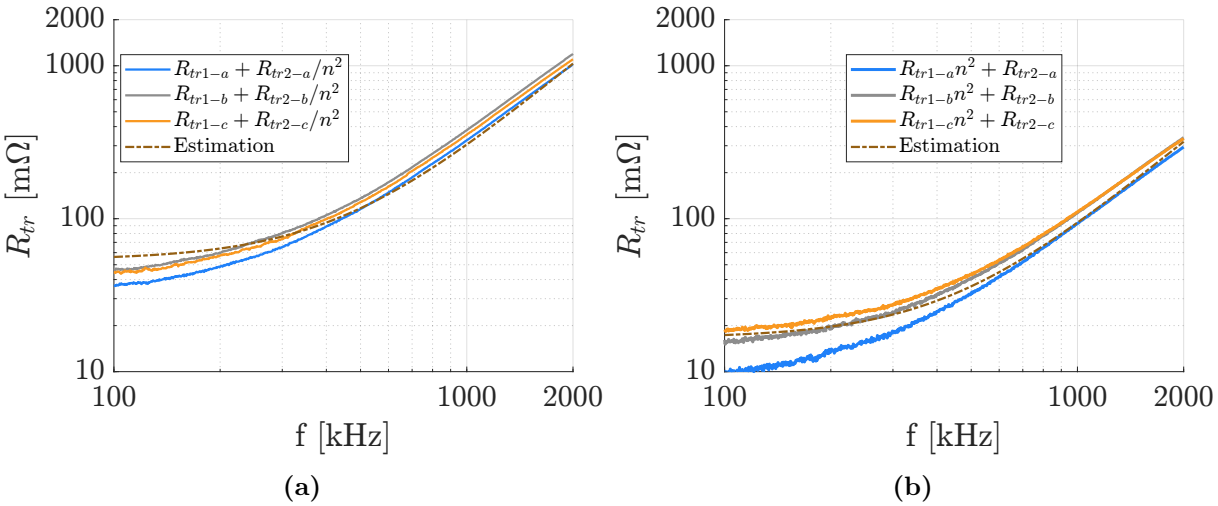

Figure B.11 – (a) Measured winding resistance referred to the primary side (b) Measured winding resistance referred to the secondary side

Figure B.12 presents the temperature rise along the variation of output voltage and output current. The maximum temperature variation expected for the transformer iDY and YY connection are respectively 54 °C and 67 °C. Assuming a temperature ambient of 30 °C lead to a temperature of 84 °C and 97 °C.

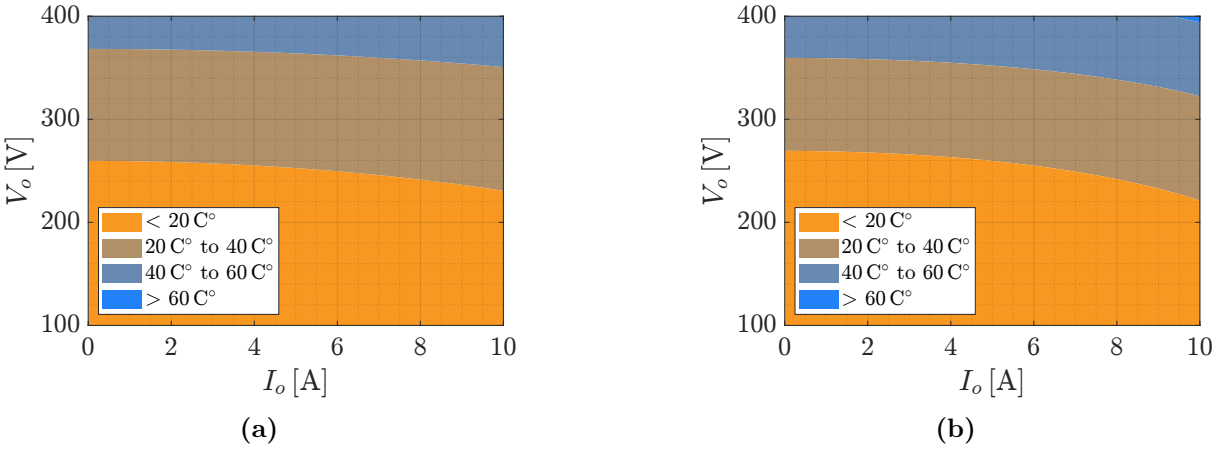

Figure B.12 – (a) Theoretical transformer temperature elevation with transformer iDY (b) Theoretical transformer temperature elevation with transformer YY

Figure B.13 presents the temperature in the magnetic elements in the nominal with a YY transformer.

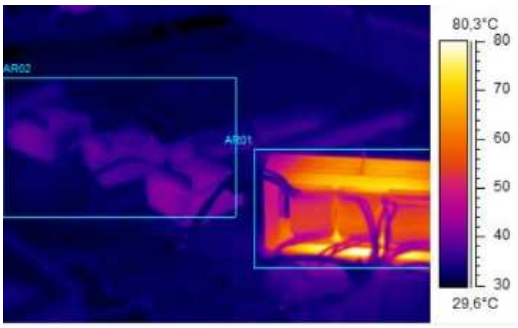

(a)

Figure B.13 – Nominal temperature using transformer YY, transformer maximum temperature: 80.6 °C, inductor maximum temperature: 42.7 °C

APPENDIX

C Loss and Thermal Models

In this section the main sources of converter losses are described.

C.1 POWER SWITCHES

The calculation of losses in a power switch considers two sources: conduction losses and switching losses.

C.1.1 Conduction losses

The mosfet C2M0080120D from Wolfspeed is used. The drain-source resistance ($R_{DS_{on}}$) depends on the gate voltage and temperature. Figure C.1 shows this relation for the C2M0080120D.

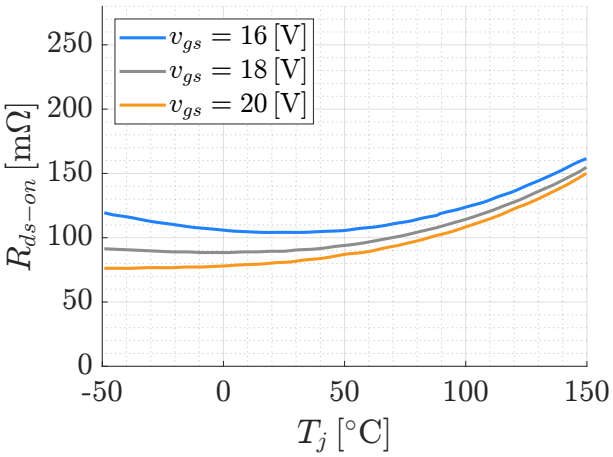

Figure C.1 – The drain-source resistance as function of junction temperature and gate voltage [35]

The gate driver used in this work was developed in [43], which provides a gate voltage of 17.5 V. Assuming that the temperature of the power switches is 75 °C, a linear interpolation from the graph results in

$$R_{S1} = R_{S2} = R_{ds-on,\text{C2M0080120D}} = 112\,m\Omega. \tag{C.1}$$

The primary conduction and secondary conduction losses are given by

$$P_{sw-a,cond} = 6R_{S1}I^2_{sw-a-rms} \qquad P_{sw-A,cond} = 6R_{S2}I^2_{sw-A-rms}. \tag{C.2}$$

C.1.2 Switching losses

The power switch datasheet provides switching energy graphs only for voltage levels of 600 V and 800 V. However, since the prototype operates at voltage levels ranging from 200 V to 400 V, interpolating the switching energy curves from the datasheet may not accurately represent the behavior at such distant voltage levels. To overcome this limitation, a simulation-based test of the power switch is conducted to obtain switching energy curves for voltage values closer to the operating range.

The inductive clamping test is performed using LTspice 17.0.35.0 software. The simulated circuit, as shown in Figure C.2, incorporates the manufacturer spice model for the power switch. By integrating the instantaneous power over the power switch Q_2, the turn-on and turn-off energies can be determined. This simulation enables the analysis of the power switch dynamics and the calculation of switching energy in the system.

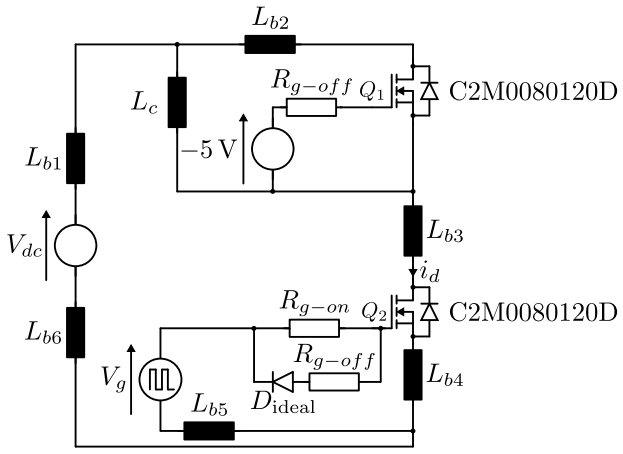

Figure C.2 – Clamped inductive switching waveform test circuit

To verify whether the calculated losses using the spice model align with expected values, the data obtained from the simulations are compared with the values provided in the datasheet. As the manufacturer does not provide information about the inductance of the PCB (L_b) used in the tests, it is assumed that the parasitic inductances of the PCB presented in [44] are similar to those used in the datasheet. Therefore, the following parasitic inductances are considered in the simulator:

$$L_{b1} = 12\,\mathrm{nH} \qquad L_{b2} = 16\,\mathrm{nH} \qquad L_{b3} = 47\,\mathrm{nH}$$
$$L_{b4} = 13\,\mathrm{nH} \qquad L_{b5} = 6\,\mathrm{nH} \qquad L_{b6} = 7\,\mathrm{nF}.$$

Figure C.3 illustrates the switching energy for both turn-on and turn-off. It compares the energy values obtained from the datasheet with the simulation results, considering scenarios without any PCB inductance and with the PCB inductance included.

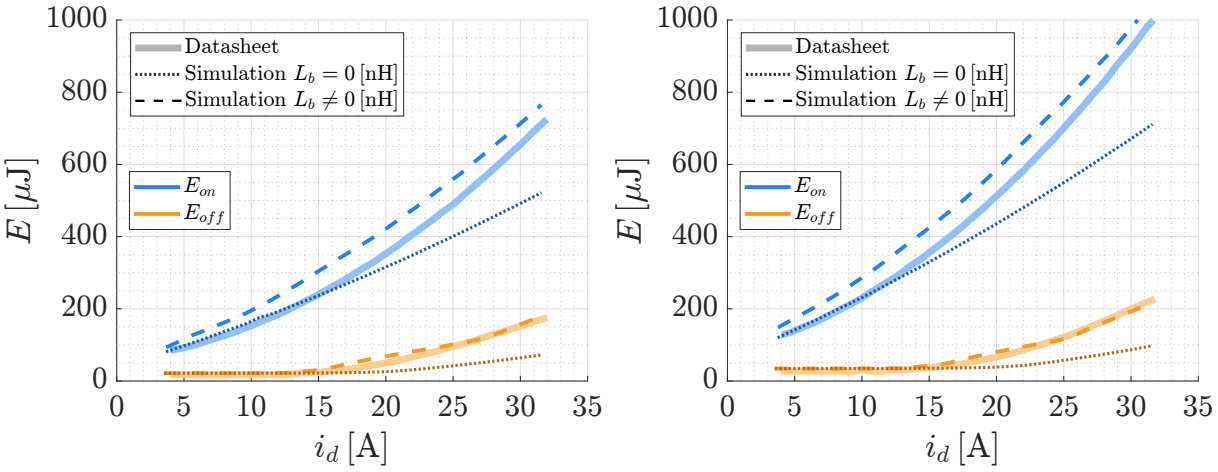

Figure C.3 – Clamped inductive switching energy vs drain current, spice model simulation data versus the datasheet data ($R_{g-on} = R_{g-off} = 2.5\,\Omega$) (a) $V_{dc} = 600\,\text{V}$ (b) $V_{dc} = 800\,\text{V}$

Figure C.3 reveals that the switching energy is lower than the value provided by the datasheet when no parasitic inductances of the PCB are considered. However, the losses exceed the value given in the datasheet when including the parasitic inductances. As a result, it is concluded that the simulated circuit can adequately represent the switching losses depending on how close the parasitic inductances are to the real values. For the prototype constructed in this work, it is assumed that the parasitic inductances are close to the values presented in this section. Based on this, simulations are conducted with voltage levels experienced by the DAB3 prototype. The data is presented in Figure C.4.

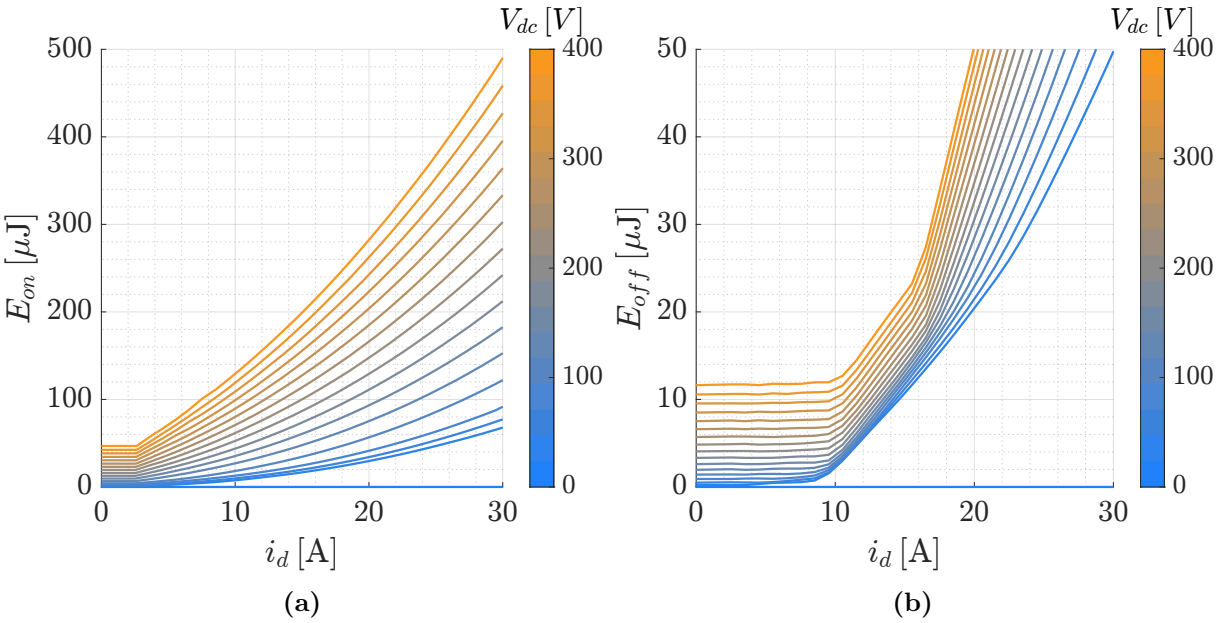

Figure C.4 – Simulation data of switching energy vs drain current for different bus voltages ($R_{g-on} = 10\,\Omega$ and $R_{g-off} = 2.5\,\Omega$) (a) Turn on energy (b) Turn off energy

The 3D surface plot of the switching energy is presented in Figure C.5.

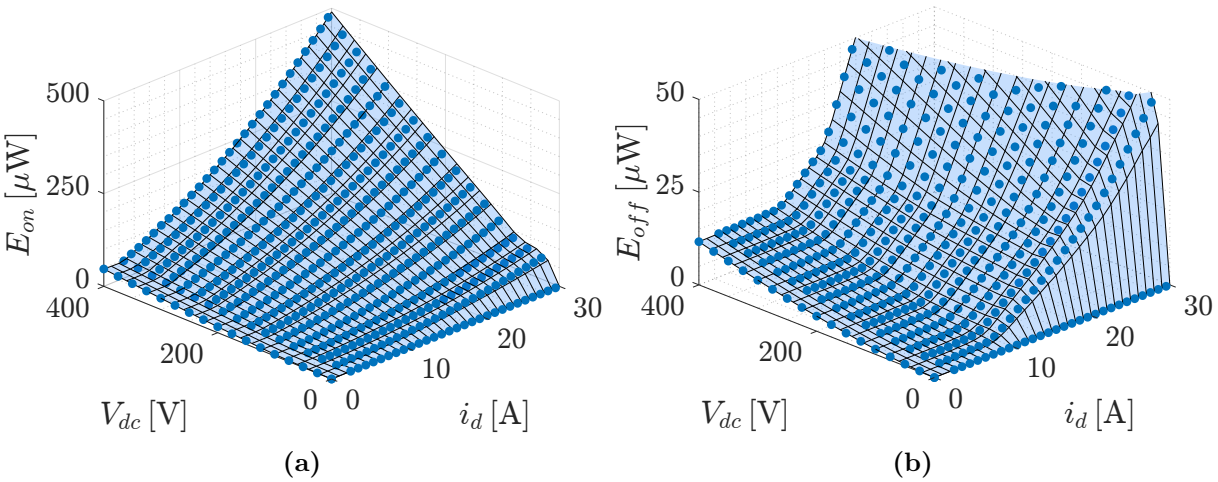

Figure C.5 – Switching energy surfaces made from the linear interpolation from simulation data (a) Turn on energy (b) Turn off energy

Once the turn on energy and turn off energy are obtained, the turn on loss and turn off loss are given by

$$P_{on} = E_{on} f_s \qquad\qquad P_{off} = E_{off} f_s. \tag{C.3}$$

The switching loss is given by

$$P_{sw} = P_{on} + P_{off}. \tag{C.4}$$

C.1.3 Semiconductors thermal model

It is possible to estimate the temperature rise of the semiconductors based on the losses. The considered model is presented in Figure C.6.

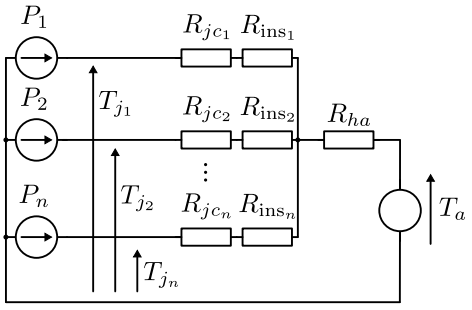

Figure C.6 – Semiconductor simplified thermal model

The temperature estimation equation, considering that all power switches are identical and have the same loss when connected to a heatsink, can be expressed as

$$T_j = P_{\text{tot}} \left(\frac{R_{jc} + R_{\text{ins}}}{n} + R_{ha} \right) + T_a. \tag{C.5}$$

Where P_{tot} represents the total loss in all power switches, R_{jc} is the internal thermal resistance of the power switch, R_{ins} is the thermal resistance between the heatsink and the junction of the power switch, n is the number of power switches, R_{ha} is the heatsink thermal resistance, and T_a is the ambient temperature.

C.2 TRANSFORMER, INDUCTOR

The calculation of losses in magnetic components can be separated into two sources, copper losses and core losses.

C.2.1 Copper

Losses in inductor or transformer conductors are caused by two effects: the skin effect and the proximity effect. The litz-wire is designed with the aim of reducing these losses. Because if a multistrand conductor is used, the total cross-sectional area is distributed among many conductors with small diameters. For this reason, the litz-wire may result in a more uniform current density distribution than a solid wire [14, 45].

Dowell expression for the winding resistance of the adapted foil inductor was used to describe the resistance of the litz wire winding [45]. The ratio of DC resistance R_{wDC} to AC resistance $R_{w,f}$ is called ratio F_R and can be calculated as

$$F_R = \frac{R_{w,f}}{R_{wDC}} = A\left(F_P + F_S\right). \tag{C.6}$$

Where F_R depends on: skin effect factor F_S, given by

$$F_S = \frac{\sinh(2A) + \sin(2A)}{\cosh(2A) - \cos(2A)}, \tag{C.7}$$

proximity effect factor F_P, given by

$$F_P = \frac{2(N_l^2 k - 1)}{3} \frac{\sinh(A) - \sin(A)}{\cosh(A) + \cos(A)}, \tag{C.8}$$

and effective litz-wire diameter A, given by

$$A = \left(\frac{\pi}{4}\right)^{0.75} \frac{d_l}{\delta_w} \sqrt{\eta}. \tag{C.9}$$

The following variables are used in Equations C.6-C.9: d_l is the diameter of the conductor of the litz-wire strand; N_l number of winding layers; k number of strands [14].

The R_{wDC} is given by

$$R_{wDC} = \frac{4\rho_w N l_T}{k\pi d_l^2}. \tag{C.10}$$

The skin depth of winding conductor is given by

$$\delta_w = \sqrt{\frac{\rho_w}{\pi \mu_0 f}}. \tag{C.11}$$

The copper losses are given by

$$P_w = \sum_{j=1}^{\infty} R_{w,f} i_{rms}(f)^2. \tag{C.12}$$

Once the frequency dependent resistance is obtained, it is necessary to perform the following calculation

$$i_{rms}(f) = \frac{1}{\sqrt{2}\,T} \int_0^T i(t) e^{-j2\pi f t} dt \tag{C.13}$$

to obtain the rms current component at each frequency.

C.2.2 Core

The Steinmetz equation (SE), given by

$$P_V = k_c f^{\alpha} B_{pk}^{\beta}\,, \tag{C.14}$$

is used to estimate the losses in the core when subjected to a sinusoidal excitation. Where B_{pk} is the peak flux, f is the excitation frequency, P_V is the average power per unit volume, and k, α and β are the Steinmetz parameters, which can be calculated empirically [46].

As non-sinusoidal excitations are typical in power electronics, other methods are needed for more accurate calculations. Furthermore, the nonlinear behavior of ferromagnets means that simply adding individual components of the Fourier series does not work. The generic Steinmetz equation, given by

$$P_V = \frac{k_i}{T} \int_0^T \left| \frac{dB(t)}{dt} \right|^{\alpha} |\Delta B|^{\beta - \alpha}\, dt\,, \tag{C.15}$$

is an alternative to non-sinusoidal excitations, where ΔB is the peak-to-peak flux density and k_i is given by

$$k_i = \frac{k_c}{2^{\beta-1}\pi^{\alpha-1} \int_0^{2\pi} |\cos(\theta)|^{\alpha}\, d\theta}\,. \tag{C.16}$$

A limitation of iGSE is that it only works for $\alpha < \beta$, since not respecting this equality leads to an infinite loss. The materials used in this work satisfy this condition and therefore the iGSE method is used to calculate the losses [46, 32].

The magnetic flux density is given by

$$B(t) = \int_0^t \frac{v(t)}{N\,A_c} \mathrm{d}t, \tag{C.17}$$

where $v(t)$ is the voltage applied to the element, N is the number of turns, and A_c is the core cross-sectional area. The peak-to-peak flux density is calculated by

$$\Delta B = \max(B(t)) - \min(B(t)). \tag{C.18}$$

C.2.2.1 Steinmetz parameters

The Steinmetz parameters are needed to calculate the losses in the core; these are extracted from the loss curves of the material. The materials used in this work are N87 for the inductor and 3C94 for the transformer; their curves are presented in Figure C.7.

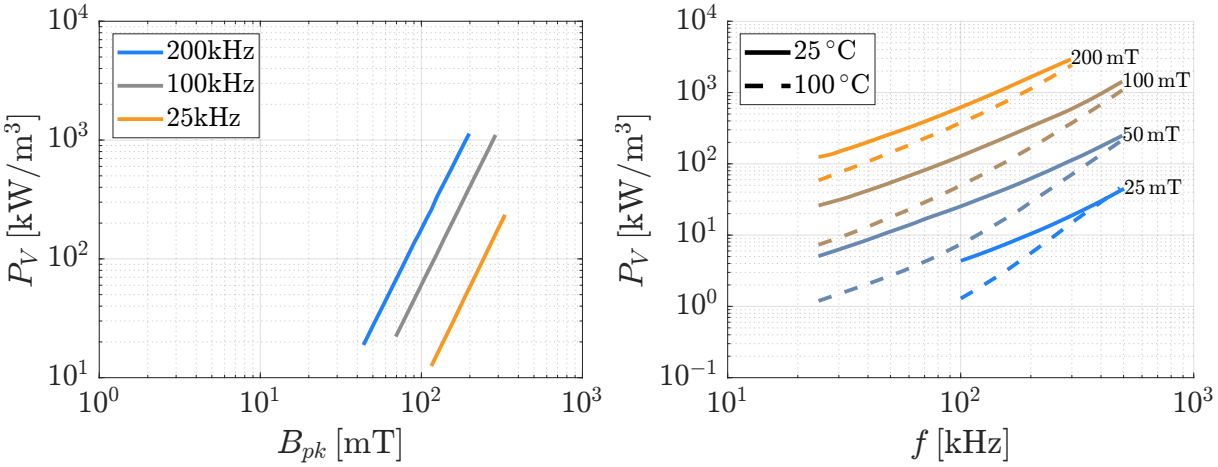

(a) **(b)**

Figure C.7 – P_V as a function of B_{pk} and f (a) Ferrite 3C94 at 100°C [47] (b) Ferrite N87 [48]

To obtain the parameters, the quadratic minimization is applied [49], several points are extracted and these are applied to the equation

$$\boldsymbol{\lambda} = (\mathbf{A}^T\mathbf{A})^{-1}\mathbf{A}^T\mathbf{b} = [\log(k_c)\alpha\beta]^T \tag{C.19}$$

where $\mathbf{A}$ and $\mathbf{b}$ are

$$\mathbf{A} = \begin{bmatrix} 1 & \log(f_1) & \log(B_{pk1}) \\ & \vdots & \\ 1 & \log(f_n) & \log(B_{pkn}) \end{bmatrix}, \quad \mathbf{b} = \begin{bmatrix} \log(P_{V1}) \\ \vdots \\ \log(P_{Vn}) \end{bmatrix}.$$

Therefore the coefficients obtained for ferrite N87 are

$$\alpha_{\text{N87}} = 1.29, \quad \beta_{\text{N87}} = 2.35, \quad k_{c_{\text{N87}}} = 11.19[\text{kW/m}^3], \tag{C.20}$$

and for 3C94 ferrite are

$$\alpha_{\text{3C94}} = 1.45, \quad \beta_{\text{3C94}} = 2.73, \quad k_{c_{\text{3C94}}} = 2.93[\text{kW/m}^3]\,. \tag{C.21}$$

C.2.3 Magnetic components thermal model

The surface power loss density of an inductor/transformer is given by

$$\psi = \frac{P_{total}\,[\mathrm{W}]}{A_t\,[\mathrm{cm}^2]}. \tag{C.22}$$

Where A_t is the radiating surface area, and P_{total} is the total loss (copper and core loss). The temperature rise for steady-state operation is given by [14]

$$\Delta T = 450\psi^{0.826}\,[^\circ\mathrm{C}]. \tag{C.23}$$

C.3 CAPACITOR

There are two different capacitors in the power system of the prototype: the series capacitor, which blocks the DC current level in the transformer, and the DC bus capacitor. The losses in both capacitors are calculated using

$$P_C = R_C I_{rms}^2. \tag{C.24}$$

Where P_C is the power dissipated by the capacitor, R_C is the equivalent series resistance of the capacitor, and I_{rms} is the rms current that flows through the capacitor.

The series capacitor, 75MW4560, is used for both the primary and secondary sides, which has

$$R_{C,p} = R_{C,s} = R_{C,\mathrm{75MW4560}} = 4.3\,\mathrm{m\Omega} \tag{C.25}$$

at 100 kHz.

The bus capacitor, MHBS455400, is also used for both the primary and secondary sides, and has

$$R_{C,bus} = R_{C,\mathrm{MHBS455400}} = 4.2\,\mathrm{m\Omega} \tag{C.26}$$

at 10 kHz. It is assumed that the resistance at 100 kHz is the same.